



Universiteit  
Leiden  
The Netherlands

**Evolution of Au(111) electrode surface in different electrolytes and conditions studied with a home-made EC-STM**  
Behjati, S.

**Citation**

Behjati, S. (2026, January 28). *Evolution of Au(111) electrode surface in different electrolytes and conditions studied with a home-made EC-STM*. Retrieved from <https://hdl.handle.net/1887/4290073>

Version: Publisher's Version

License: [Licence agreement concerning inclusion of doctoral thesis in the Institutional Repository of the University of Leiden](#)

Downloaded from: <https://hdl.handle.net/1887/4290073>

**Note:** To cite this publication please use the final published version (if applicable).

# **Evolution of Au(111) Electrode Surface in Different Electrolytes and Conditions Studied with a Home-made EC-STM**

Proefschrift

ter verkrijging van  
de graad van doctor aan de Universiteit Leiden,  
op gezag van de waarnemend rector magnificus,  
volgens besluit van het college voor promoties  
te verdedigen op woensdag 28 januari 2026  
klokke 14:30 uur

door Saeid Behjati

geboren te Tehran, Iran

in 1991

**Promotor:**

Prof. dr. M.T.M. Koper

**Co-promotor:**

Dr. R.V. Mom

**Promotiecommissie:**

Prof. dr. M. Ubbink

Prof. dr. J.M. van Ruitenbeek

Dr. D.G.H. Hetterscheid

Prof. dr. A. Cuesta Ciscar

University of Aberdeen

Prof. dr. E. Alarcón Lladó

Universiteit van Amsterdam

The work presented in this thesis was financially supported by the Dutch Research Council (NWO).

ISBN: 978-94-6534-072-2

# Contents

<b>1</b>	<b>Introduction</b>	<b>1</b>
1.1	Electrochemistry . . . . .	1
1.1.1	The electrochemical cell . . . . .	2
1.1.2	The place exchange mechanism in oxidation-reduction cycles . . . . .	7
1.2	Scope of this thesis . . . . .	8
<b>2</b>	<b>Electrochemical Scanning Tunneling Microscope (EC-STM)</b>	<b>9</b>
2.1	Scanning Tunneling Microscope . . . . .	9
2.2	Electrochemical Scanning Tunneling Microscope . . . . .	11
2.2.1	Potentiostat for EC-STM . . . . .	12
2.2.2	Controller . . . . .	20
2.2.3	Analog Module . . . . .	21
2.2.4	Mechanical design . . . . .	27
<b>3</b>	<b>In situ STM Study of Roughening of Au(111) Single-Crystal Electrode in Sulfuric Acid Solution during Oxidation-Reduction Cycles</b>	<b>33</b>
3.1	Abstract . . . . .	34
3.2	Introduction . . . . .	34
3.3	Experimental . . . . .	36
3.3.1	EC-STM measurements . . . . .	36
3.3.2	Electrochemical Cell and Electrolyte . . . . .	36
3.4	Results and discussion . . . . .	37
3.4.1	Oxidation-reduction cycles of Au(111) without holding potential in double layer . . . . .	37
3.4.2	Oxidation-reduction cycles of Au(111) with holding the potential in double layer . . . . .	43

## Contents

---

3.4.3	Comparison of STM-derived roughening to Oxidation-Reduction Charge Density . . . . .	47
3.5	Conclusions . . . . .	51
3.6	Acknowledgement . . . . .	52
3.7	Supporting Information . . . . .	52
<b>4</b>	<b>Effect of Trace Amounts of Chloride on Roughening of Au(111) Single-Crystal Electrode Surface in Sulfuric Acid Solution during Oxidation-Reduction Cycles</b>	<b>53</b>
4.1	Abstract . . . . .	53
4.2	Introduction . . . . .	54
4.3	Experimental . . . . .	55
4.3.1	EC-STM measurements . . . . .	55
4.3.2	Electrochemical Cell and Electrolyte . . . . .	56
4.4	Results and discussion . . . . .	56
4.4.1	Oxidation-reduction cycles of Au(111) in 0.1 M H <sub>2</sub> SO <sub>4</sub> and 50 pM HCl . . . . .	57
4.4.2	Oxidation-reduction cycles of Au(111) in 0.1 M H <sub>2</sub> SO <sub>4</sub> and 10 pM HCl . . . . .	58
4.4.3	Oxidation-reduction cycles of Au(111) in 0.1 M H <sub>2</sub> SO <sub>4</sub> and 1 pM HCl . . . . .	63
4.5	Conclusions . . . . .	71
<b>5</b>	<b>Anisotropic Roughening of Au(111) Single-Crystal Electrode Surface in HClO<sub>4</sub> Solution during Oxidation-Reduction Cycles</b>	<b>73</b>
5.1	Abstract . . . . .	73
5.2	Introduction . . . . .	74
5.3	Experimental . . . . .	75
5.3.1	EC-STM measurements . . . . .	75
5.3.2	Electrochemical Cell and Electrolyte . . . . .	76
5.4	Results and discussion . . . . .	77
5.4.1	Oxidation-reduction cycles of Au(111) in 0.1 M HClO <sub>4</sub> . . . . .	77
5.4.2	Role of H <sub>2</sub> SO <sub>4</sub> Contamination in HClO <sub>4</sub> solution on Au (111) Surface Structure . . . . .	82
5.4.3	Role of HCl Contamination in HClO <sub>4</sub> solution on Au (111) Surface Structure . . . . .	84
5.4.4	General Discussion . . . . .	87

5.5 Conclusions . . . . .	90
5.6 Acknowledgement . . . . .	92
<b>A Supporting information for chapter 2</b>	<b>93</b>
A.1 Introduction . . . . .	93
A.2 Numerical Model (FLOW-3D) . . . . .	94
A.2.1 Geometry and Mesh . . . . .	96
A.2.2 Boundary conditions . . . . .	98
A.3 Results and discussion . . . . .	99
<b>B Supporting information for chapter 3</b>	<b>109</b>
B.1 Lifting the reconstruction for the experiment with holding the potential	109
B.2 HHCF result for the instant frames . . . . .	110
B.3 Curve fitting for OR charges . . . . .	110
B.4 Oxidation-Reduction charge density with holding the potential . . . . .	113
<b>C Supporting information for chapter 5</b>	<b>115</b>
C.1 Au(111) in 0.1 M HClO <sub>4</sub> . . . . .	116
C.2 Au(111) in 0.1 M HClO <sub>4</sub> and 10 µM H <sub>2</sub> SO <sub>4</sub> . . . . .	122
C.3 Au(111) in 0.1 M HClO <sub>4</sub> and 10 µM HCl . . . . .	126
C.4 Recorded CV on EC-STM . . . . .	130
<b>Bibliography</b>	<b>131</b>
<b>Summary</b>	<b>143</b>
<b>Samenvatting</b>	<b>145</b>
<b>List of publications</b>	<b>147</b>
<b>Curriculum vitae</b>	<b>148</b>
<b>Acknowledgements</b>	<b>150</b>



# Chapter 1

## Introduction

This chapter provides an overview of the theoretical foundation underlying the experimental techniques utilized in this thesis. Section 1.1 outlines the fundamental concepts and methods in electrochemistry.

### 1.1 Electrochemistry

The roots of electrochemistry trace back to the late 18th century through the experiments conducted by Volta and Galvani[1], marking the initial connection between chemistry and electricity. Over time, the definition and range of electrochemical science have undergone changes[2], and since the 1980s, the field of electrochemistry has experienced significant evolution. Many electrochemical (EC) experiments are conducted at the interface between distinct chemical phases, commonly involving an electronic conductor (the electrode) and an ionic conductor (the electrolyte). Typically, the electrode is a metal, and the electrolyte is a liquid solution containing a salt, acid, or base in water. At this interface, the characteristics of the two adjacent phases diverge significantly from those of the bulk. The process at this interface holds central importance and varies with the electric potential drop across it. In the case of excess charge on the metal surface, the ions with opposite charges on the solution side of the interface will compensate for this charge by creating the corresponding excess of cations or anions. Such a structure acts as a capacitor. Since the charge carrier concentration in the electrolyte is always lower than in a metal, the charge in the electrolyte expands diffusely (3 to 20 Å) into the solution. This charge distribution in a very narrow space is known as electrical double layer (EDL) and stands as a

## 1.1. Electrochemistry

---

fundamental concern in the field of electrochemistry. As is shown in Figure 1.1a, the EDL can be made up of several layers and the layer closest to the electrode surface is called the inner layer, which contains solvent molecules and ions or cations that are specifically adsorbed[3]. They make the inner Helmholtz plane (IHP) at a distance  $x_1$  from the electrode. Solvated ions can approach the metal to a distance  $x_2$  and their interaction with the electrode is only electrostatic, so it is independent of the ions type and the chemical properties of the electrode. They are called nonspecifically adsorbed and form the so-called outer Helmholtz plane (OHP).

Beyond the outer Helmholtz plane (OHP), the diffuse layer extends into the solution bulk. Within this three-dimensional space, nonspecifically adsorbed ions are distributed by a combination of electrostatic interactions and thermal motion. The thickness of the diffuse layer depends on several parameters, primarily the ionic strength of the solution and the electrode potential. The potential profile in the double layer is illustrated in Figure 1.1, denoted by a solid line for nonspecifically adsorbed anions and a dotted line for the specifically adsorbed ions [4]. In the case of nonspecifically adsorbed ions, the potential varies from the metal surface to the outer Helmholtz plane (OHP) linearly like a capacitor. But it does not drop linearly to the solution potential  $\varphi_s$ , as in the diffuse layer it drops off exponentially from  $\varphi_2$  to  $\varphi_s$ . In the other case, since more charge is accumulated on the electrode surface than the required charge by electrostatics, the potential overshoot to  $\varphi_1$  is lower than the bulk potential. To be able to compensate for this extra charge, the countercharge will be brought into the double layer.

### 1.1.1 The electrochemical cell

In the experiment, measuring an isolated interface is not feasible, and at least two electrodes separated by one (or more) electrolyte phases are required. This represents the most basic form of what is commonly known as an electrochemical (EC) cell. Within an electrochemical (EC) cell, an electrical current can be generated by a chemical reaction (Galvanic cell) or, conversely, an electrical current can drive a chemical reaction (electrolytic cell). The total reaction within an EC cell is typically divided into two half-reactions: reduction occurring at the cathode and oxidation taking place at the anode. Unlike redox reactions in solution, in the electrochemical (EC) experiments, oxidation and reduction take place at different locations, where the exchange of electrons specifically accrues on the electrodes. In the majority of electrochemical (EC) experiments in a research laboratory, a three-electrode cell is used, consisting of

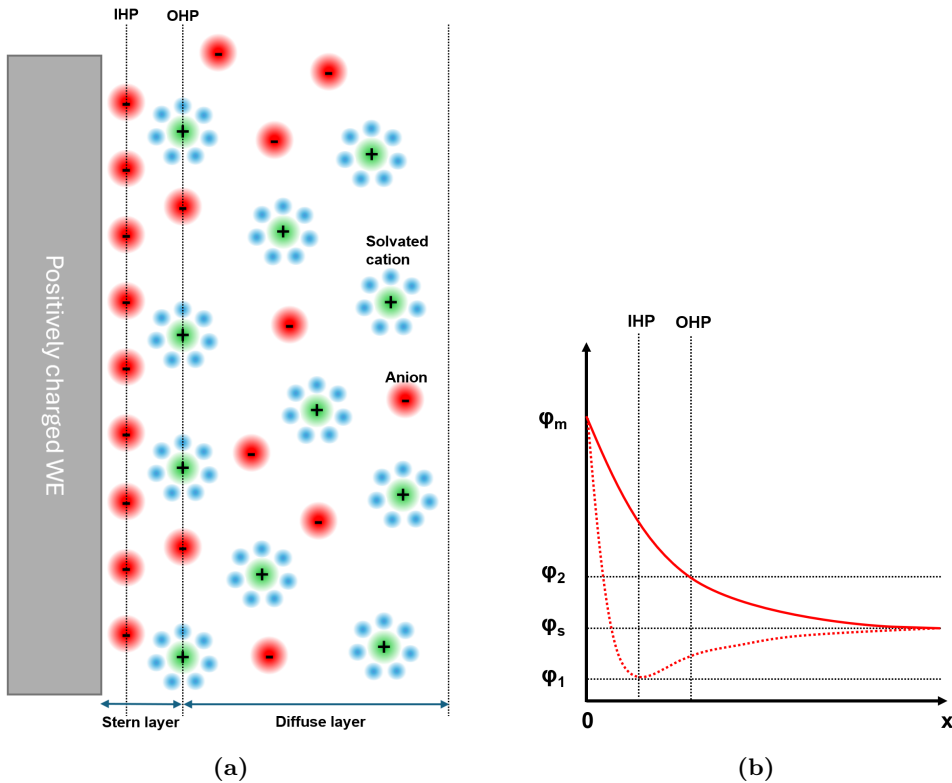


**Figure 1.1:** a) The model for the double layer region which contains the inner Helmholtz plane and the outer Helmholtz plane. b) Potential distribution near the electrode for non-specifically adsorbed anions as a solid line and specifically adsorbed anions as dotted line.

a working electrode (WE), reference electrode (RE), and counter electrode (CE). The working electrode (WE) is where the processes or reactions under study occur. Due to the movement of ions between the working electrode (WE) and counter electrode (CE), an electrical current flows through the cell and the potential of the working electrode (WE) is measured with respect to the reference electrode (RE). In other words, one can consider the reference electrode as a virtual ground for the electronics, so all the voltage differences can become meaningful for electrochemistry. Additionally, having just two electrodes (WE and CE) would entail the contribution of CE/electrolyte interface and electrolyte characteristics like resistivity on the applied potential on the working electrode. By adding the third electrode, we can exclude the CE/electrolyte interface contribution to the experiment and minimize the electrolyte resistance effects on the reactions under study. The potential of the reference electrode should

## 1.1. Electrochemistry

---

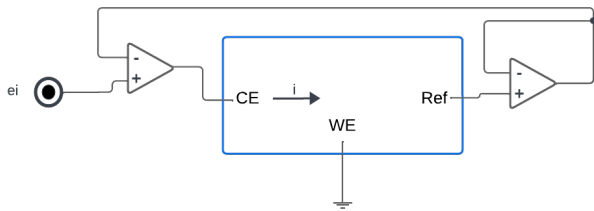


**Figure 1.2:** A very simple schematic of a potentiostat with three connections to the EC cell.

be well-defined, so there are many different types of reference electrodes for various experimental setups. Moreover, the reference electrode should not contribute to the current flowing in the EC cell. Thus the current on the reference electrode should be zero in the ideal case, but in practice, this is not possible. The best solution can be the usage of operational amplifiers in a voltage follower configuration. By reducing the reference current to a very low level, its contribution to the EC current flow will become negligible. The counter electrode (CE) is typically made out of an inert material. It is important that the electrochemical (EC) reactions occurring on it, do not interfere with the WE. The accurate control and measurement of the potential between the working electrode (WE) and reference electrode (Ref), as well as the current flowing between the working electrode (WE) and counter electrode (CE), are achieved using a device known as potentiostat. Figure 1.2 shows a very simple schematic of a potentiostat[3].

At electrodes, two types of processes can take place: faradaic and non-faradaic currents. Adsorption/desorption without charge transfer and the formation of the electrical double layer (EDL) involve no charge transfer across the metal-solution interface and are referred to as non-faradaic processes. Despite no charge crossing the interface, external currents can still flow when there are changes in potential or solution composition, just like the charging of a capacitor without having a conductive path between the capacitor's plates. Processes involving charge transfer across the metal-solution interface are named faradaic processes. Electron transfer in faradaic processes induces oxidation or reduction, governed by Faraday's law. Consequently, the flowing current is directly proportional to the reaction rate. The half-reaction for reduction (forward) and oxidation (backward) is shown in Reaction 1.1 where  $n$  is the number of electrons transferred during the reaction. The potential at which this reaction is in equilibrium under standard conditions is the standard equilibrium potential

of Ox-Red couple with the notation of  $E_{\text{Ox}/\text{Red}}^0$ . The standard potential is referred to the normal hydrogen electrode (NHE), which has standard equilibrium potential of zero, by convention.



The Nernst equation (Equation 1.2) describes how the equilibrium potential  $E_{\text{eq}}$  of the Ox/Red electrode depends on the thermodynamic activities ( $a_{\text{Ox}}$  and  $a_{\text{Red}}$ ) of its components.

$$E_{\text{eq}} = E_{\text{Ox}/\text{Red}}^0 + \frac{RT}{nF} \ln \frac{a_{\text{Ox}}}{a_{\text{Red}}} \quad (1.2)$$

Where  $R$ ,  $F$ , and  $T$  represent the universal gas constant, the Faraday constant and the temperature at which the reaction takes place. The thermodynamic activities of the species are usually replaced by their concentration, which is a reasonable approximation if the ionic strength of the electrolyte is low and constant. Thus Equation 1.2 can be rewritten as Equation 1.3, in which  $C_{\text{Ox}}$  and  $C_{\text{Red}}$  are the concentrations of the oxidized and reduced species.

$$E_{\text{eq}} = E_{\text{Ox}/\text{Red}}^0 + \frac{RT}{nF} \ln \frac{C_{\text{Ox}}}{C_{\text{Red}}} \quad (1.3)$$

By applying a positive or a negative potential to the electrode, one can lower or raise the energy level of the electrons in the electrode. At a negative potential with respect to the equilibrium potential, electrons are thermodynamically favored to move from the electrode to occupy the lowest unoccupied molecular orbital (LUMO) of  $A$  in the electrolyte. As a consequence,  $A$  will be reduced to  $A^-$  and cause a negative current flowing in the system. By convention, if reduction takes place on an electrode, the electrode is called cathode and the corresponding reduction is named cathodic current. On the other hand, oxidation of  $A$  to  $A^+$  will occur only if a potential positive with respect to the equilibrium potential is applied, thermodynamically favoring the electron to transfer from the highest occupied molecular orbital (HOMO) in the electrolyte to the electrode. The electrode is called anode and the corresponding positive current is the anodic current. This oxidation-reduction process is shown in Figures 1.3b and 1.3a respectively.

Many parameters play an important role in the kinetics of electrode reactions and the rate of electron transfer is just one of them. For instance, mass transfer limitations, and chemical reactions before and after the electron transfer, can also influence the overall rate. The rate constants for electron transfer at the electrode surface, are influ-

## 1.1. Electrochemistry

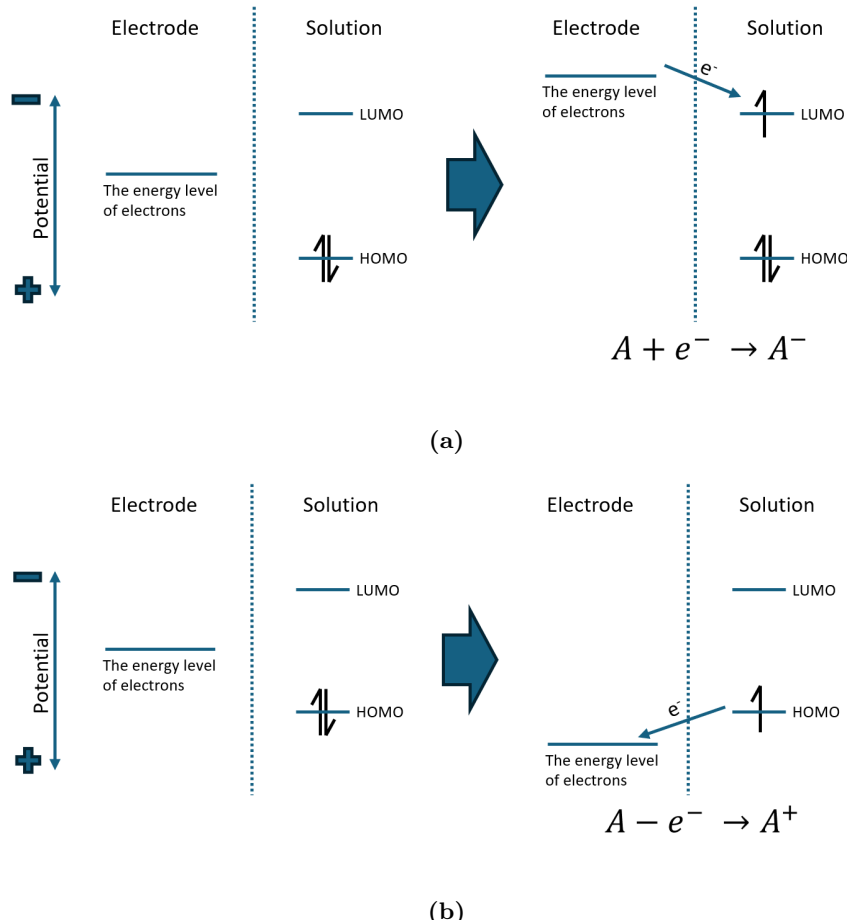


**Figure 1.3:** a) Reduction and b) oxidation process of A in a solution. By changing the applied potential to the electrode, depending on the magnitude and the sign of the potential, the electron can either be taken from the highest occupied molecular orbital or it can be transferred into the lowest unoccupied molecular orbital.

enced by the applied potential. Recording the current as a function of the potential, typically represented as i-E curves, can help to obtain proper information about these processes. There are different types of EC experiments, classified by the parameter which is kept constant, controlled, and measured. By applying a constantly varying potential to the electrode and recording the current flow, so-called cyclic voltammograms (CVs) can be recorded. The rate of potential change is called scan rate and is defined by  $s = \frac{dE}{dt}$ . A cyclic voltammogram contains forward and backward scans. If only one scan direction is applied, the technique is called linear sweep voltammetry. At a sufficiently slow scan rate, the obtained i-E curve is called the polarization curve.

### 1.1.2 The place exchange mechanism in oxidation-reduction cycles

During oxidation-reduction cycles, electrode surfaces can change due to atomic rearrangements/replacements. One of the key processes responsible for these changes is the place-exchange mechanism, where metal atoms swap positions with oxygen-containing species (such as oxygen or hydroxide) during oxidation at high enough potentials. During the cathodic voltage sweep, these oxygen species are removed, but the displaced metal atoms often do not return to their original positions. This leads to irreversible changes in the surface, including adatom and vacancy island formation.

Understanding the effects of place exchange mechanism is critical for optimizing electrode materials in catalysis, energy storage, and corrosion resistance. For example, in fuel cells and electrocatalysis, surface restructuring can enhance or diminish catalytic activity, depending on the degree of atomic rearrangement. Similarly, in electrochemical sensors, surface stability is essential for maintaining consistent performance over time[5]. Experimental techniques such as electrochemical scanning tunneling microscopy (EC-STM)[6], electrochemical atomic force microscopy (EC-AFM)[7, 5], X-ray scattering (SXS)[8], and X-ray photoelectron spectroscopy (XPS)[9] have provided valuable insights into how place exchange occurs at the atomic level. However, challenges remain in fully controlling this mechanism to engineer more durable and efficient electrode materials. Researches aim to develop strategies for stabilizing surfaces during ORCs, minimizing unwanted structural changes, and enhancing electrochemical performance across various applications.

## 1.2. Scope of this thesis

---

### 1.2 Scope of this thesis

During electrochemical experiments involving various techniques, the electrode surface may undergo minor or significant transformations. Monitoring these surface transformations in real time while the electrochemical reactions are in progress is the primary objective of this thesis. Specifically, we focus on the evolution of the Au(111) surface under different electrochemical conditions (e.g., various electrolytes, delays) by applying oxidation-reduction cycles. Through this study, we aim to gain deeper insights into the dynamic changes occurring on the electrode surface, which are crucial for understanding electrochemical processes and optimizing electrode performance. **Chapter 2** is devoted to the design of the electrochemical scanning tunneling microscope with the desired specifications. The mechanical parts and the electrical modules (like potentiostat, controller, and analog module) are shown and discussed. Supplementary information for the flow-cell design is available in **Appendix A**. In **Chapter 3**, we studied roughening of Au(111) single-crystal electrode in 0.1 M sulfuric acid during 200 oxidation-reduction cycles with the developed EC-STM. In these experiments, we applied two experimental procedures called "without holding the potential" and "with holding the potential". Holding the potential cause some delays during the ORCs and its effects were studied. Supplementary information for these experiments is available in **Appendix B**. In **Chapter 4**, we studied the effect of different concentrations of chloride in 0.1 M sulfuric acid during 200 ORCs. The studied concentrations of chloride are 50, 10, and 1  $\mu$ M. The surface reacts differently to these changes and in the lowest concentration, some surprising behavior was observed. Finally, **Chapter 5** is about roughening of Au(111) single-crystal electrode in 0.1 M  $\text{HClO}_4$  as the result of ORCs. Au(111) surface reacted in three counter-intuitive and different manners. Some areas started to get roughened (similar to pure  $\text{H}_2\text{SO}_4$ ), some regions started to get dissolved and form vacancy islands, and others did not go through major changes over the ORCs. The knowledge from Chapters 3 and 4 helps us to rationalize the unanticipated results. The provided supplementary information can be found in **Appendix C**.

# Chapter 2

2

# Electrochemical Scanning Tunneling Microscope (EC-STM)

This chapter consists of two sections. Section 2.1 introduces the basic working principle of a Scanning Tunneling Microscope (STM). After familiarizing with STM, section 2.2 describes the design of the Electrochemical STM (EC-STM) and the main modules used for the work described in the rest of the thesis.

## 2.1 Scanning Tunneling Microscope

Binning and Rohrer invented the first Scanning Tunneling Microscope (STM) in 1981 [10, 11], which for the first time allowed surface scientists to directly image the real spatial structural and electronic properties of their surfaces. Depending on the type of experiment, STM can be done on surfaces in vacuum, air, or a liquid. An additional possibility is to perform so-called scanning tunneling spectroscopy, which gives information about the density of electrons as a function of their energy[12, 13]. It also can be used to manipulate and reposition the atoms[14]. After the emergence of STM, other scanning probe techniques like atomic force microscopy (AFM) were developed. The operation of STM relies on electron tunneling, a quantum mechanical phenomenon enabling electrons to tunnel through an insulating barrier between two electrodes. As a result of the applied bias potential  $V_{Bias}$  to the electrodes, tunneling can take place

## 2.1. Scanning Tunneling Microscope

---

and the corresponding tunneling current  $I_t$  can be measured by a proper amplifier. This tunneling current is a function of the distance between the electrodes, the tunneling bias potential, and the density of states (DOS) of the electrodes. Thereby, it contains information about the electrode distance and the electronic structure of both electrodes[15].

Figure 2.1 shows the working principle of a scanning tunneling microscope. An atomically sharp metallic tip (first electrode) is positioned close to the conductive or semi-conductive sample (second electrode). If the tip-sample distance is reduced to a few Å, the tip and the sample wave functions overlap. If a bias potential is applied at this condition, the electrons can tunnel from the tip to the sample or vice versa, depending on the sign of the applied potential. The majority of the tunneling current occurs through the atoms at the apex of the tip, primarily due to its exponential dependence on the tip-sample distance. This results in a distinct localization of the tunneling current and, as a consequence, contributes to the high-resolution capabilities of the STM. The tip is mounted on a piezoelectric tube which allows very precise movement of the tip in 3 dimensions. Via the piezoelectric effect, precise movement of the tip is easy to achieve. During the measurement, the tip can move in the X-Y plane to scan the area under study and the z-axis can be used to measure or control the tip-sample distance. There are two main working modes for STM: namely constant current mode and constant height mode, of which the first one is used most frequently. In the constant current mode, the tunneling current is being monitored as a function of the X-Y position of the tip and by using feedback, the tunneling current will be kept constant by applying changes in the tip height. Thus, by recording the displacement of the tip in the z-axis as a function of the X-Y position, one can extract the topography of the sample surface with atomic resolution. The tunneling current in STM is typically quite low, ranging from 0.01 to 50 nA. Consequently, the current amplifier plays a crucial role in the STM functionality by magnifying this small tunneling current and transforming it into a measurable voltage, because for the feedback system or the main controller voltage level that tiny current is not useful. The characteristics of the current amplifier significantly impact the overall performance of the STM, which is influenced by factors such as thermal noise, stray capacitance, and the inherent characteristics of electronic components. The next required part is the controller which generates the scanning signals of the piezo tube and it usually contains a logarithmic amplifier and a PID controller to adjust the height of the tip during the scans. The controller typically can be connected to a PC to gather the information and plot the images. Since the working voltage range of the piezoelectric tube is much higher than the working voltage

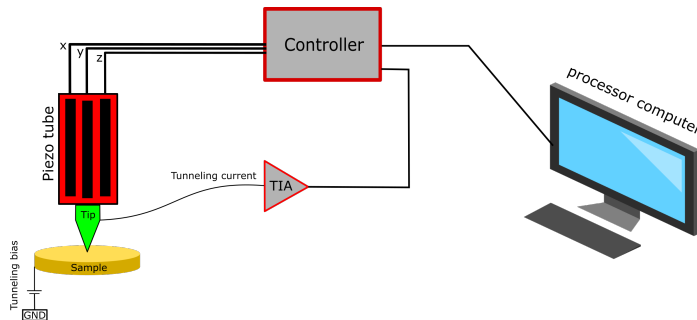


**Figure 2.1:** Working principle of an STM. The applied potential to the piezoelectric tube can move the tip in three dimensions and the change in current on the tip which can be measured by a transimpedance amplifier (TIA), can provide the input for the feedback signal to adjust the tip-sample distance (constant current mode) or a signal to calculate the distance between the tip and the sample (constant height mode).

of the controller, an extra-high-voltage amplifier is essential to multiply the low-level output voltage of the controller by a constant coefficient. There are many different types of mechanical designs for an STM like, single-tube STM, the beetle, the walker, and many others[15]. Each design has its own strong and weak points and it can be chosen for the specific aim of the research. Among them, single-tube is the most common because of its small size and high natural resonance frequency which makes the mechanical design and vibration isolation system simpler. In this design, the piezo scanner tube is fixed to the central portion of a robust and rather heavy metal cylinder. The tip can be mounted on the apex of the piezoelectric element. This metal cylinder, including the piezoelectric element, is called the scanning head. The head can be mounted on three screws with polished spherical ends, and the screws should be fixed on the base plate where the sample is securely fixed. Two screws can be used for coarse approaching steps to move the tip very close to the sample surface. Subsequently, precise positioning can be achieved by controlling the third screw for fine adjustments. Typically, a step motor drives the screw and helps to deploy automatic approach procedures.

## 2.2 Electrochemical Scanning Tunneling Microscope

The working principle of a scanning tunneling microscope and regular electrochemical experiment in an EC cell has been discussed in the previous two sections. For an in-situ scanning tunneling microscope for electrochemistry, combining a normal STM

## 2.2. Electrochemical Scanning Tunneling Microscope

---

and EC experiment setup is desirable. By achieving this goal, one can study the sample topography of the electrode surface on a specific spot with atomic resolution before, during, and after electrochemical experiments. A simple schematic of this setup is shown in Figure 2.2. The scanner head (piezoelectric tube), SPM controller, and processing PC are the main parts of the STM setup, and by adding potentiostat, electrochemical cell, and electrodes, an EC-STM can be built. To integrate an STM with an EC setup, multiple electrical modules with specific characteristics, mechanical parts, and software are necessary. In the following sections, these subjects will be covered.

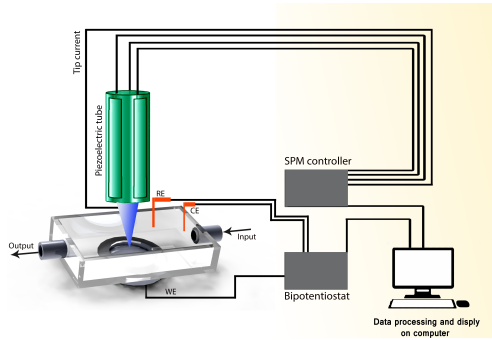


**Figure 2.2:** Simple schematics of an Electrochemical Scanning Tunneling Microscope (EC-STM).

### 2.2.1 Potentiostat for EC-STM

The reason for having a potentiostat in a normal electrochemical experiment was discussed in section 1.1. Since the scanning probe (tip) as an extra electrode is needed for an EC-STM, an additional requirement is essential for the potentiostat. The primary extra capability is the ability to independently adjust or tune the working electrode voltage with respect to the tip. In conventional electrochemical experiments, the voltage difference between the working electrode and the reference electrode is important while the voltage of the working electrode has no importance by itself and it can be grounded or remains float. However in an EC-STM, since a voltage difference (tunneling bias) is needed, we must be able to control the WE potential separately so that it does not interfere with the applied electrochemical potential. There are different types of potentiostat with various working principles and thus a comparison is inevitable for making a decision for the EC-STM potentiostat. In the following

section, the three main categories will be brought up.

### Resistive-Based Potentiostat

The first type and the most common type of potentiostat contains a resistor and operational amplifier to control the voltage difference between the working electrode and the reference electrode and measure the current flowing through the electrochemical cell. Because of the circuit configuration, the current passing through the working electrode has to pass through the resistor  $R$  and this will make a voltage difference at the output of the operational amplifier which has a linear correlation with the current and this is called transimpedance amplifier. The formula for the output can be written as:

$$V_{\text{out}} = -I_{\text{EC}} \times R \quad (2.1)$$

where  $V_{\text{out}}$  is the output voltage and  $I_{\text{EC}}$  is the electrochemical current in the cell. The simple schematic of this configuration is shown in Figure 2.3. It is also possible to implement the transimpedance amplifier on the counter electrode since the current passing through the working electrode is theoretically equal to the current at the counter electrode if we consider the current at the reference electrode negligible. However, doing so can increase the complexity and noise level of the system since more active components will be needed for the entire potentiostat configuration. Furthermore, stability issues may arise as the transimpedance amplifier is integrated within the primary feedback loop. A weak point to be considered for this configuration is its inefficiency for the experiments that need high current because the power in the resistor  $R$  in Figure 2.3 will turn into heat. Considering the formula for the electrical power loss in a resistor as  $P = RI^2$  where  $I$  is the electrochemical current passing through the EC cell, this reduces the efficiency of this circuit. Lower  $R$  values result in lower power loss but reduce the current reading precision. Thus, there is a trade-off between the electrical power loss and the current reading precision. However, the precision and frequency response of this configuration are satisfactory.

The other approach can be placing a resistor in series in the path of either the counter electrode or working electrode. In the case of the former, the working electrode should be connected to the ground with a resistor  $R$  in series. The passing current will make a voltage difference and this voltage can be measured by a voltage follower. However, it is important to note that this voltage difference will also alter the working electrode voltage, which is not desirable. In other words, the WE voltage will become a function of the EC current. To compensate for this unwanted effect, an extra circuit

## 2.2. Electrochemical Scanning Tunneling Microscope

---

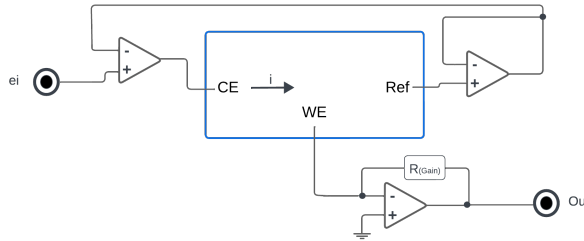


**Figure 2.3:** Resistor-based potentiostat schematic containing a resistor and operational amplifier.

is needed. In brief, the main issue with this approach can be the lack of enough precision for very small currents. There is a trade-off between the precision and the voltage difference introduced into the measurement.

### Capacitive-based Potentiostat

An alternative approach is using a capacitor in the current sensing circuit, instead of a resistor. It is well known that the voltage across a capacitor is equal to the integrated current passing through the capacitor over time. Thus by reading the capacitor voltage one can calculate the total current passing through. As shown in Figure 2.4, it is essential to discharge the capacitor to avoid current blockage in the case of a fully charged capacitor. Thus, a transistor or CMOS switch will be turned on if the capacitor's voltage reaches a certain voltage threshold. The frequency of the applied pulses to the switch can be a proper parameter for current calculation. This technique can be used in either the working electrode or the counter electrode. This method is capable of increasing the efficiency of the potentiostat (the ratio of the electrical energy used in the electrochemical cell to the total energy consumed by the potentiostat). Thus, it is more favorable for high current measurement. Another advantage is the capability to measure different current ranges without the need for changing the capacitor. By contrast, for the aforementioned method of resistor-based potentiostat, changing the resistor is essential. For very high-accuracy experiments with this configuration, one can use a delta-sigma modulator as a recovery module[16]. The shortcoming of this method can be the leakage current in the capacitor and more importantly, the applied pulses on the switch can impose some noise into the electrochemical system.

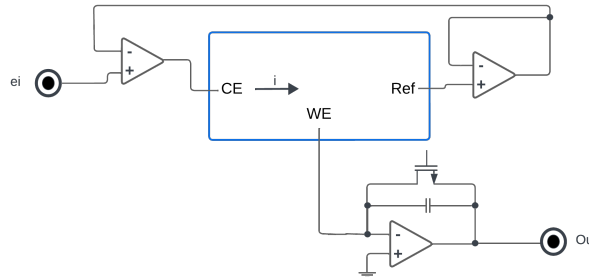


**Figure 2.4:** Capacitor-based current sensing circuit.

### Current Mirror-Based Potentiostat

To enhance stability and mitigate the impact of discharging pulses on the potentiostat system, a current mirror method can be used which is shown in Figure 2.5. In this method, by the proper components, a mirrored current of the either working electrode or counter electrode is made and this current can be measured by a transimpedance amplifier configuration or capacitive-based current sensing. By implementing this method, the current sensing system and the main electrochemical current will be separated and the current sensing circuit will not be able to disturb the performance.

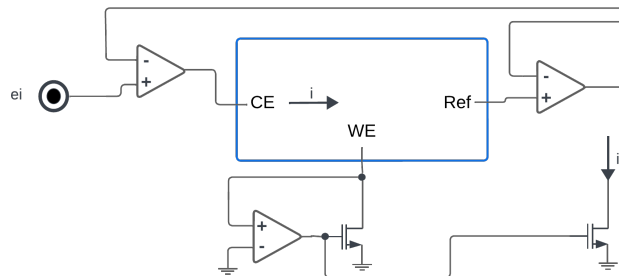


**Figure 2.5:** Current mirror method for current measurement in a potentiostat.

### Schematics and working principle of the potentiostat

Between the three aforementioned modes, the resistor-based potentiostat seems the best fit for an EC-STM for the following reasons: First, the surface area of the sample under study is a few squared millimeters, thus the magnitude of current will be from

## 2.2. Electrochemical Scanning Tunneling Microscope

---

nano ampere to a few milli-ampere range. Thus, the energy loss of the resistor in the transimpedance configuration can be negligible. Second, this method does not add extra noise (like noise coming from pulses on the switch) to the experiments, and avoiding noise is crucial in an EC-STM. Finally, this configuration allows a fine control of the working electrode potential without affecting the EC potential which is crucial for an EC-STM.

Figure 2.6 shows the schematics of the designed potentiostat. On the left-hand side, four inputs are shown. The two top inputs will set the electrochemical voltage and can accept two AC and DC signals. The DC input is suitable for a low-speed changing waveform, like a conventional triangular waveform for a cyclic voltammogram. The AC input can be used for other fast-changing signals and it helps to deploy ACV techniques. The two bottom inputs can adjust the working electrode potential, which in a conventional potentiostat is either grounded or remains floating. With this configuration, the WE potential can be adjusted precisely by a DC voltage or with an AC potential to apply modulation techniques to the tunneling bias. All the inputs are passed by a second-order active low pass filter to reduce the unwanted noises at the inputs. The working electrode is connected to a transimpedance amplifier to convert the current on the WE into a readable voltage which can be read at WE  $I_{Out}$  connector. There are seven different current ranges available and can be changed digitally from  $1\mu A$  to  $200mA$ . With  $1\mu A$  as the current range setting, nano ampere currents can be read. These gain settings can also influence the bandwidth and phase margin of the potentiostat. As a rule of thumb, higher transimpedance gains will cause a reduction in the bandwidth. Another operational amplifier with a voltage follower configuration is connected to the WE to read the actual voltage. This is important because the bandwidth limitations and wrong gain settings can lead to strong deviation from the asked WE potential. To improve the reliability and precision of the potentiostat the WE potential is always read directly by the circuit. This voltage is detectable at the WE  $U_{Out}$  connector. The reference electrode is directly connected to the non-inverting input of the operational amplifier with a voltage follower configuration. This makes reading of the Ref potential possible with great precision and the output is connected to Ref  $U_{Out}$ . The final part is the counter electrode driver module which reads the EC potential setpoint from the active filter output, the reference electrode voltage, and the actual working electrode potential to adjust the counter electrode voltage so that the voltage difference between the working electrode and the reference electrode matches with the asked EC potential. The bandwidth of this module is adjustable with four digitally controlled channels. The main specification of the designed potentiostat is as

follows:

- Tunable bandwidth for CE.
- Tunable bandwidth and gain for WE.
- Maximum 5 picoampere RE input current (very low ohmic error).
- Second-order low-pass active filter on inputs.
- AC and DC inputs for each channel (AC for modulation and DC for voltage sweep).
- 200 mA continuous output current.
- Control of CMOS switches with 10 ns resolution.
- Everything is controlled by the *FPGA* (no selector or knob) and the instrument can be run remotely.

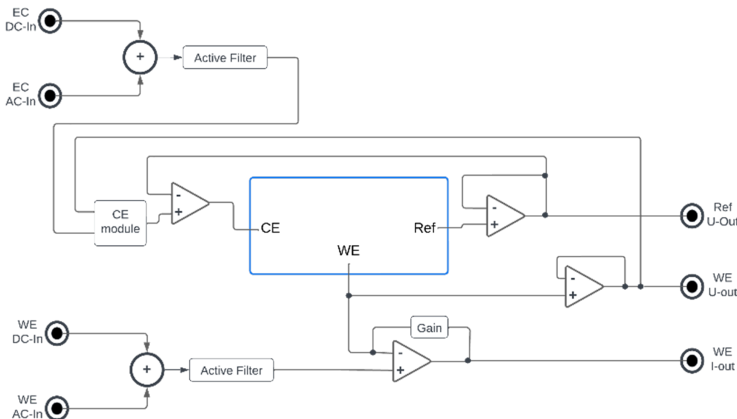


**Figure 2.6:** Simple schematics of the potentiostat with the cell containing the electrodes in the middle. On the left, there are four input channels, and on the right, three outputs are shown.

After finishing the schematic design, the printed circuit board, which is shown in Figures 2.7a (upper side) and 2.7b (lower side), was developed. Figure 2.7c shows the final product with a metallic box to reduce the electromagnetic noise during the precise experiments. There is one National Instrument DAQ card on the right side of

## 2.2. Electrochemical Scanning Tunneling Microscope

---

the potentiostat which contains four digital-to-analog converters and four analog-to-digital converters with 16 bits resolution. Thus, all the waveform can be generated by this module and be passed to the potentiostat and all the output voltages from the potentiostat can be read by the DAQ card. Home-built software is needed to run electrochemical experiments with different techniques, which will be discussed in the next section.

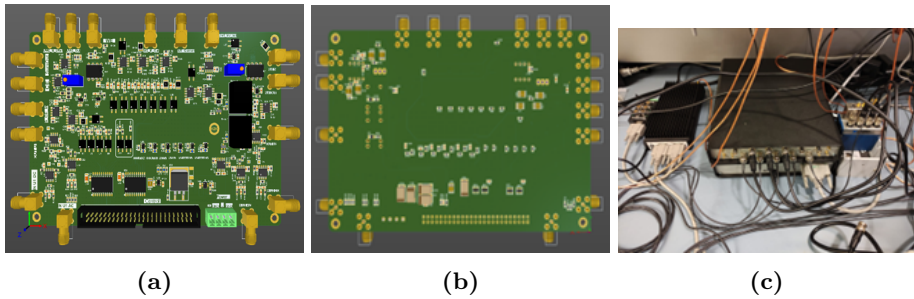


**Figure 2.7:** The designed printed circuit board top and bottom (a and b) and the final module in a metallic box (c).

### The potentiostat software

As was explained in the previous section, the potentiostat is connected to a NI DAQ card, and a home-built software was developed to facilitate the generation of the working electrode and other voltages and read, process, plot, and save the measured signals. The basic version of the software contains two fundamental techniques for electrochemistry experiments, namely chronoamperometry and cyclic voltammetry. Figure 2.8 depicts the window for the chronoamperometry and basic potentiostat settings like the gains and bandwidth. On the top left-hand side, the CA technique can be started and stopped by run and stop buttons, respectively. Below these buttons, the working electrode potential and the electrochemical potential can be set by the operator and those voltages will be applied immediately while the software is running. There is a cluster containing four boxes where it shows the value of the working electrode potential (tunneling bias voltage), electrochemical voltage, electrochemical current on WE, and current on the tip. On the bottom, the real-time plot can be screened during the experiment. On the top right-hand side, There is a window for adjusting the settings, such as turning the potentiostat into an open circuit configuration, adjusting the counter electrode bandwidth, and working electrode transimpedance gain and bandwidth. This window is usually used to start many conventional EC experiments

## Chapter 2. Electrochemical Scanning Tunneling Microscope (EC-STM)

2

since the first step can be closing the circuit and applying a voltage (usually in the double-layer potential window).

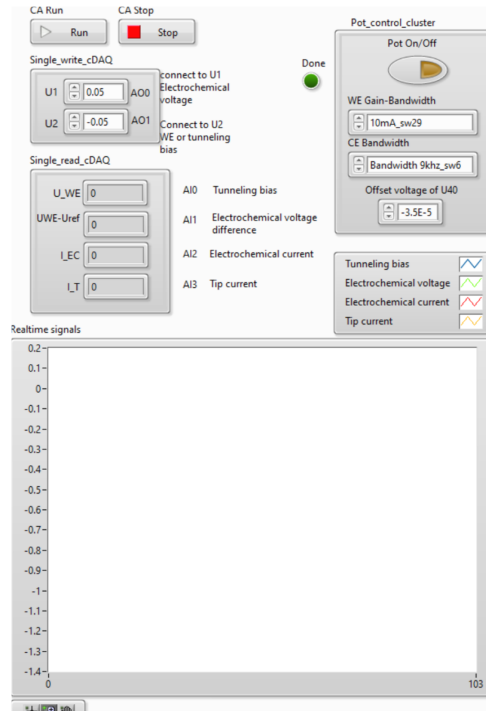


**Figure 2.8:** Chronoamperometry window of the potentiostat software

The next window in Figure 2.9 is designed for measuring a cyclic voltammogram or applying a voltage sweep from a certain voltage to either higher or lower potential. On the left-hand side, the operator can change the start potential for the CV, vertex one and vertex two, end potential, scan rate in volts per second, number of scans that need to be applied, tunneling bias voltage during the cycles, and oversampling factor. The parameters are self-explanatory except the last one. Over over-sampling factor tells the software how many data points need to be recorded on all the inputs for each applied data point on the output (WE and EC potential during the CV and LVS experiments). By elevating this value, a greater number of data points can be captured, potentially allowing for the reduction of inherent electrical noise through methods such as averaging over-sampled data points or implementing digital filters. After adjusting all the items, the run button can be pressed and the CV will be recorded and plotted in real-time on the large window. The recorded data can be

## 2.2. Electrochemical Scanning Tunneling Microscope

automatically saved with the description and experiment name on the hard drive for further analysis.

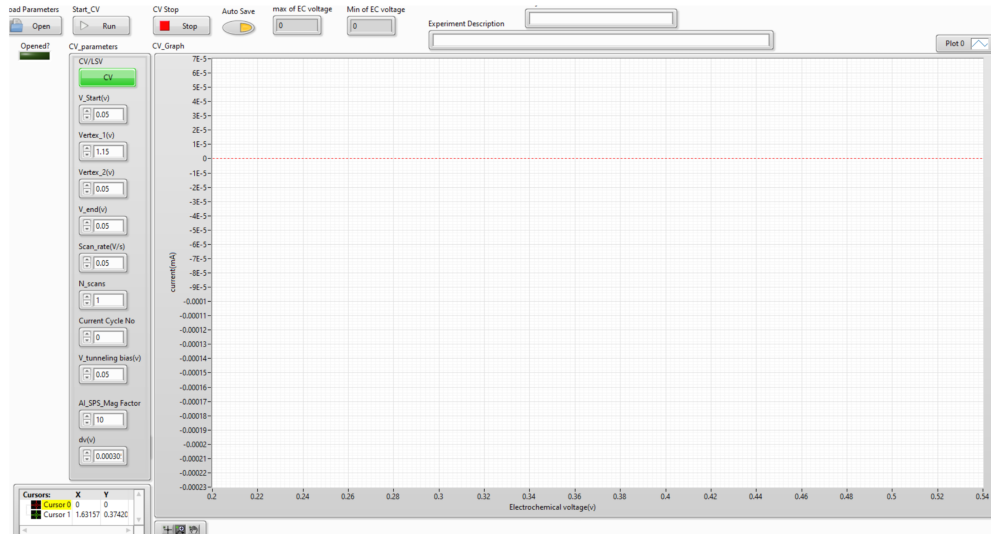


**Figure 2.9:** Cyclic voltammogram window of the potentiostat software.

To make sure the potentiostat (the electronics and the software) is working flawlessly, a  $10\text{ k}\Omega$  resistor and a  $0.1\text{ }\mu\text{F}$  capacitor were connected separately between the WE and CE, and the reference electrode was connected to the CE. Then a cyclic voltammogram was recorded to test the performance under capacitive and resistive loads. The observed outcomes aligned with expectations.

### 2.2.2 Controller

The other essential module is the controller which should be able to perform many tasks. First, the controller generates scanning waveforms for the x and y piezoelectric elements. These waveforms contain one fast-changing triangular waveform for movement in the X direction and one slow-moving waveform for the Y direction. For each complete triangle, the tip will move in the X direction, reach the maximum distance, and then come back to the original starting point. By applying a very slow changing voltage sweep (or triangular waveform in case of scanning upward and downward continuously) the tip location in the Y axis will be modified. There are many parameters for these waveforms that the controller must be able to modify like frequency of the triangular waveform, voltage magnitude for the waveform, and offset potential for X

and Y signal. Second, the height of the tip needs to be adjusted based on the tunneling current on the tip. Therefore, a feedback signal needs to be generated to keep the tip current as close as the set current setpoint. It can be done by PID controller and it can be implemented inside the SPM controllers. Thus, the controller will generate the feedback signal to control the height of the tip and it also records the values for each data point. Finally, by having the feedback signal value along with the X-Y waveform data, the controller can generate and plot the topographical image of the scanned surface. This task can be done in the controller software installed on a PC. It is important to keep in mind that there are many more technical functionalities for modern SPM controllers that we did not discuss in this section. Commercial SPM controllers are available nowadays and they can match the requirements of many projects. For many reasons, open-source software for the controller is very useful since each instrument needs specific modifications in the software for a smooth operation. For instance, for the coarse approach mechanism, the controller should communicate with the actuator's module, and having access to the source code is very helpful in modifying the software. Thus, MK3 controller from Soft dB company, as shown in Figure 2.10, was purchased and used. There are controllers with better precision, speed, and more sophisticated electronics but considering the price and having no access to the source code, could prevent us from employing them for this instrument. There are eight inputs and eight outputs with 16 bits of precision on this controller. The channels can be assigned to different input and output signals.



**Figure 2.10:** Open-Source SPM Controller, Model MK3.

### 2.2.3 Analog Module

The analog module was designed and manufactured to take care of all the analog operations on the input and output signals. This module has two main parts and each part has its sub-modules. The first part is called “XYZ modules” and is for all the

## 2.2. Electrochemical Scanning Tunneling Microscope

---

analog operations on control signals for the piezoelectric in the X, Y, and Z axis. The second part is related to the generation of control signals and some necessary arithmetic operations on the tunneling current signal. These two parts will be discussed in more detail in the following.

### X, Y, and Z modules

The controlling signals for X, Y, and Z can be made in the main controller but more essential operations are needed. First, since the controller is capable of generating signals from -10 to + 10 volts with 16 bits precision, in some experiments it is required to reduce the voltage span to increase in precision further. One application for this operation is precision improvement for small scan areas and atomically flat surfaces. In this case, the instrument should have a very high resolution in the X, Y, and Z directions. This can be achieved by division of the signals by a certain coefficient. Second, in the case that one wants to zoom in on a small area (compared to the total travel range of the piezoelectric tube), it is important to separate the scanning signal and the offset signal. By applying this, one can record high-precision pictures on a small area while having access to the whole travel range of the piezoelectric tube. The offset signal is also useful for compensating the thermal drifts in all three directions during long experiments. Moreover, in some cases, one needs to apply some modulation in different directions with a certain frequency. So, external modulation signals need to be added to the offset and scanning signals. Third, the out-of-range potential of the piezo is damaging and needs to be avoided. Since commercial high-voltage amplifiers usually have a fixed gain value, it is wise to have good control on the output voltage levels. Fourth, a high order low pass filter can reduce the voltage noise level on the output since the output of this module will be connected to the high voltage amplifier, the voltage noise will be magnified by the gain value of the high voltage amplifier and this magnified noise can reduce the precision of the tip location in three axes. Additionally, the low pass filter can avoid the first fundamental resonance frequency of the piezoelectric tube to avoid unwanted oscillation during the experiments. The general specifications of the module are as follows:

- Differential or single-ended signals on all of the inputs.
- Ultra-low noise linear voltage regulators on the power lines.
- Ultra-low noise and drift +10 and -10 volts reference for the offsets.
- Adjustable minimum and maximum voltage for the low pass filter to limit the output voltage (to avoid damaging the piezo).

- 7<sup>th</sup> and 8<sup>th</sup> order low pass filter to reduce the noise and cut the sharp edges of the scanning waveform. The cutoff frequency and the topology of the low-pass filtered can be designed and implemented as per the requirements of the project.
- The offsets and the attenuation coefficient are controlled by a computer in 256 steps (LabVIEW or other languages).
- The maximum bandwidth of the attenuators is 500 kHz. If higher bandwidth is required, a regular potentiometer can be installed.

Since the requirements for X and Y directions are almost identical, the X and Y modules are identical in terms of the circuit board, but the filters and coefficients can be tuned separately. It is possible to set up each module in two different modes, which are shown in Figures 2.11a and 2.11b. The functionality of the first mode is as follows. There are two external inputs with the capability of accepting differential and single-ended signals. Then the input signals can be magnified by a constant coefficient (the minimum coefficient value can be one) and then there is a voltage divider on the path of “In 1” input. So, the scanning waveform from the main controller can be connected to this input and will be divided by the desired value. There is a dedicated output connection named “out 1” for this signal. The second input can be used as a separate offset signal from the controller or in case of any modulation in X and Y directions, the modulation signal can be connected here. There is also a digitally controlled offset value which is generated internally. The value can be tuned by the operator or the main controller software in case of integration of this module with the controller. Then the three signals go to the voltage adder amplifier and the output is passed through an eighth-order low-pass filter for the aforementioned purposes. The final output is accessible on the “Out 2” connector. In the second mode, the sequence of the operations is different as it can add the two input signals after the magnification and pass it through the voltage divider. Thus, this mode can reach gains lower than one for the two inputs. This mode can be more helpful for applications with small modulations in the X-Y plane.

The next part is the Z module, which has four modes and each of them is configurable as per the requirements of the project. Compared to the XY modules, this module has more functionality and extra functionality usually comes with more complexity. The four working modes are shown in Figure 2.12. One additional input is considered for the Z module compared to the X and Y modules in the case of different kinds of modulation. Thus there are three inputs for external signals either differential or single-ended and two single-ended outputs. The first mode (Figure 2.12a) is very

## 2.2. Electrochemical Scanning Tunneling Microscope

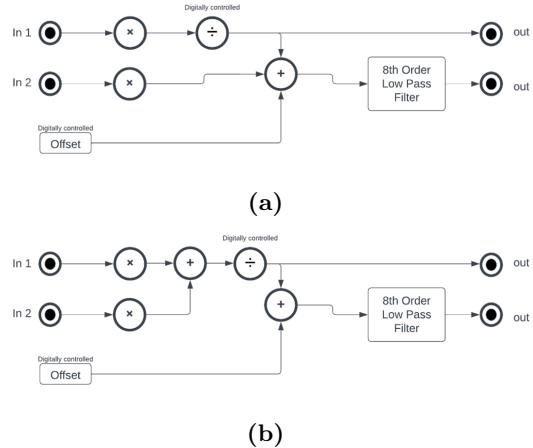


**Figure 2.11:** Simple schematic for the X, and Y modules for a) first mode, b) second mode

similar to the first mode of the X-Y module, except for the fact that there is one more input “In 3” and the signal can be multiplied and added to the output of the low pass filter. The summation signal is connected to “out 2”. As described, the third input can get bypassed from the low pass filter and it can be beneficial for modulations with a frequency higher than the cutoff frequency of the filter. This can avoid any phase shift and change in modulation amplitude. The second mode (Figure 2.12b) is similar to the X-Y second mode and we can apply division on the summation signal of inputs one and two. The third input works as it was described above. For the third and fourth modes (Figures 2.12c and 2.12d), the third input is added to the other signals and the result is passed onto the low-pass filter. If the modulation frequency of the modulation is lower than the cutoff frequency of the filter, these modes can be useful. The difference between the third and fourth modes is the ability of signal division on “In 2”, as it was discussed above. Choosing the best working mode depends on the experimental requirements and many other design parameters like the modulation frequency, amplitude, low-pass filter frequency, low-pass filter topology, resonance frequency of the system, etc.

### Abs, Log, PID with a Low-pass filter

The tunneling current can flow in two directions depending on the polarity of the tunneling bias, thus positive and negative signals are possible on the output of the pre-amplifier. The opposite directions for negative and positive signals can cause trouble for the feedback loop. There are two solutions for this. First: flipping the signs of the tunneling setpoint and changing the polarity of the output signal of the

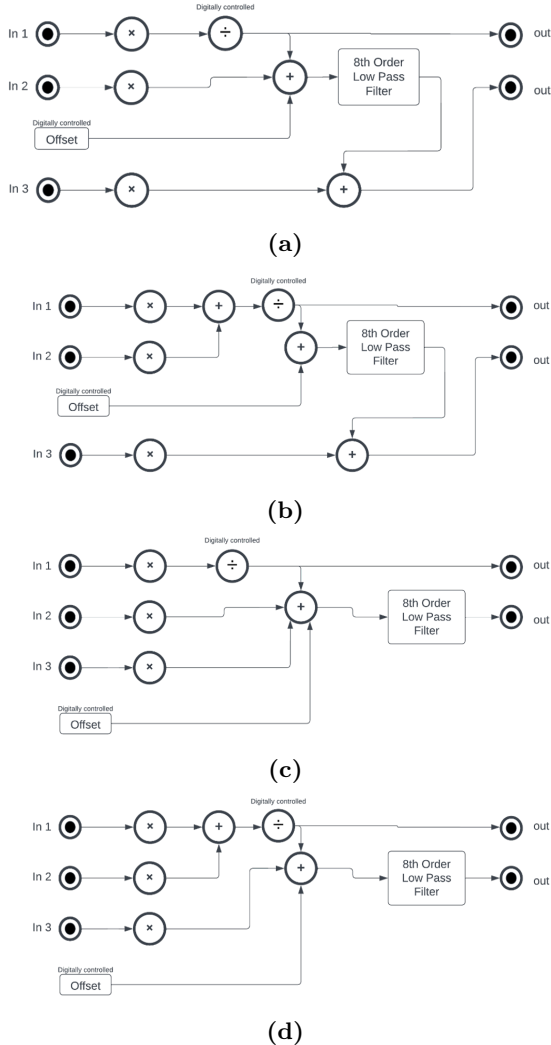


**Figure 2.12:** Simple schematic of the Z module for the a) first mode, b) second mode, c) third mode, d) fourth mode.

## 2.2. Electrochemical Scanning Tunneling Microscope

---

feedback. This solution can get rather challenging in the case of the need for changing the bias voltage during the scan time because all the parameters should be changed with a specific timing to avoid tip crashes or losing the tunneling current. The second solution is applying an absolute value operator on the input signal (output of the pre-amplifier). This avoids the aforementioned issue with the polarity and the feedback loop can work without any problems. It also reduces the complexity of changing the tunneling bias and having stable control over the tip location. Thus, the next required module is an absolute amplifier. A simple schematic is shown in Figure 2.13a. The output of this module can be internally connected to the input of the logarithmic amplifier and there are two external outputs. “Out 1” is directly connected to the absolute amplifier and “Out 2” is a buffered signal of the input and it can deliver up to 250 mA.

Since the tunneling current magnitude is an exponential function of the tip-sample distance, having a logarithmic amplifier is a must. As shown in Figure 2.13b, there are two inputs for this module, one is internal and comes from the absolute amplifier and the other one is for an external signal. The logarithmic amp can perform logarithm operations over 8 decades (very wide dynamic range). The output range in the standard configuration is  $\pm 10$  volts. “Out 1” is the connector for the external connection and the second output can be connected internally to the PID module.

Figure 2.13c shows the PID module with the integrated low-pass filter. This module has three inputs, one internal and two external connectors. The internal input can be disconnected and leaves room for the external inputs. The two external inputs can be used as the PID setpoint and input for the main feedback signal. There is also the possibility of adjusting the setpoint internally, which can be controlled digitally by the software. After the voltage adder, the error signal goes through the PID controller. The PID coefficients are controlled by the computer in 256 steps (LabVIEW or other language). The maximum values for each gain can be tuned by choosing the appropriate resistors and capacitors values. One active low pass filter with a tunable cutoff frequency is placed after the PID controller to limit the bandwidth and avoid oscillations caused by the white noise and slight tip crashes during the scan time. Just before the output connector, there is an inverter to invert the polarity of the PID. This can be bypassed due to the next module and its configuration.

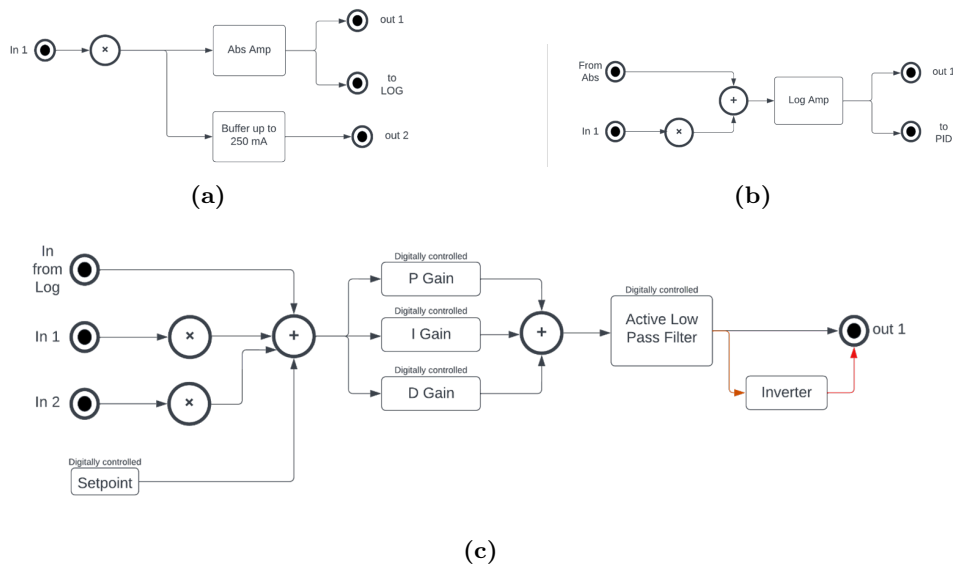


**Figure 2.13:** Simple schematic for the a) absolute amplifier, b) logarithmic amplifier, c) PID with a low-pass filter

#### 2.2.4 Mechanical design

There are many different mechanical designs for the SPM which were introduced thoroughly in the literature[15]. EC-STM has some specific challenges and these should be considered during the design steps. The main considerations are as follows:

- The sample should always be placed horizontally and the tip should land on the sample from the top since the surface should be in contact with the electrolyte.
- The electrolytes can be very corrosive and damaging to the mechanical parts. Protective properties are essential.
- The electrolyte should be in contact with as few parts as possible since the cleanliness of the entire electrochemical cell is crucial and those parts should be resistive against the electrolytes and do not contribute to the electrochemical reactions inside the cell.
- Easy and fast assembling steps for the experiments because the complexity of these steps can lead to introducing extra contamination to the sample surface and the electrochemical cell.

## 2.2. Electrochemical Scanning Tunneling Microscope

---

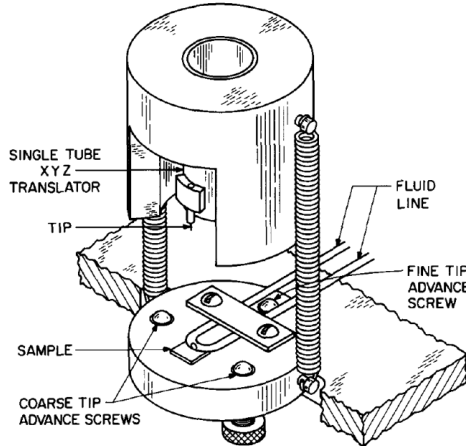


**Figure 2.14:** STM design which operates with a drop of fluid on the sample. The two springs hold the top piece, which has the scanner tube, and hold the tip in an upside-down configuration. Two coarse advance screws are deployed to be adjusted by hand for the initial approaching step and one fine screw is connected to the motor to adjust the height automatically during the auto approach step[17]. Reprinted with permission from Elsevier.

The best fit for these requirements is the single-tube scanning tunneling microscope design. In this design[17], the single tube scanner head is placed on the top of the sample and secured with springs. The tip is hanging on the single tube translator (scanner head) and it can land vertically on the sample. The sample and the entire electrochemical setup can be installed on the base plate. By removing the single tube transducer, the operator has enough room to assemble the sample and EC cell quickly. Three fine screws help the coarse approach steps and the fine approach step can be done by the accurate motors.

Figure 2.15a shows the designed base plate. This is the main plate that holds the EC cell, the sample, the scanner head, and fine screws/motors. This plate is connected to a vibration isolation system from three points which are shown with white signs with three metallic pillars. In the center, there is a large circular cut that accommodates the EC cell and sample. The three cyan-colored cylinders show the locations of the motors and the four arrows can be seen pointing downwards. These arrows show the direction of the forces applied to this plate. The center arrow is coming from the center of mass of the plate and the three outer are related to the forces on the three fine screws/motors holding the scanner head. The chosen material for this part is Invar to reduce thermal drifts in the XYZ direction. To ensure the rigidity of the

design, a finite element simulation can shed some light on the design characteristics. The result shows that the first fundamental resonance frequency is 7727.52 Hz which is high enough for many experiments.

The next part is the scanner holder that is shown in Figure 2.15b. Three seats are designed at the bottom (indicated with white signs) to land on the upward fine screws to hold the scanner head assembly (scanner holder + piezo tube). On the top part, the indicated cyan area is the plane that the piezo tube can be attached and the arrow shows the direction of the force on this part from the piezo tube. The desired material for this part is Invar as well. The first resonance frequency of this part is 7599.42 Hz, according to the simulation.

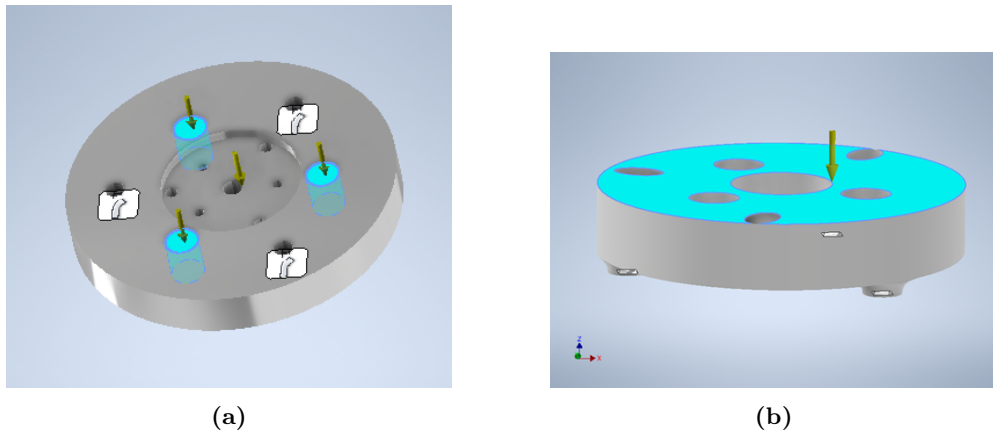


**Figure 2.15:** a) The base plate with the three white signs shows the location of the three main legs that hold the entire microscope. The three cyan-colored cylinders show the locations of the motors and the arrows indicate the directions of forces on this plate. The center arrow is the result of the mass of this plate and the three surrounding arrows show where the three fine screws/motors hold the mass of the scanner head. b) The scanner holder which has three seats for the fine screws indicated with white signs. The cyan surface shows the plane that the piezo tube can get connected to and the arrow shows the force direction caused by the mass of the piezo tube.

The electrochemical cell, which will be filled with an electrolyte during the experiments, is an important part of the setup. The design of this part needs more sophisticated computational fluid dynamic simulations to improve the properties of the cell. Appendix A is dedicated to the design for this part. The cross-section of the design in the Y-Z plane crossing the center of the sample is shown in Figure 2.16. The EC cell is in yellow and the insulator plate is in blue. The base plate is located at the bottom and the tip (in green) is hanging from the tip holder. The selected material for

## 2.2. Electrochemical Scanning Tunneling Microscope

---

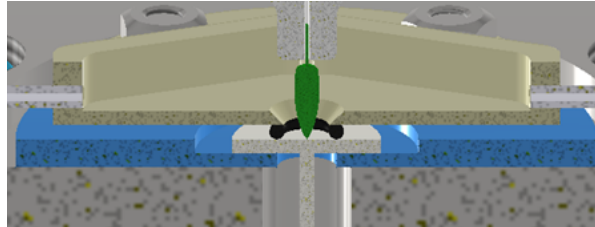


**Figure 2.16:** Cross section of the design in Y-Z plane. The EC cell is in yellow and the insulator plate is in blue. The base plate is located at the bottom and the tip (in green) is hanging from the tip holder. The O-ring in black is located above the sample and underneath the EC cell to avoid electrolyte leakage and the inlet and outlet are located on the left and right side of the EC cell.

the tip holder, the EC cell, and the insulator plate is PEEK since PEEK is a very good electrochemically resilient material for basic and acidic electrolytes and it is suitable for a large spectrum of electrochemical experiments. PEEK is also resilient against the conventional cleaning procedure of cleaning (soaking in potassium permanganate, then diluted piranha solution, and several times boiling in milli-Q water). The O-ring in black is located above the sample and underneath the EC cell to avoid electrolyte leakage and the inlet and outlet are located on the left and right side of the EC cell. The cell can be fixed to the base plate by three nuts and the tightness of the nuts will indicate the total force on the O-ring and the sample. Extra force can be damaging for soft samples like gold, so precautions should be taken.

The entire CAD design is depicted in Figure 2.17a, which shows the location of the three motors under the base plate in gray, the reference electrode secured on the base plate in yellow, and the scanner head assembly on the top. By having the designed parts manufactured, the assembling process was done and Figure 2.17b shows the final result. The three motors are located below the main plate and secured tightly to it. The whole scanner head assembly is located on the three motors and can lift and lower the head for a coarse approach and auto-approach mechanism. There are two thin pipes on both sides of the main plates which are connected to the EC cell. Pumping the electrolyte in and out is possible through these pipes. Since the scanner holder is detachable from the piezo tube, it is easy to have different piezo tubes for different experiments. The longer scanner head in Figure 2.17c provides a larger scan area. In this figure, all the electrical connections are shown and the inlet and outlet pipes are connected as well.

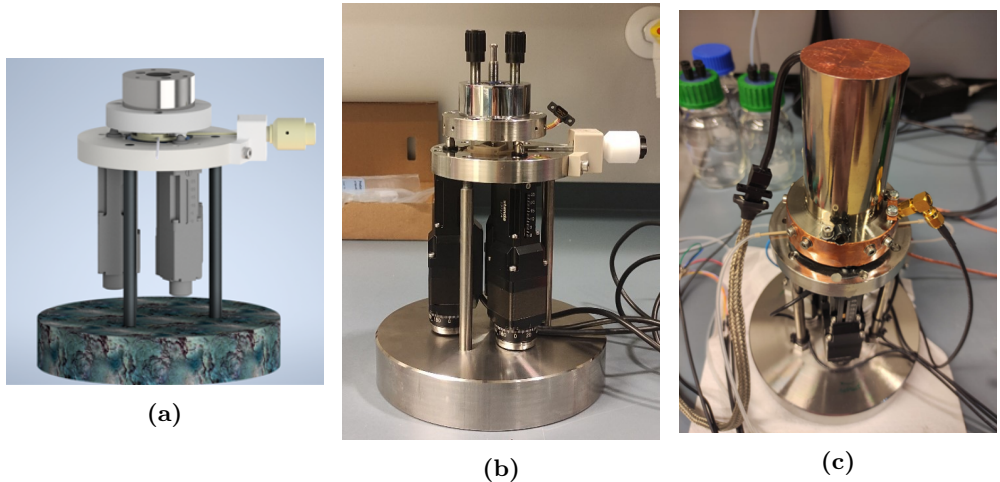


**Figure 2.17:** a) The CAD model of EC-STM design b) manufactured and assembled with a smaller piezo tube, c) with a piezo tube for larger scan areas.



# Chapter 3

3

## In situ STM Study of Roughening of Au(111) Single-Crystal Electrode in Sulfuric Acid Solution during Oxidation-Reduction Cycles

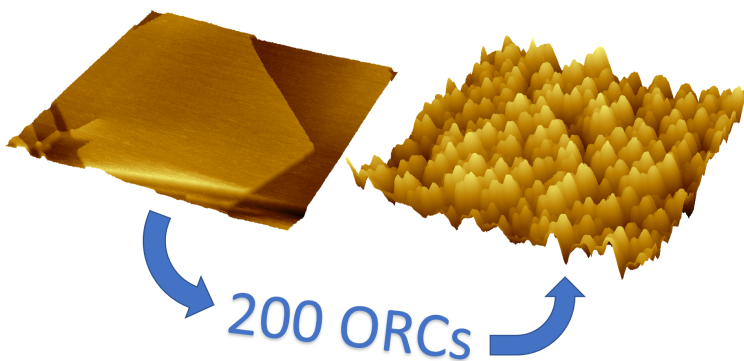


Figure 3.1

### **3.2. Abstract**

---

#### **3.1 Abstract**

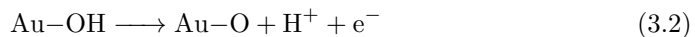
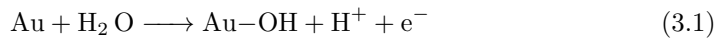
Oxidation-reduction cycles (ORCs) on Au(111) in 0.1 M sulfuric acid solution change the electrode morphology due to the formation of many new nano-sized islands. With increasing the cycle number, the roughness of the surface increases due to the formation of multi-atomic-step adatom islands and pits. The final roughness value is a function of the applied potential window, number of ORCs, scan rate, electrolyte concentration, and any applied delay time. In the first experiment, the roughening was tracked by recording the STM images in 11 steps during 200 ORCs. The results show the formation of pyramidal islands and a linear correlation between the roughness amplitude and the cycle number. In a second experiment, the 200 cycles were studied in 38 steps while after each step, two images were recorded with a 3-minute delay by holding the potential in the double-layer window. This leads to a lower roughness increase due to the high surface mobility of the Au surface atoms, which smoothens the surface during the delay time. Finally, the oxidation-reduction charge density per cycle shows an inverse correlation with surface roughness due to the (111) terrace showing a higher surface oxidation charge than the other sites and facets. Each delay causes a strong increase in the oxidation charge which is a consequence of surface smoothening during the delays leading to an enhancement of the (111) related oxidation charge.

#### **3.2 Introduction**

Gold is well-known as an important material for various applications, and therefore the structure and characteristics of single-crystal gold surfaces have been studied in ultra-high vacuum (UHV) [18, 19] and aqueous electrochemical environments[6, 20]. Electrochemical characterization of gold electrodes often involves cyclic voltammetry experiments in which the gold surface is oxidized and subsequently reduced. Oxidation of gold electrodes in acidic electrolytes containing sulfate or perchlorate anions has been studied thoroughly [20, 21, 8, 22]. For sufficiently positive potential, sulfate anions will be specifically absorbed on the surface and form an ordered sulfate adlayer, with the anions undergoing either partial or complete charge transfer[23]. On the other hand, perchlorate anions are considered to reside in the electrochemical double layer without chemisorption and adlayer formation. The onset potential for surface oxidation is influenced by this adlayer, as anion adsorption blocks the initial stages of OH electrosorption. At sufficiently positive potential, two reactions have been

### Chapter 3. In situ STM Study of Roughening of Au(111) Single-Crystal Electrode in Sulfuric Acid Solution during Oxidation-Reduction Cycles

suggested to initiate surface oxidation:



3

As shown in Reaction 3.1, the oxidation starts with electroabsorption of  $\text{OH}^-$ . Reaction 3.2 will take place at slightly more positive potential and has been suggested to lead to a two-atom thick oxide layer[8]. The formation of  $\text{Au}-\text{OH}$ ,  $\text{Au}-\text{O}$ , and  $\text{Au}_2\text{O}_3$  species on the surface has been considered based on charge and capacitance results acquired by conventional electrochemical techniques[21, 24, 25].

By applying successive oxidation-reduction cycles (ORC) on Au (111) single crystal electrodes in an acidic electrolyte, some long-range nano-patterned surfaces are formed which after many cycles will lead to a highly roughened surface. This procedure is used e.g. for preparing rough gold surfaces for Surface Enhanced Raman Spectroscopy[26]. In situ electrochemical scanning tunneling microscopy (EC-STM) is a suitable technique to record the surface evolution with atomic resolution from the pristine Au (111) surface to the final roughened or electrochemically annealed surface[27]. The pattern formation resulting from the applied oxidation-reduction cycles likely depends on many parameters; specifically: the lower and upper potential limits of the cycles, the potential scan rate, the number of cycles, and the electrolyte composition. It has been reported that after 10 ORCs in 0.1 M sulfuric acid, only vacancy islands form on Au(111), and this points out that some other mechanisms are taking place (i.e. gold dissolution) apart from the place exchange mechanism. By increasing the number of cycles, adatom islands start to appear[6]. In this paper, we perform a detailed study and analysis of the oxidation-reduction cycling experiment to have a better understanding of the roughening process. Specifically, we study how stopping the potential in the double layer window during the cycling strongly affects the gold surface dynamics, showing that the gold surface atoms are highly mobile even if surface oxidation and reduction do not take place. This has a corresponding effect on the roughening of the surface. Moreover, we show that the roughening stages are not well captured quantitatively by the oxide formation and reduction charges from the cyclic voltammetry.

### **3.3. Experimental**

---

## **3.3 Experimental**

### **3.3.1 EC-STM measurements**

The Electrochemical Scanning Tunneling Microscope (EC-STM) images were recorded with a home-built instrument, which was developed at the Leiden Institute of Chemistry (LIC) of Leiden University. Details of the design and construction of this instrument are given in the Supporting Information. The tips were produced from a platinum/iridium wire (90/10) by the pulling-cutting method. To reduce the extra faradaic current on the tip, a layer of hot melt adhesive (EVA-copolymer, synthetic resin, Wax and Stabilizer Brand: C.K.) was added except for the apex of the tip. A disk-shaped single-crystal electrode Au(111) (10 mm diameter) with a gold wire welded at the back was used as the working electrode (WE). The crystal was cut with an accuracy of 0.1° and polished down to 30 nm roughness (Surface Preparation Laboratory, Netherlands). Before each measurement, the Au(111) sample was annealed by a butane flame torch to an orange color for 5 minutes and cooled down in air above the surface of ultrapure water to avoid introducing contamination to the sample surface. A high-purity gold wire was used as the counter electrode (CE) and a reversible hydrogen electrode (RHE, Hydroflex, Gaskatel) was used as a reference electrode (RE). The distance between the working electrode and the reference electrode is about 7 mm to minimize the ohmic drop during the voltage sweep. The images were recorded in constant tunneling current mode with the tunneling bias between 10 to 20 mV and the current setpoint was between 100 to 150 pA. The current setpoint was changed to zero to maximize the distance between the tip and the sample while applying the cyclic voltammetry (CV). Then the electrochemical voltage was set to the “rest potential”. In this condition, by increasing the current setpoint, the tip could approach, and the tunneling current on the tip appeared. During the experiment, the EC-STM chamber was purged with ultra-high-purity argon gas to reduce the chance of oxygen (or other gasses) dissolving into the EC-STM cell.

### **3.3.2 Electrochemical Cell and Electrolyte**

A custom-made Pyrex glass cell was used for standard electrochemical experiments. The glassware and plastic parts were cleaned by leaving them in a permanganate solution (0.5 M sulfuric acid and 1 g/L potassium permanganate) for at least 12 hours prior to each experiment. After rinsing them with milli-Q water, diluted piranha solution (3:1 mixture of sulfuric acid ( $H_2SO_4$ ) and hydrogen peroxide ( $H_2O_2$ ), diluted

## 3.4 Results and discussion

### 3.4.1 Oxidation-reduction cycles of Au(111) without holding potential in double layer

To check the quality of the sample surface, Figure 3.2a shows the CV of the Au(111) electrode in 0.1 M sulfuric acid that was recorded with a scan rate of  $s=50\text{ mV/s}$  in the potential window of 0.05 to 1.1 V. At potentials below 0.5 V, there is a low current corresponding to the double layer charging of the  $(\sqrt{3} \times 22)$  reconstructed surface, which was formed during the annealing step. At higher potential (ca. 0.55 V), sulfate adsorbs and induces the lifting of the reconstruction, corresponding to the anodic peak at 0.64 V [22, 28]. The broad peak which appears at 0.78 V is due to further absorption of anions and lifting the rest of the reconstruction[29]. The subsequent sharp anodic peak at 1.10 V is caused by the formation of an absorbed anion overlayer with  $(\sqrt{3} \times \sqrt{7})\text{ R}19.1^\circ$  structure [22]. In the reverse scan, the peaks at 1.07 V, 0.68 V, and 0.53 V correspond to the reverse processes, with the re-formation of the reconstructed surface at the lowest potentials. By increasing the upper potential of the voltage window, the CV in Figure 3.2b was recorded. There is now one distinct anodic peak at 1.62 V, corresponding to surface oxide formation and anion desorption. With the presence of defects on the surface, a small and broad peak at 1.44 V appears and its absence would indicate the quality of the sample used in the experiment.[6] Finally, the large cathodic peak at 1.16 V in the return scan shows the reduction of the formed oxide and the reabsorption of anions. The shoulder peak observed at potentials negative of the main cathodic peak has been discussed as resulting from the formation of two different oxides [30].

Next, a series of experiments was conducted to investigate the roughening process occurring during oxidation-reduction cycles. The same sulfuric acid electrolyte was used in the EC-STM experiments. Duplicate experiments were performed to confirm the reproducibility of the experimental observations.

### 3.4. Results and discussion

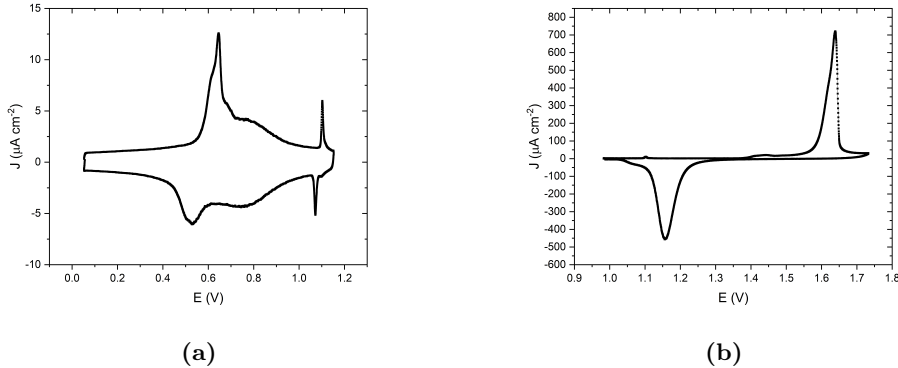


**Figure 3.2:** Cyclic voltammetry for Au(111) electrode in 0.1 M sulfuric acid with a scan rate of  $50 \text{ mVs}^{-1}$  at a temperature of  $T = 298 \text{ K}$  A) from 0 to 1.15 V versus RHE. B) from 0.98 to 1.7 V versus RHE.

Figure 3.3a shows an EC-STM image of the pristine surface of the sample in 0.1 M sulfuric acid at an electrode potential of 0.05 V. There are some defects in the left-bottom and right-bottom parts of the image which are useful to aid in the compensation for the thermal drifts in long-term experiments. There are still large flat terraces in the middle and top parts of the image, which is a good situation for studying the roughening of the Au(111) surface. Figure 3.3b shows the Au(111) surface after the potential has been swept from 0.05 to 0.88 V. As the potential is higher than the potential of zero charge, the reconstruction of the Au(111) surface has been lifted. The lifting of the reconstruction causes ca. 4% of excess atoms in the first atomic layer to be expelled, resulting in the formation of numerous small islands. The formed islands are monoatomic (ca.  $2.3 \text{ \AA}$ ). Figure 3.3c was recorded at the same potential of 0.88 V after a four-minute delay, to show the influence of time for comparison with Figure 3.3b. The number of islands has evidently diminished, while simultaneously observing an increase in their size, suggesting the ripening of the islands. The rapid growth of the islands shows that gold atoms are rather mobile and can detach from the steps and hoover on the terraces. They finally find each other, or other islands, and form larger islands. Additionally, a large vacancy island (parallelogram shape) has appeared on the initially flat terrace. The reason for the appearance of this large vacancy island is unknown, but it could be caused by some crystal defects in bulk.

Figure 3.4a shows the sample surface after 5 consecutive oxidation-reduction cycles from 0.98 to 1.73 V with a scan rate of  $50 \text{ mV s}^{-1}$  with the image recorded at 0.98 V. The formation of numerous islands with varying heights of one or even two atomic steps

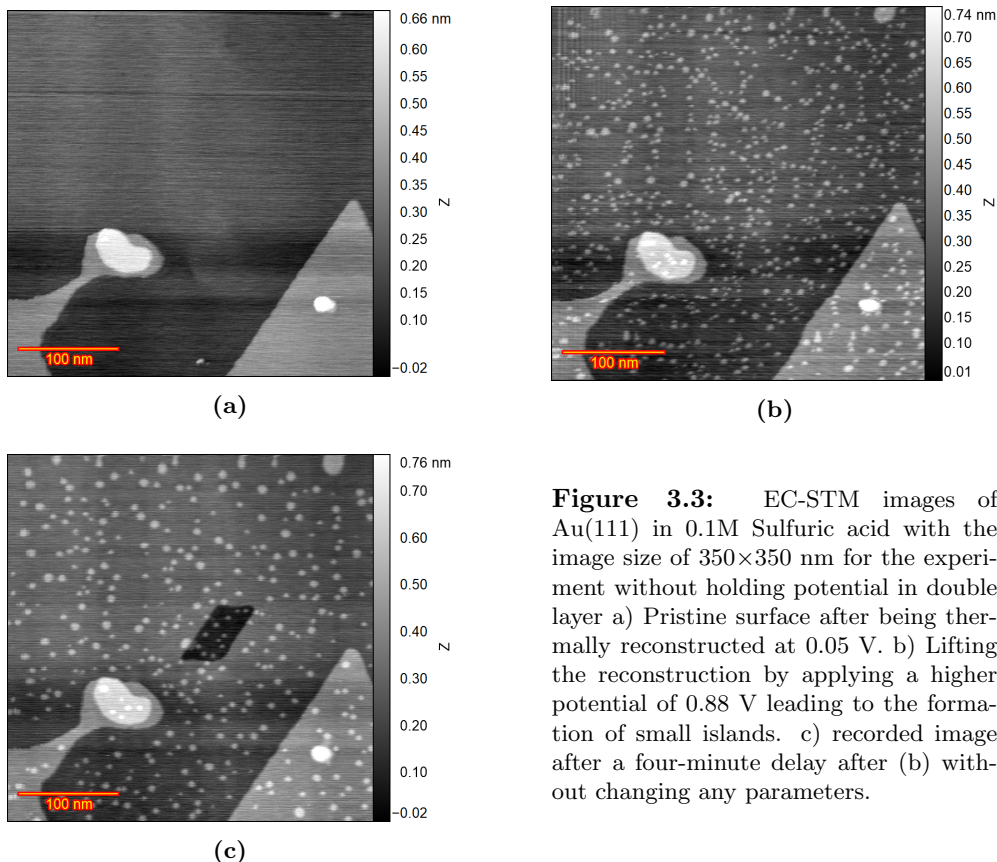


**Figure 3.3:** EC-STM images of Au(111) in 0.1M Sulfuric acid with the image size of  $350 \times 350$  nm for the experiment without holding potential in double layer a) Pristine surface after being thermally reconstructed at 0.05 V. b) Lifting the reconstruction by applying a higher potential of 0.88 V leading to the formation of small islands. c) recorded image after a four-minute delay after (b) without changing any parameters.

### 3.4. Results and discussion

---

is evident throughout the surface in Figure 3.4a. Additionally, the presence of vacancy islands between these islands can be observed. After five additional consecutive cycles (i.e. total number of cycles reaching 10), the image in Figure 3.4b was recorded. Comparing the images after 5 and 10 ORCs, a distinct and noteworthy trend emerges: the number of islands with two atomic steps in height has visibly increased, while the presence of monoatomic islands appears to be scarce after 10 cycles. The roughening process has progressed to the extent that one can barely distinguish the original surface at this stage, though interestingly enough, the parallelogram can still be distinguished. Figure 3.4c shows the STM image after 50 cycles when the islands have grown in size while having diminished in number. The island shape is approximately triangular and their direction is not randomly distributed. After 150 ORCs, Figure 3.4d is recorded and shows that features like the step lines of the initial surface are not distinguishable anymore, and the entire surface is covered by larger pyramids oriented to the three crystallographic axes (particularly [110], [101], and [011] directions). Moreover, their height is increasing indicating an increase in surface roughness. The surface after 200 ORCs is shown in Figure 3.4e. At higher ORC numbers, it is evident that the height of the pyramids is increasing (considering the gray-scale bar range). For a more quantitative comparison, it is necessary to calculate the average size and height of the islands for each stage. An appropriate approach for this is to calculate the height-height correlation function.

#### Calculation of the height-height correlation

Determining the height-height correlation function (HHCF) serves as a robust analytical tool for characterizing the spatial properties and scaling behavior of surface roughness. Height-height correlation relies on the principle that the heights of neighboring points on the surface are not independent but correlated. This method quantifies the level of correlation or similarity between the heights of distinct points in relation to their separation distance. The formula for the calculation of the HHCF is:

$$H(r) = \langle [h(\vec{x}) - h(\vec{x} - \vec{r})]^2 \rangle \quad (3.3)$$

$$H(r) = \begin{cases} \propto r^{2\alpha}, & \text{if } r \ll \xi \\ 2\sigma^2, & \text{if } r \gg \xi \end{cases} \quad (3.4)$$

where  $h(\vec{x})$  is the surface height at the given position  $\vec{x}$  and  $h(\vec{x} - \vec{r})$  is the height for

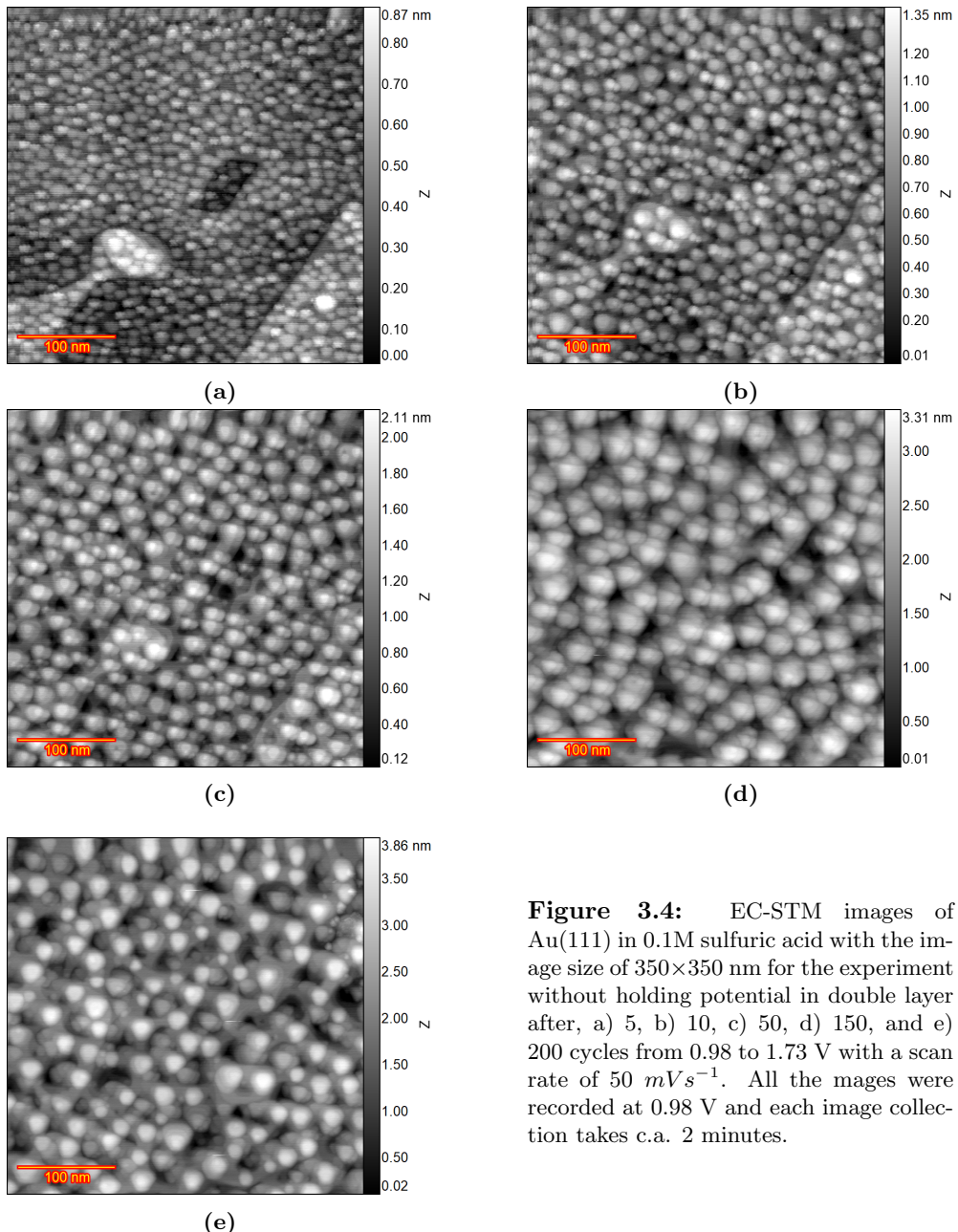


**Figure 3.4:** EC-STM images of Au(111) in 0.1M sulfuric acid with the image size of  $350 \times 350$  nm for the experiment without holding potential in double layer after, a) 5, b) 10, c) 50, d) 150, and e) 200 cycles from 0.98 to 1.73 V with a scan rate of  $50 \text{ mVs}^{-1}$ . All the mages were recorded at 0.98 V and each image collection takes c.a. 2 minutes.

### 3.4. Results and discussion

---

a position at a distance of  $\vec{r}$  from position  $\vec{x}$ . For a self-affine surface, the HHCF has the form of Eq.3.4 [31]. From this equation, the root mean square (RMS) roughness amplitude ( $\sigma$ ), the lateral correlation length ( $\xi$ ), and the roughness exponent ( $\alpha$ ) can be derived through the analysis of the HHCF[32]. The size of the analyzed images must be at least 10 times greater than the lateral correlation length ( $\xi$ ) to ensure statistical relevance in the HHCF calculations. In order to facilitate a meaningful comparison among all frames, a linear regression was employed on the images to mitigate sample tilt effects (the tip is not perfectly perpendicular to the sample surface). This prevents the sample tilt from introducing extraneous roughness into our analysis. The height-height correction function thus calculated is depicted in Figure 3.5a. For large  $\vec{r}$ , a plateau emerges, providing the basis for calculating the root mean square (RMS) roughness amplitude ( $\sigma$ ) (see Eq.3.4). With an increase in the number of oxidation-reduction cycles (ORCs), the roughness increases, in agreement with the topographical images. For smaller  $\vec{r}$ , a distinct slope is observed, from which the roughness exponent ( $\alpha$ ) can be calculated. The distance at which the transition occurs from the slope to the plateau can be regarded as the lateral correlation length, ( $\xi$ ). First of all, at a low number of ORCs, it is observed that  $h(\vec{x})$  shows (at least) two slopes. In the case of the first frame (representing the pristine surface), we expect the lateral correlation length to be very large (ideally infinite). However, in practice, there are steps, defects, and electrical and mechanical noises in the image. Therefore, the pristine sample surface shows a correlation length of ca. 100 nm. Once the reconstruction is lifted, we expect to have some islands with specific diameters on these terraces. There is an intermediate range of ORCs in which the transition from the sloped line to the plateau takes place in two steps. This is a result of having two scaling regimes[33]. There is a steeper part at small  $\vec{r}$  which is due to the roughening caused by the ORCs (microtexture), followed by an intermediate region with a different slope that is related to the steps and the defects in the frame (macrotexture). Under these conditions, we assign the correlation length of the new monoatomic islands as the transition point from the steeper line to the less steep line. The second transition point matches the correlation length of ca. 100 nm of the pristine surface. To avoid having two scaling regimes, one could ideally avoid having any steps or defects in the analyzed area. After more ORCs, the surface becomes more roughened and consequently, the roughness of the initial steps and defects of the surface becomes insignificant. Figure 3.5b depicts the roughness amplitude (in black) and correlation length (in red) versus the cycle number. The roughness amplitude ( $\sigma$ ) increases linearly with the cycle number (except the 200<sup>th</sup> cycle). For the correlation length ( $\xi$ ), one can divide the curve into two regimes with

### Chapter 3. In situ STM Study of Roughening of Au(111) Single-Crystal Electrode in Sulfuric Acid Solution during Oxidation-Reduction Cycles

different slopes. This shows that in the initial stage of roughening, the islands grow faster laterally (corresponding to the correlation length) and as soon as they reach the size of ca.15 nm, their lateral size changes more slowly and they tend to grow mainly in height.

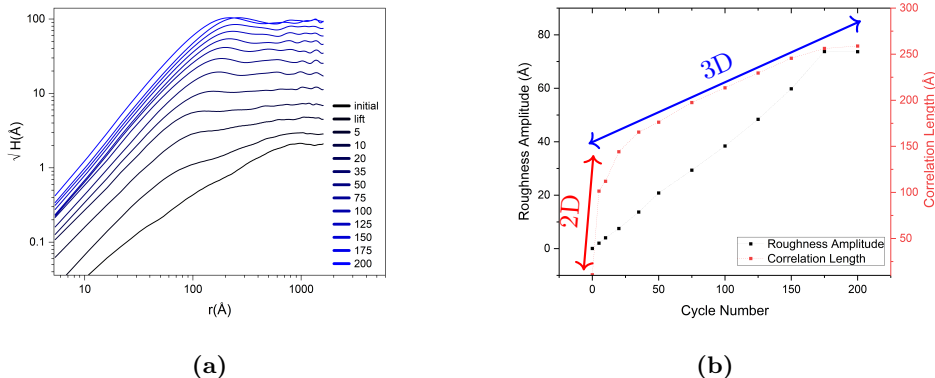


**Figure 3.5:** a) Height-height correlation function versus distance  $r$  for Au(111) in 0.1 M sulfuric acid as a function of the number of oxidation-reduction cycles (ORCs) for the experiment without holding potential in the double layer. b) Extracted roughness amplitude and correlation length versus cycle number from the HHCF results. The arrows indicate the 2D and 3D island growth regimes.

#### 3.4.2 Oxidation-reduction cycles of Au(111) with holding the potential in double layer

In the next experiment, we aimed to investigate the effect of a waiting time in the double layer region on the roughening induced by ORCs of the Au(111) single crystal in 0.1 M sulfuric acid. The goal of this experiment is to study the effect of gold atom surface dynamics in the double-layer window on a roughening surface. Before this particular experiment, we also studied the potential-induced lifting of the reconstruction in more potential steps. This is described in the Supporting Information. Figure B.1 shows the strip reconstruction (which forms at higher strain values[34]), early adatom island formation, step line evolving, formation of monoatomic islands after lifting, and island ripening.

The experiment including delay was as follows. The electrochemical potential was kept at 0.98 V as the lowest vertex potential for the entire experiment. Next, a certain number of oxidation-reduction cycles from 0.98 to 1.73 (V) with a scan rate of 50 mV/s

### 3.4. Results and discussion

---

were performed with the tip retracted. Immediately after the number of OR cycles, the tip was approached and an image was recorded. We call this "instant frame". Image recording takes about 2 minutes, after which a one-minute waiting time at 0.98 V was applied. Then, another image was recorded which is named "delayed frame". Therefore, the total time difference for each corresponding scan line in the instant and delayed frames is three minutes. During the waiting time, no parameter was changed to rule out any other sources for disturbance/change of the system with the tip standing in the top-left part of the scan area, in tunneling mode. Figure 3.6a shows the instant frame after the first ORC. Many small adatom islands and some vacancy islands were formed. The delayed frame is depicted in Figure 3.6b, which shows the presence of larger islands. The extra atoms for the formation of larger islands come from smaller islands as the result of either Ostwald ripening or Smoluchowski ripening. After the 10<sup>th</sup> ORCs, the instant frame and the delayed frame in Figures 3.6c and 3.6d were recorded. The total number of the adatom islands increased and many small vacancy islands emerged. Moreover, some bilayer adatom islands are formed. This is the starting point of the 3D island growth, but the delay is postponing that. The delayed frame shows that the islands have increased in lateral size at the expense of smaller islands. Additionally, many small islands in the second layer have also vanished. It seems the decay rate of the top layer islands depends on the size of the bottom layer island underneath. It is known that for multi-layer islands on Cu(111), the Ehrlich-Schwoebel barrier remains constant for a terrace width higher than a critical width, but vanishes for the terrace widths lower than that[35, 36]. Similar behavior has been observed on Ag(111)[37]. This can explain why having a bilayer adatom island with a small size is not common and many bilayer adatom islands have larger sizes on the first layer. Moreover, the islands tend to show a triangular shape at this potential with more delay time, they form larger islands that show the equilibrium shape more evidently(see Figure 3.6d).

Figure 3.6e shows the surface after 50 ORCs. Apart from the formation of new adatom islands, some large vacancy islands formed mainly at the spots where we observed the formation of early adatom islands during the lifting of the reconstruction (see in SI Figure B.1). Also, a long step line was formed, initiated from the dislocation in the left bottom corner. Figure 3.6f shows the delayed frame which has fewer small islands. At this stage, multi-layer adatom islands are formed. Evidently, the surface becomes rougher by applying more cycles, i.e. after 150 ORCs (Figure 3.6g), with a delay time always leading to smoothening of the surface (Figure 3.6h). Even at high cycle numbers, there is a difference between the delayed frame and the instant frame

### Chapter 3. In situ STM Study of Roughening of Au(111) Single-Crystal Electrode in Sulfuric Acid Solution during Oxidation-Reduction Cycles

especially where the smaller islands are located, but the changes are more conspicuous at lower cycle numbers.

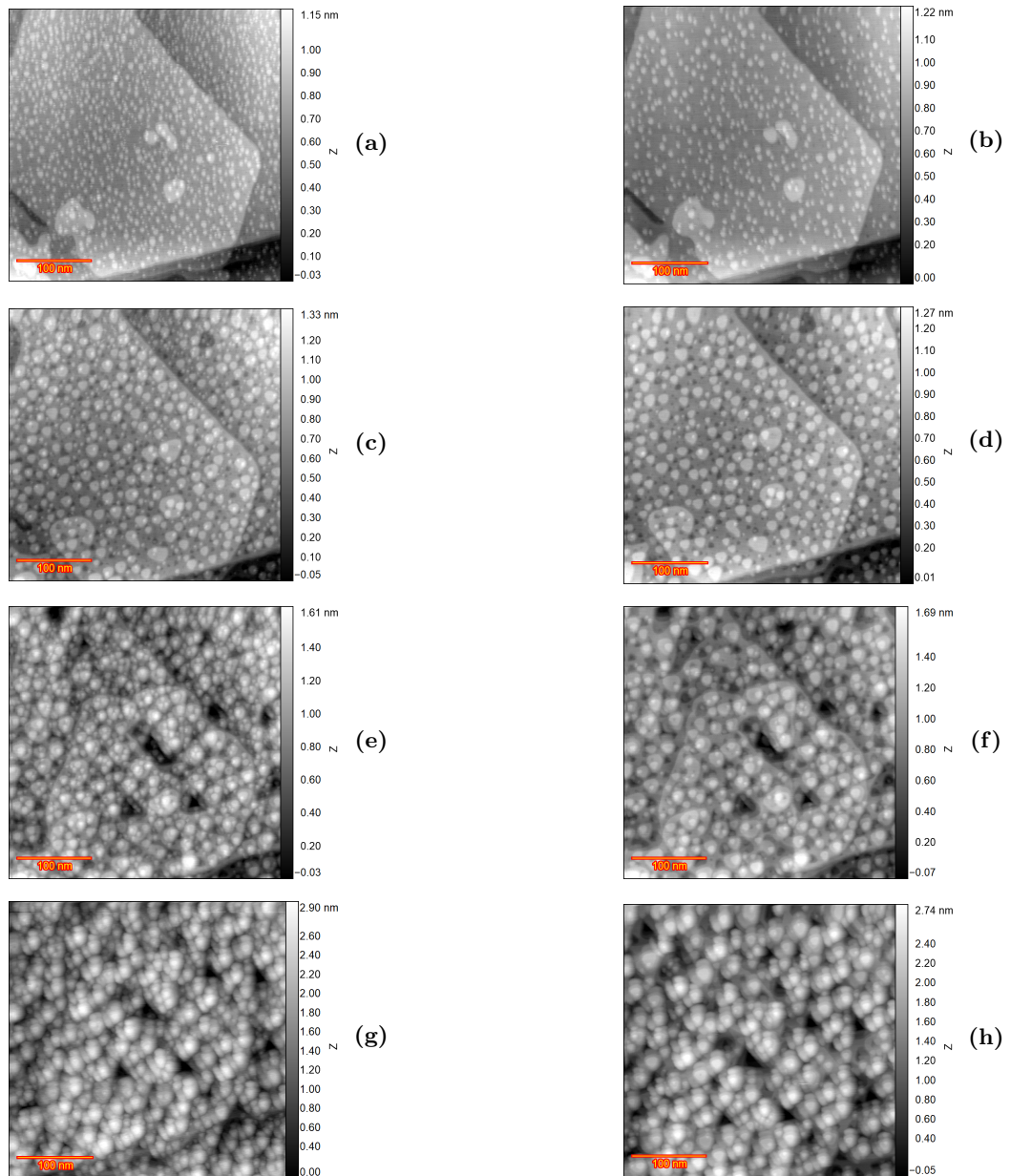
To have a more quantitative study of this delay effect, detection of the islands and subsequent calculation of their equivalent radius has been performed with Gwyddion software[38]. Figure 3.7a shows the results of the detected islands (in red) for the fourth ORC instant frame and 3.7b shows the same results for the delayed frame. From these images, the surface area of the islands was calculated and the equivalent radius of the islands was extracted. Figure 3.7c depicts the number of islands for the instant frame in red and the delayed frame in black versus their equivalent radius. The bars represent the number of the islands for the corresponding equivalent radius and the solid lines are drawn to facilitate the comparison. From this comparison, it is evident that the delay is specifically reducing the small islands with a radius of less than 2.5 nm, whereas larger islands seem less affected.

#### Calculation of the height-height correlation

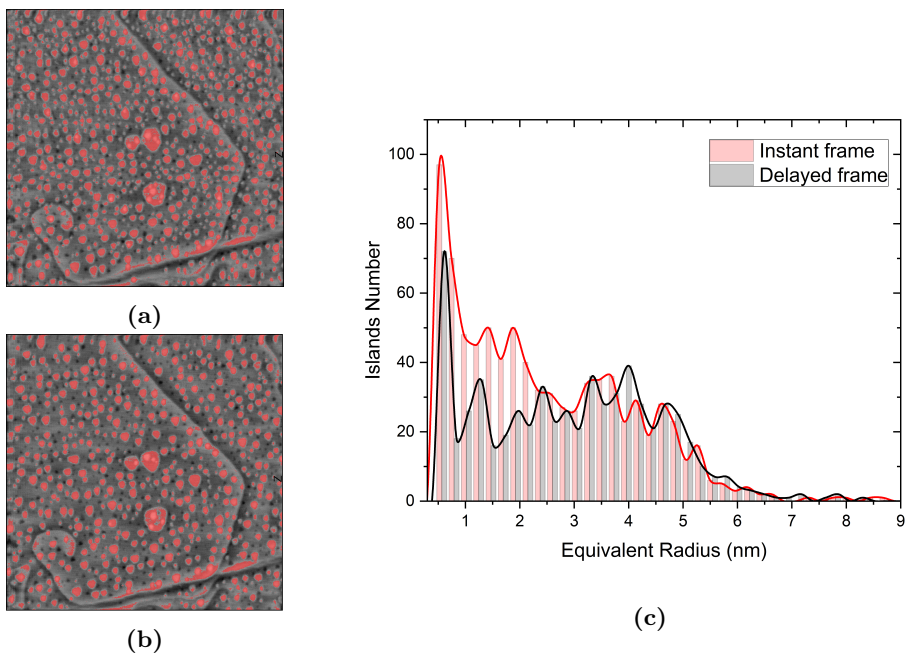
Figure 3.8a shows the HHCF for the delayed frames and the color gradient goes from black for the first cycle to blue for the 200<sup>th</sup> cycle. Figure 3.8b is the extracted correlation length and roughness amplitude versus cycle number from the HHCF results. The correlation length more clearly indicates the transition between 2D and 3D growth regimes at higher values. The roughness amplitude is increasing linearly with cycle number but the slope is slightly different from the 100<sup>th</sup> cycle onward because only four delays are applied between 100<sup>th</sup> cycle and 200<sup>th</sup> cycle. This change in the slope can be explained easily by comparison of the experiment with and without holding the potential.

Figure 3.9 compares the roughness amplitude and the correlation length versus cycle numbers for the delayed frames of the experiment with holding the potential shown in Figure 3.8b and for the experiment without holding the potential shown in Figure 3.5b. The comparison shows clearly the influence of the delay on the development of the roughness amplitude and the correlation length during ORCs. The experiment with additional delay shows a lower slope for roughness amplitude versus cycle number (the black line with triangular data points) and reaches a larger correlation length (ca. 20 nm) at a lower cycle number (the red line with triangular data points). By considering the fact that even for the experiment without holding the potential, there were some inevitable delays because of image recording, it is clear that the eventual roughening of the gold surface is very sensitive to scan rate and the existence of any delay times in the experiments (for instance by recording an image).

### 3.4. Results and discussion



**Figure 3.6:** Au(111) in 0.1 M sulfuric acid with the image size of  $350 \times 350$  nm with holding potential in double layer after a)  $N=1$  instant, b)  $N=1$  delayed, c)  $N=10$  instant, d)  $N=10$  delayed, e)  $N=50$  instant, f)  $N=50$  delayed, g)  $N=150$  instant, h)  $N=150$  delayed, where  $N$  is number of ORCs.



**Figure 3.7:** Adatom island detection for the frames after four ORCs with holding potential in double layer a) Instant frame which shows more small islands. b) delayed frame. c) islands number versus equivalent radius for the instant frame and delayed frame after four cycles. Solid lines connect the endpoints of the bars for easier comparison.

### 3.4.3 Comparison of STM-derived roughening to Oxidation-Reduction Charge Density

In electrochemical experiments with gold electrodes, the electrochemically active surface area is often estimated by calculating the gold oxide reduction charge[39]. Therefore, an experiment in a conventional electrochemical cell was conducted on an Au(111) electrode in sulfuric acid. The scan rate was set to  $50 \text{ mV s}^{-1}$  and the applied potential windows was from 0.98 to 1.73 (V) versus RHE. The current density was calculated by using the geometrical area of the working electrode. Figure 3.10a shows the CVs measured during the ORCs, with the first cycle shown in blue and the last cycle in red. The first cycles contain a sharp oxidation peak at 1.62 V in agreement with Figure 3.2b. With increasing cycle number, the sharpness of the main peak decreases and two oxidation peaks at lower potential appear. On the other hand, the shape of the reduction peak remains similar but the decrement of the current density of the peaks is

### 3.4. Results and discussion

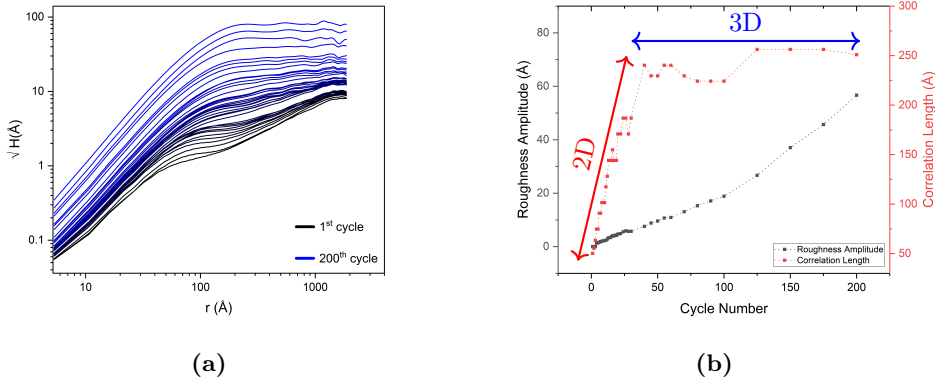


**Figure 3.8:** a) Height-height correlation function versus distance  $r$  for Au(111) in 0.1 M sulfuric acid as a function of the number of oxidation-reduction cycles (ORCs) for the experiment with holding potential in the double layer for the delayed frames. b) Extracted roughness amplitude and correlation length versus cycle number from the HHCF results. The arrows indicate the 2D and 3D island growth regimes.

obvious. Figure 3.10b shows the oxidation and reduction charge densities ( $\mu\text{C cm}^{-2}$ ) as a function of cycle number, obtained by integration of current of the recorded CVs subtracted by the double layer charging current (determined by the current density magnitude at 1 V where neither oxidation nor reduction is taking place). The dots represent the calculated data points and the lines are the result of a logarithmic fitting. The oxidation charge density is in black and the reduction charge is in red. Interestingly, the first cycle shows the highest oxidation and reduction charge density; subsequent ORCs lead to an approximate logarithmic decay with cycle number (fitting results in Table B.1).

The same analysis was done on the recorded CVs for the EC-STM experiment without holding the potential in the double layer (the same analysis for the experiment with holding the potential is achievable in the SI). The results in Figure 3.11a show the CVs, and 3.11b the calculated oxidation reduction charge density versus cycles number. The oxidation charge is maximum in the first cycle and it reduces gradually. However, a spike in both oxidation and reduction charge density appears just after the STM recording (when the potential is held in the double layer window) which did not appear in the results of the consecutive cycles shown in Figure 3.10b. The delay is caused by the required time for image recording after the fifth ORC while a constant voltage was applied. Then, the charge decreases again until the eleventh cycle after which a new STM image is recorded. Thus, each spike happens in the first cycle after

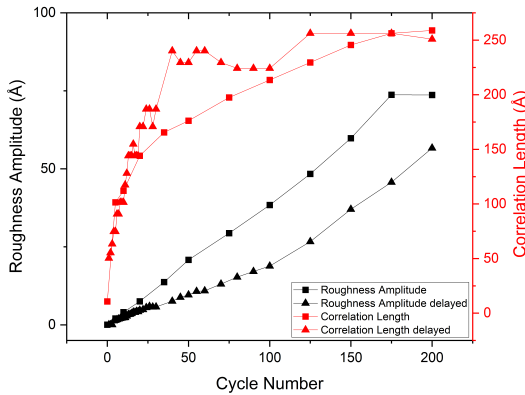


**Figure 3.9:** Roughness amplitude and correlation length versus cycle number for the experiment without holding potential in double layer (lines with square data points) and the delayed frames of the experiment with holding potential in double layer (lines with triangular data points).

each image recording. Moreover, the magnitude of the spikes decreases with higher cycle numbers. Regardless of the spikes, the overall charge density decreases with increasing number of cycles as in Figure 3.10b.

It is well-known that extensive electrochemical roughening of the gold surface leads to an increase in oxidation-reduction charge density[39]. This can be explained by the increase in actual active surface area due to extensive roughening. Considering the calculated roughness value from the two experiments and the oxidation-reduction charge density over cycles, our results reveal an inverse correlation, at least in the roughness regime relevant to our work. This indicates that the atoms on (111) terraces have a higher oxidation charge compared to the defects (different step types around the adatom islands and vacancy islands). Oxidation and reduction charge densities of Au(111) with different terrace widths have been reported in 0.1 M sulfuric acid for the first cycle after annealing [40]. The reported values for both anodic and cathodic charges showing a decrease for lower terrace width, confirm the difference for oxidation and reduction charges for different sites. This is consistent with the sharp increase observed in the oxidation charge density immediately following the delays, as we noted that the delays reduced the number of smaller islands in the STM images. This increases the proportion of atoms on the (111) terrace relative to the atoms at the defects, and hence the corresponding oxidation/reduction charges. The comparison of our STM images for both experiments with Kolb's results[6] reveals a difference in the

### 3.4. Results and discussion

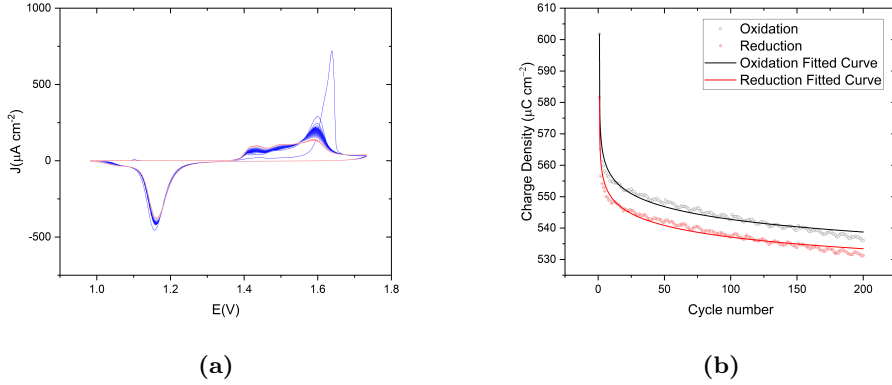


**Figure 3.10:** a) Cyclic voltammograms of the consecutively applied 200 ORCs on Au(111) in 0.1M sulfuric acid with a scan rate of  $50 \text{ mVs}^{-1}$  versus RHE. The color gradient from blue to red corresponds to the progression from the first to the last cycle. b) The circles show calculated oxidation(black) and reduction(red) charge density ( $\mu\text{C cm}^{-2}$ ) versus the cycle number for the CVs shown in (a). Solid lines represent logarithmic curve fitting for oxidation(black) and reduction(red) charge density.

results at lower ORC numbers. E.g. after ten cycles, no adatom islands were reported in their experiments and the entire scanning area was covered by pits, which indicates a higher dissolution rate of gold atoms for the low cycle numbers compared to our experiment. Our results show many monoatomic islands (more with more delays) and bilayer islands with some pits between them at the same cycle number. Furthermore, our experiment with delays shows that the duration of the experiment, such as scan rate or image capture time, has a substantial impact on the observed roughening, due to the high surface diffusion rate of the gold atoms, even in the double-layer window. Apart from this difference, the final results after many ORCs match qualitatively in terms of the shape of the islands and the long-range surface roughening.

The formation of nanoislands during ORCs is very similar to what has been observed for a Pt(111) surface[41], a kinetic model for which was proposed[42]. The primary difference is the much higher surface mobility of Au surface adatoms compared to Pt adatoms, including their ability to move over the step sites. Unlike the discussed inverse correlation between oxidation charge and surface roughness for Au(111), the study of the correlation between surface roughness and electrochemical data (hydrogen desorption charge) on Pt(111) showed that after the 31<sup>st</sup> cycle, every newly formed step site influences both the electrochemical signal and the surface roughness[41]. In other words, there is an approximately linear correlation between the surface roughness

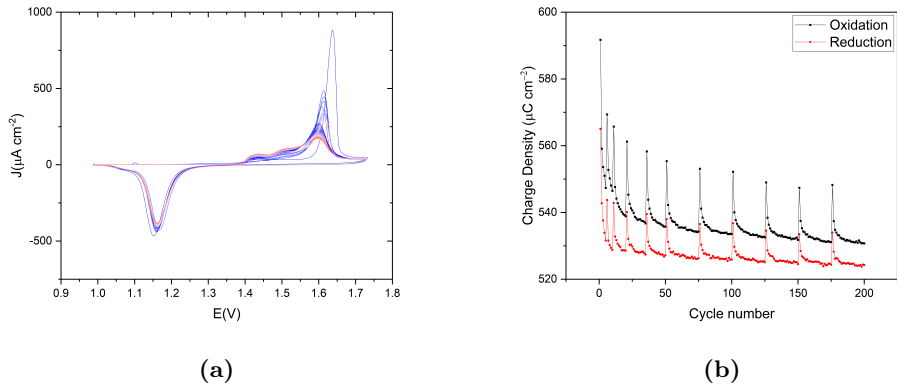


**Figure 3.11:** a) Cyclic voltammogram of the applied 200 ORCs on Au(111) in 0.1 M sulfuric acid with a scan rate of  $50 \text{ mVs}^{-1}$  versus RHE for the experiment without holding potential in double layer. The color gradient from blue to red corresponds to the progression from the first to the last cycle. b) Calculated oxidation-reduction charge density ( $\mu\text{C cm}^{-2}$ ) versus the cycle number for the CVs shown in (a).

and the hydrogen desorption charge after a certain cycle number. Such a correlation does (unfortunately) not exist for Au(111) roughening.

### 3.5 Conclusions

In this paper, we performed an in-situ EC-STM and electrochemical study of the roughening of an Au(111) electrode in sulfuric acid. Although such (nano-)roughening of Au(111) has been studied before [6], the atomistic mechanisms and the relation to the observed electrochemical signals have not been elucidated in detail. Specifically, we studied the effect of a delay time by holding the potential in the double layer region, on the roughness development of the surface by calculating the height-height correlation function and compared this with the surface area determination from the oxide formation and reduction charge densities in the CVs. The results suggest that the roughening starts with 2D island formation and is followed by 3D island growth. The extra delays can cause the formation of larger 2D islands (higher correlation length) and a lower roughness amplitude (lower roughening rate per cycle) for both 2D and 3D regimes. By calculating the size of the island, we showed that the number of islands with smaller sizes decreased after the delay, confirming the time effect in Au(111) smoothening caused by the high mobility of gold atoms in the double layer. The oxidation-reduction charge per cycle showed an inverse correlation between the

### **3.7. Acknowledgement**

---

oxide charges and the surface roughness suggesting that the charges at this roughness level are not a good indicator for the actual surface roughness. The results suggest that the oxidation charge per Au site is higher on the (111) terrace compared to other sites. Hence by losing Au(111), the surface charge decreases. The appearance of spikes in oxidation charge after image recording or delays is therefore consistent with a surface smoothening during the potential holding in the double layer.

## **3.6 Acknowledgement**

This work was funded by TOP grant project number 716.017.001, financed by the Dutch Research Council (NWO).

## **3.7 Supporting Information**

The extra experimental information is available in Appendix B.

# Chapter 4

## Effect of Trace Amounts of Chloride on Roughening of Au(111) Single-Crystal Electrode Surface in Sulfuric Acid Solution during Oxidation-Reduction Cycles

4

### 4.1 Abstract

This study investigates the impact of varying trace-level chloride ion concentrations on the roughening of a Au(111) electrode during oxidation-reduction cycles (ORCs) in 0.1 M sulfuric acid by *in situ* scanning tunneling microscopy (STM). At the higher chloride concentration (50  $\mu$ M), rapid dissolution of Au atoms and step line recession are observed in the recorded *in-situ* STM images. The high surface mobility of Au atoms resulted in a lack of detectable vacancy islands in the images with minimal changes in cyclic voltammograms (CVs) and the complete absence of nano-island formation, which is observed in pure sulfuric acid. At moderate concentration (10  $\mu$ M),

## 4.2. Introduction

---

the dissolution rate decreased substantially so that the initial step lines are still distinguishable after the 200 ORCs. The lower surface mobility leads to the formation of vacancy islands in the terraces and these newly formed step sites give rise to additional peaks in the CVs. At the lowest concentration (1  $\mu$ M), nano-island formation is observed. However, inhomogeneous chloride adsorption (showing as darker areas in the EC-STM images) on the sample at high enough anodic potential (0.9 V) led to previously unreported behavior, showing very inhomogeneous roughening, with parts on the surface showing reduced Au atom mobility and minimal changes even after the 200 ORCs.

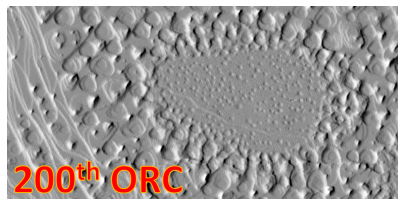
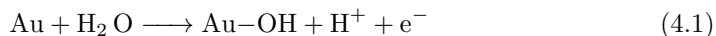


Figure 4.1

## 4.2 Introduction

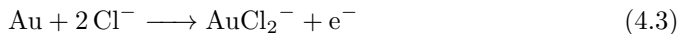
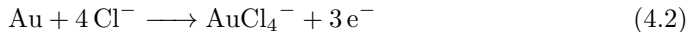
The excellent chemical stability of Au leads to its extensive use in various electrochemical conditions. To understand the detailed surface chemistry of Au, Au single crystals have been studied both in ultra-high vacuum (UHV) [43, 44] and aqueous electrochemical environments [45, 46, 47]. Au oxidation has been studied in sulfate- and perchlorate-containing electrolytes. [46, 48, 8, 22] In sulfate-containing electrolytes, at sufficiently positive potential, sulfate anions will form an ordered adlayer on Au(111)[23], which influences the onset potential for surface oxidation by blocking by adsorbed anions. The oxidation starts with electroadsortion of  $OH^-$ :



At higher potentials, the formation of  $Au(OH)_3$ ,  $AuOOH$ , and  $Au_2O_3$  has been suggested[49]. Successive oxidation-reduction cycles (ORC) applied to the Au(111) single crystal electrode in sulfuric acid creates a highly roughened surface with long-range nanopatterns[45, 50]. The surface roughness is caused by oxide formation pushing out Au surface atoms, which form adatom and vacancy islands after subsequent reduction[42]. If the electrode is paused within the double layer potential window, the

## Chapter 4. Effect of Trace Amounts of Chloride on Roughening of Au(111) Single-Crystal Electrode Surface in Sulfuric Acid Solution during Oxidation-Reduction Cycles

surface mobility of the Au surface atoms will smoothen the surface, making the final roughness very sensitive to the times spent at different potentials[50]. It is well known that the electrochemical behavior of Au surfaces is very sensitive to trace amounts of chloride ions present in the electrolyte[51, 52]. Both one and three electron oxidation processes have been proposed for Au dissolution at positive potentials[52, 53]:



Thus, in the presence of chloride, Au surface oxidation and Au dissolution occur simultaneously at anodic potentials. At high concentration of chloride (1 mM) in perchloric acid, anisotropic dissolution of Au was reported[54]. Moreover, apart from causing dissolution during the ORCs, trace amounts of chloride can enhance the step motion and prevent roughening[55]. Investigation of step dynamics on Au(111) in chloride-containing electrolytes showed that the specifically absorbed chloride can change the dominant mass transport mode from terrace diffusion to edge diffusion[56].

In this study, we conduct an in-depth in situ electrochemical scanning tunneling microscopy (EC-STM) study of the oxidation-reduction cycling of an Au(111) electrode with varying chloride ion concentrations in 0.1 M sulfuric acid. We show how these changes in electrolyte composition influence surface evolution during the ORCs, particularly the role of chloride on the dissolution rate, roughening process, and Au surface atom mobility. Notably, at the lowest chloride concentration, we show how chloride appears to amplify the inhomogeneity of the surface, by roughening certain parts of the surface while other parts remain unaltered.

4

### 4.3 Experimental

#### 4.3.1 EC-STM measurements

The Electrochemical Scanning Tunneling Microscope (EC-STM) images were captured using a custom-built instrument developed at the Leiden Institute of Chemistry (LIC) at Leiden University. More information about the instrument can be found in our previous paper[50]. The tips were fabricated from a platinum/iridium wire (90/10) using the pulling-cutting method. To minimize additional faradaic currents at the tip, a layer of hot melt adhesive (EVA-copolymer, synthetic resin, Wax, and Stabilizer, Brand: C.K.) was applied, leaving only the apex of the tip exposed. A disk-shaped

#### 4.4. Results and discussion

---

single-crystal electrode Au(111) (10 mm diameter) with an Au wire welded to the back was used as the working electrode (WE). The crystal was cut with a precision of 0.1° and polished to a roughness of 30 nm by the Surface Preparation Laboratory (SPL) in the Netherlands. Before each measurement, the Au(111) sample was annealed using a butane flame torch until it turned orange, maintained for 5 minutes, and then cooled in air above ultrapure water to prevent contamination of the sample surface. A high-purity Au wire was used as the counter electrode (CE), and a reversible hydrogen electrode (RHE, Hydroflex, Gaskatel) was used as the reference electrode (RE). Images were recorded in constant current mode with a current setpoint ranging from 50 to 150 pA and a tunneling bias of 10 to 20 mV. The tip was retracted hundreds of nanometers during the CV recording. Throughout the experiment, the EC-STM chamber was purged with ultra-high-purity argon gas to minimize the dissolution of oxygen or other gases into the EC-STM cell. Despite these efforts, there is still a possibility that a trace amount of oxygen is present. We expect trace oxygen or oxygen reduction on the Au surface to be only a very minor, if at all, disturbance to the surface structure.

##### 4.3.2 Electrochemical Cell and Electrolyte

A custom-made Pyrex glass cell was utilized for standard electrochemical experiments. All glassware and plastic components were thoroughly cleaned by soaking in a permanganate solution (0.5 M sulfuric acid and 1 g/L potassium permanganate) for a minimum of 12 hours before each experiment. After rinsing with Milli-Q water, the components were treated with a diluted piranha solution (3:1 mixture of sulfuric acid ( $H_2SO_4$ ) and hydrogen peroxide ( $H_2O_2$ ), diluted with water) to eliminate manganese oxide and permanganate residues. To remove any remaining diluted piranha, all parts were boiled at least five times. The electrolyte, composed of  $H_2SO_4$  (96% Suprapur Sigma Aldrich) and HCl (30% Suprapur Sigma Aldrich), was prepared using ultra-high purity (UHP) Milli-Q water (resistivity  $> 18.2\text{ M}\Omega\cdot\text{cm}$ ) and degassed with ultra-high purity argon gas for at least 30 minutes. All measurements were conducted at room temperature ( $T = 293\text{ K}$ ).

### 4.4 Results and discussion

The roughening process of Au(111) in 0.1 M sulfuric acid has been studied well in previous works[50, 45]. In order to be able to compare and clearly distinguish the role of chloride during the ORCs, the sulfuric acid concentration is kept constant in all

## Chapter 4. Effect of Trace Amounts of Chloride on Roughening of Au(111) Single-Crystal Electrode Surface in Sulfuric Acid Solution during Oxidation-Reduction Cycles

experiments and the chloride concentration was varied between 1, 10, and 50  $\mu\text{M}$ .

### 4.4.1 Oxidation-reduction cycles of Au(111) in 0.1 M $\text{H}_2\text{SO}_4$ and 50 $\mu\text{M}$ HCl

The first experiment is devoted to the highest chloride concentration, i.e. 50  $\mu\text{M}$ . Figure 4.2a shows the sample surface in 0.1 M  $\text{H}_2\text{SO}_4$  and 50  $\mu\text{M}$  HCl at 0 V vs. RHE just after the annealed Au(111) electrode. The differential image shown on the bottom-right side of the image gives a better contrast to see the Au(111) reconstruction pattern. Moreover, some step lines can be seen, which will be useful since we expect some dissolution from step lines after applying CVs. Thus, having these step lines in the scan area can help to evaluate step line activity. The top half of Figure 4.2b is recorded at 0.6 V and the bottom half (below the dashed line) at 0.7 V vs RHE. Formation of the small adatom islands is clear at 0.7 V. After applying 0.8 V vs RHE, Figure 4.2c was recorded, which shows some large monoatomic islands and one vacancy island. The most likely reason for these large islands is the increased mobility of the Au surface atoms in the presence of (adsorbed) chloride[57, 56] so that the Au adatom islands have grown (Ostwald ripening) before image recording. The shape and size of the islands are smaller and more triangular in pure sulfuric acid, but with chloride, their size increases while their shape is more circular. After five consecutive ORCs with 0.9 V and 1.7 V as the lower and upper potential limit (scan rate of 50  $\text{mV s}^{-1}$ ), Figure 4.2d was recorded. Comparing this frame with the previous one, two main differences can be noted: all the adatom islands have dissolved and step line recession has taken place, as most clearly evidenced by the disappearance of the narrow terrace. The red dashed line represents the step lines before applying 5 ORCs (Figure 4.2c). After ten ORCs, the image in Figure 4.2e shows more step-line recession but no vacancy islands. Two possible mechanisms can be considered for this behavior. Either the dissolution of Au atoms only takes place at the step edges and the terraces stay unchanged, or there is also some dissolution taking place on the terraces but the mobility of the atoms is so high that the vacancy islands effectively move quickly[58] until they are captured by the step lines and vanish[59]. The latter case is more probable since some large vacancy islands appear after 50 ORCs, as illustrated in Figure 4.2f. This indicates that Au dissolution is also taking place from the terraces. The step-line recession is now so severe that the initial step-lines cannot be observed anymore. Figures 4.2g, 4.2h, and 4.2i show the surface development after 100, 150, and 200 ORCs, respectively, confirming that a higher cycle number leads to more

#### 4.4. Results and discussion

---

dissolution and continuing step-line recession.

From the above experimental results, we conclude that with a (relatively) high concentration of chloride in solution, surface oxidation and subsequent reduction do not lead to roughening (formation of adatom and vacancy islands). The dominant process on the surface is Au dissolution by reactions 4.2 and/or 4.3. Moreover, the mobility of the chloride-covered Au atoms is so high that vacancy islands are also highly mobile and the surface development at higher ORC numbers is mostly taking place by step line recession.

Figure 4.3a presents the recorded CVs on Au(111) in 0.1 M  $\text{H}_2\text{SO}_4$  and 50  $\mu\text{M}$  HCl with a scan rate of  $50 \text{ mVs}^{-1}$  in the potential window of 0.9 V to 1.7 V vs RHE. The first cycle (in blue) does not differ substantially from the last cycle (in red). As evident from the EC-STM images, at high chloride concentrations, the surface roughness does not change very much (mainly dissolution and step line recession), as confirmed by the essentially identical CVs over 200 cycles. The main anodic and cathodic peaks are taking place at 1.55 V and 1.19 V vs RHE, respectively. The small anodic current peak at 1.13 V seems to be correlated to chloride adsorption since this peak disappears for lower concentrations of chloride. The small cathodic peaks at 1.09 V can be correlated to the desorption of chloride and minor redeposition of dissolved Au atoms. Figure 4.3c shows the calculated charge density for both oxidation and reduction peaks as a function of cycle number. Except for the few first cycles, the charge density shows a plateau, in line with the absence of roughening. The large difference between the oxidation and reduction charge density is due to the Au dissolution process.

##### 4.4.2 Oxidation-reduction cycles of Au(111) in 0.1 M $\text{H}_2\text{SO}_4$ and 10 $\mu\text{M}$ HCl

For the next experiment, the concentration of hydrochloric acid was reduced to 10  $\mu\text{M}$ . This change can help to pinpoint the role of trace levels of chloride on the surface evolution over many ORCs. Figure 4.4a shows the differential image of the pristine surface at 0 V vs RHE after the annealing, which shows herringbone reconstruction on the large terraces. There are some adatom and vacancy islands in the bottom-left part and these defects have been observed in many previous experiments showing that the annealed sample (with the corresponding method) is not flawless. The potential is then increased to the point that the reconstruction lifting process initiates. It is known that the lifting of reconstruction happens in several stages[60]. Figure 4.4b shows the differential image recorded at 0.7 V vs RHE. Some small monoatomic is-

**Chapter 4. Effect of Trace Amounts of Chloride on Roughening of Au(111) Single-Crystal Electrode Surface in Sulfuric Acid Solution during Oxidation-Reduction Cycles**

4

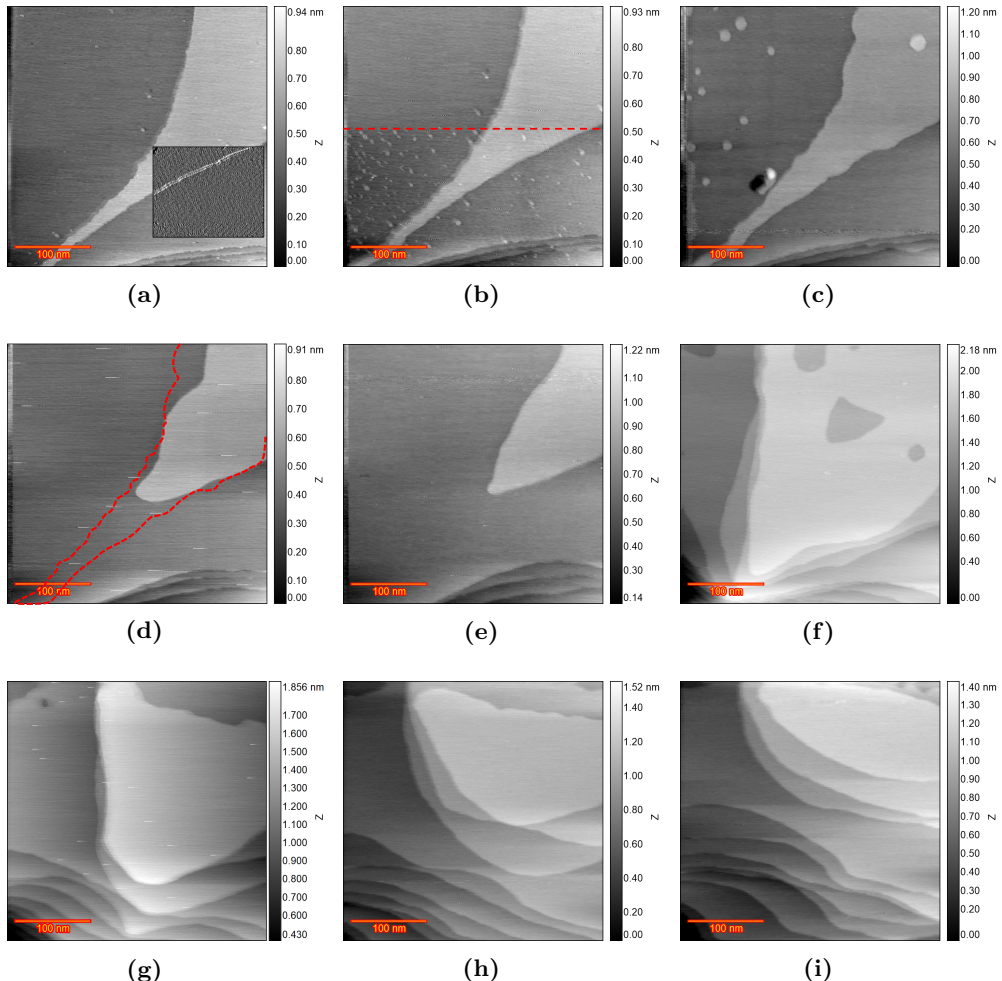


**Figure 4.2:** EC-STM images ( $350 \times 350$  nm) of Au(111) in  $0.1$  M  $\text{H}_2\text{SO}_4$  and  $50$   $\mu\text{M}$   $\text{HCl}$ .  
 a) Sample surface at  $0$  V vs RHE just after annealing. b) Top half is recorded at  $0.6$  V and from the red arrow downward, the EC voltage changed to  $0.7$  V. c) Fully lifted reconstruction at  $0.8$  V, d) after  $n=5$  ORCs, e)  $n=10$ , f)  $n=50$ , g)  $n=100$ , h)  $n=150$  i)  $n=200$ .

#### 4.4. Results and discussion

---

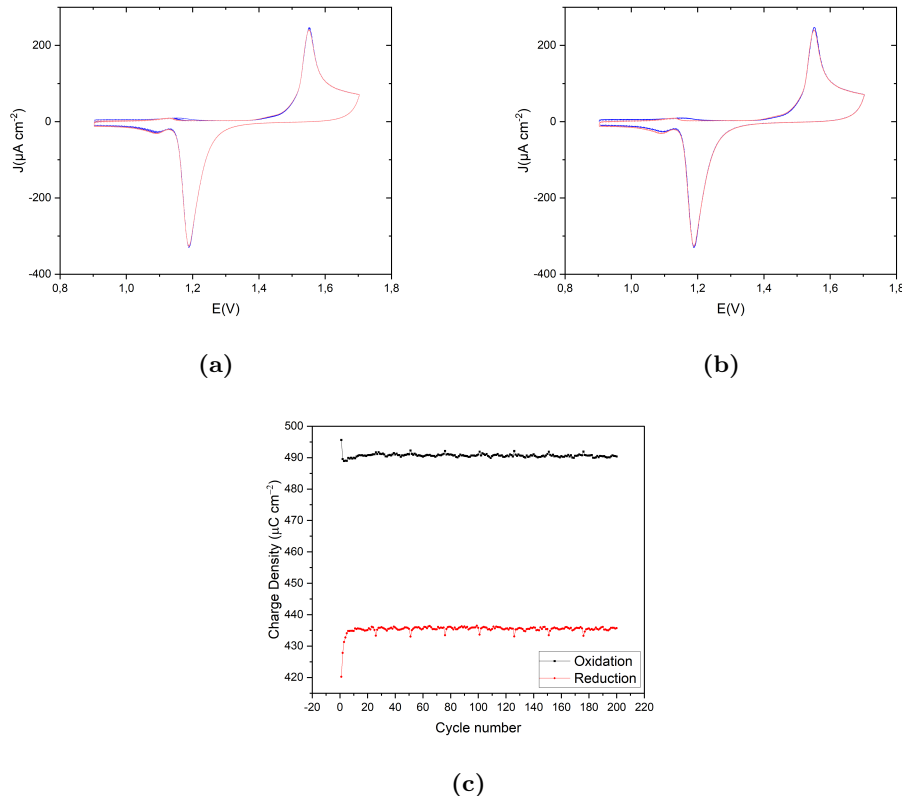


**Figure 4.3:** a) Cyclic voltammograms of the consecutively applied 200 ORCs on Au(111) in 0.1 M  $\text{H}_2\text{SO}_4$  and 50  $\mu\text{M}$  HCl with a scan rate of 50  $\text{mVs}^{-1}$  versus RHE. The color spectrum ranges from blue for the first cycle to red for the last cycle. b) First and last cycle in blue and red respectively for a better representation. c) Calculated oxidation(black) and reduction(red) charge density ( $\mu\text{C cm}^{-2}$ ) versus the cycle number for the CVs shown in (a).

## Chapter 4. Effect of Trace Amounts of Chloride on Roughening of Au(111) Single-Crystal Electrode Surface in Sulfuric Acid Solution during Oxidation-Reduction Cycles

4

lands are showing up at the very top of the image, which indicates the lifting of the reconstruction at that spot. However, the compact herringbone can still be seen in the middle and bottom parts, which indicates the local charge density is not high enough to initiate the lifting. Also, there is a spot between the aforementioned areas indicated with red spheroids which shows some distorted reconstruction, which can be considered as an intermediate stage. This suggests that even at the same potential, different areas can exhibit slightly different behaviors concerning surface reconstruction. At 0.8 V vs RHE, the reconstruction is fully lifted, as is shown in Figure 4.4c, since there is no sign of herringbone and the entire surface is covered with monoatomic islands. The island density is lower on the terraces near the upward step lines and this can be due to the capturing of the atoms/islands by the step line. Regarding the island shape, no preferred step type/direction is observed and islands appear circular. The island size is less than in the captured frame in Figure 4.2c for higher chloride concentration. Figure 4.4d was recorded after 5 ORCs within the same potential window. The number of islands reduced substantially while their size increased, which can be caused by Ostwald ripening. Moreover, some slight changes in the step lines can be observed (i.e. smoothening the rough step line on the bottom-left corner). The red dashed line shows the same step line in the previous frame. In 50  $\mu\text{M}$  chloride, no adatom islands were left at this cycle number (Figure 4.2d) and the step line receded much more (by comparison of the dashed lines and the new step lines after 5 ORCs) which underscores the chloride role in the surface evolution. After 10 ORCs, Figure 4.4e shows only five adatom islands and some more recession at the step line (e.g. see the step in the bottom left). After 20 ORCs, the dissolution of all the adatom islands took place, simultaneously with the formation of vacancy islands, as shown in Figure 4.4f. Figure 4.4g was taken after 50 ORCs and shows larger vacancy islands with a few adatom islands at the bottom part. Those islands can be related to the redeposition of dissolved Au atoms during the negative-going voltage sweep. Figure 4.4h and 4.4i show the result after 100, and 200 ORCs respectively. It is clear that the higher number of ORCs is causing more Au dissolution causing the formation of new vacancy islands and recession of the step lines.

Figure 4.5a presents the recorded CVs of Au(111) in 0.1 M  $\text{H}_2\text{SO}_4$  and 10  $\mu\text{M}$  HCl with a scan rate of 50  $\text{mV s}^{-1}$  in the potential windows of 0.9 V to 1.7 V vs RHE. The first cycle (in blue) to the last cycle (in red) shows only slight changes. Specifically, the amplitude of the main anodic peak at 1.63 V reduces and shifts slightly to the higher potential at higher ORC numbers, and a small anodic peak emerges at 1.54 V with its amplitude increasing with the ORC number. We expect this peak to be

#### 4.4. Results and discussion

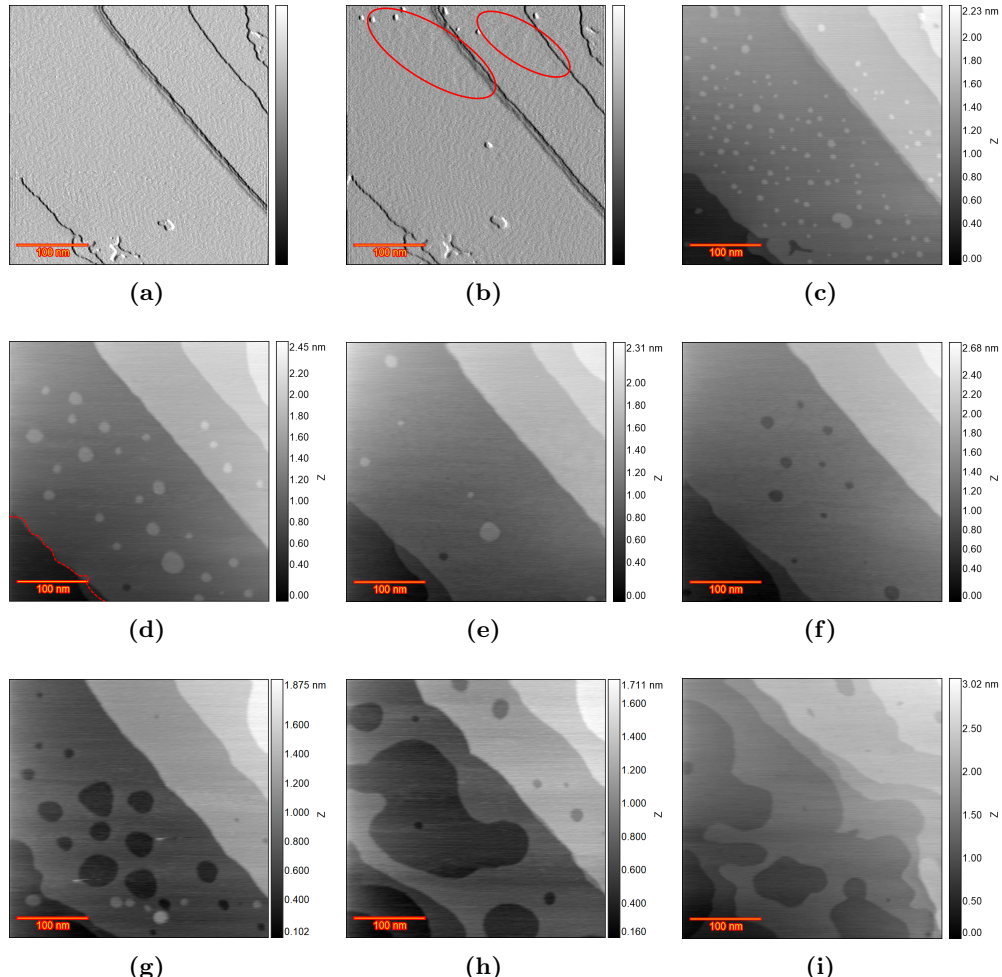


**Figure 4.4:** EC-STM images ( $350 \times 350$  nm) of Au(111) in  $0.1$  M  $\text{H}_2\text{SO}_4$  and  $10$   $\mu\text{M}$   $\text{HCl}$ . a) differential image of the pristine surface at  $0.6$  V vs RHE after thermal annealing. b) differential image of partially lifted reconstruction at  $0.7$  V vs RHE. c) Fully lifted reconstruction at  $0.8$  V, d) after  $n=5$  ORCs, e)  $n=10$ , f)  $n=20$ , g)  $n=50$ , h)  $n=100$  i)  $n=200$ .

## Chapter 4. Effect of Trace Amounts of Chloride on Roughening of Au(111) Single-Crystal Electrode Surface in Sulfuric Acid Solution during Oxidation-Reduction Cycles

related to oxidation at the step sites. The main cathodic peak is located at 1.15 V with no shoulder peaks for the first cycle. With more cycles, another peak appeared at 1.18 V very close to the main cathodic peak, and a small shoulder at 1.11 V (indicated with an arrow in Figure 4.5b). The small cathodic shoulder peak at 1.11 V is likely correlated to the redeposition of dissolved Au atoms since the concentration of dissolved Au atoms in the diffusion layer is initially very low but after more cycles, it can show up. Figure 4.5c shows the calculated charge density for both oxidation and reduction peaks as a function of ORC number. After 20 ORCs, there is a linear decay for both charge densities and as expected, the reduction charge is lower than the oxidation charge. The difference between oxidation and reduction charge is less than in the experiment with 50  $\mu$ M, showing that the extent of Au dissolution is related to the chloride concentration.

4

### 4.4.3 Oxidation-reduction cycles of Au(111) in 0.1 M $\text{H}_2\text{SO}_4$ and 1 $\mu$ M HCl

For the final experiment, the chloride concentration was reduced to 1  $\mu$ M. Figure 4.6a shows the pristine Au(111) surface at 0 V vs RHE after the annealing: there are only two terraces with a curved step line in the scanning area. Figure 4.6b contains two parts which are separated by the red dashed line: the top half is recorded at 0.8 V vs RHE and the bottom half at 0.9 V. The top half shows a vacancy island surrounded by adatom islands formed on the top right part of the image. This feature appeared at 0.6 V and can be related to having some contaminations/defects in the sample which leads to this early island formation. Other than that, no substantial change is observed in the top half. On the other hand, in the bottom half the reconstruction is lifted. It is important to notice the darker areas that appeared in the bottom part, along with the lifting of the reconstruction. The darker area suggests a different local work function, which can alter the local tunneling current magnitude. Since all the images are recorded in constant current mode, the feedback system will compensate for that change by adjusting the tip height. Thus, the change in the work function can be seen as some depressions in the surface. These changes in height would then not correspond to a real topographic feature of the sample. The influence of the adlayer on the topographical image of Cu(111) has previously been observed as a lower height of the terrace (ca. 0.05 nm) and assigned to lower conductivity of Cu terrace covered by adsorbates[61]. Although we do not expect surface oxidation at 0.9 V, similar patches have been observed on Au(111) when an oxide layer is forming[62]. This implies that

#### 4.4. Results and discussion

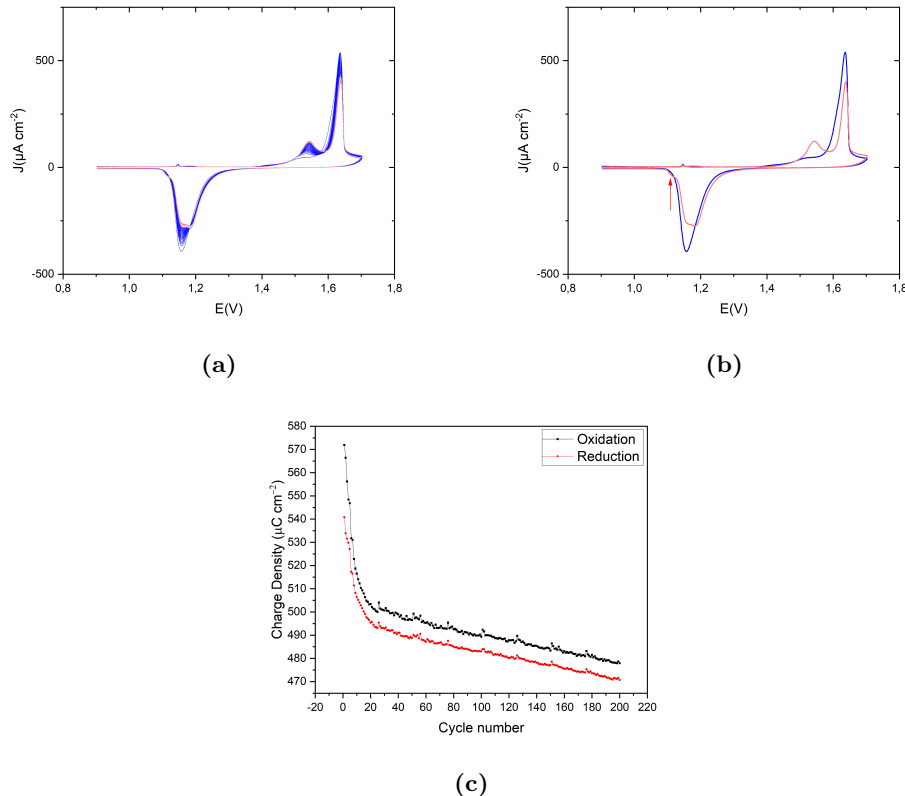


**Figure 4.5:** a) Cyclic voltammograms of the consecutively applied 200 ORCs on Au(111) in 0.1 M  $\text{H}_2\text{SO}_4$  and 10  $\mu\text{M}$  HCl with a scan rate of  $50 \text{ mV s}^{-1}$  versus RHE. The color spectrum ranges from blue for the first cycle to red for the last cycle. b) First and last cycle in blue and red respectively for a better representation. c) Calculated oxidation(black) and reduction(red) charge density ( $\mu\text{C cm}^{-2}$ ) versus the cycle number for the CVs shown in (a).

## Chapter 4. Effect of Trace Amounts of Chloride on Roughening of Au(111) Single-Crystal Electrode Surface in Sulfuric Acid Solution during Oxidation-Reduction Cycles

any factor influencing the work function can lead to comparable results. What causes the local work function changes, with presumably a correspondingly different anion adsorption, remains unfortunately unresolved. Interestingly, the island size in those darker areas in Figure 4.6b is smaller than at other locations. This suggests that the composition of the interface in these regions must be different from elsewhere. Since this behavior is not observed in a pure sulfuric acid solution, the emergence of these areas should be attributed to the presence of a trace level of chloride anions and their influence on the surface chemistry. The next frame in Figure 4.6c is recorded at 0.9 V vs RHE; the large dark area is now located in the center of the image. Moreover, there are some new small dark spots at the bottom half, which were not (yet) observed in the previous image. This can be caused by the tip effect or by some extra adsorption/desorption of anions at this potential. The former reason is less probable since the STM scan line is from left to right. In case of a tip effect on the double-layer composition of the darker areas, enlargement of the dark areas in that direction would be expected, however, there are many new spots, spatially separated, without a clear direction. The second reason would imply a certain slowness in the surface chemistry, which may be related to the very low chloride concentration. Figure 4.6d was recorded after five ORCs. It is obvious that the surface response on the dark areas is different from the rest of the sample surface since it seems that neither roughening nor dissolution is taking place there. The result for other spots is very similar to the experiment in pure sulfuric acid[50] which shows normal roughening caused by the place exchange mechanism during ORCs leading to rounded-edge triangular islands. This observation implies that there is a direct correlation between the dark regions and the unroughened regions after the ORCs. Figure 4.6e shows the result after 10 ORCs. Surprisingly, even up to this cycle number, the darker areas stayed pristine. However, at  $n=50$  shown in Figure 4.6f, those areas are shrinking slowly, which can be caused by the tip effect or by the ORCs. At higher cycle numbers of 100, 150, and 200 (Figures 4.6g, 4.6h, and 4.6i), the surface is becoming more homogeneously roughened, but some differences still can be observed.

The zoomed-out frame recorded after running 200 cycles is shown in Figure 4.7a. The initial scan area is located almost at the center of the image and the comparison with the rest of the image suggests that less roughening took place in the initial scan area. Thus, locations with a smaller/no contribution of chloride anions behave very similarly to pure sulfuric acid[50]. A further zoomed-out image is shown in Figure 4.7b. The red square indicates the initial scan area of Figure 4.6. Some areas remain pristine, as highlighted by the yellow circles. Figure 4.7c shows the same image in Figure 4.7b

#### 4.4. Results and discussion

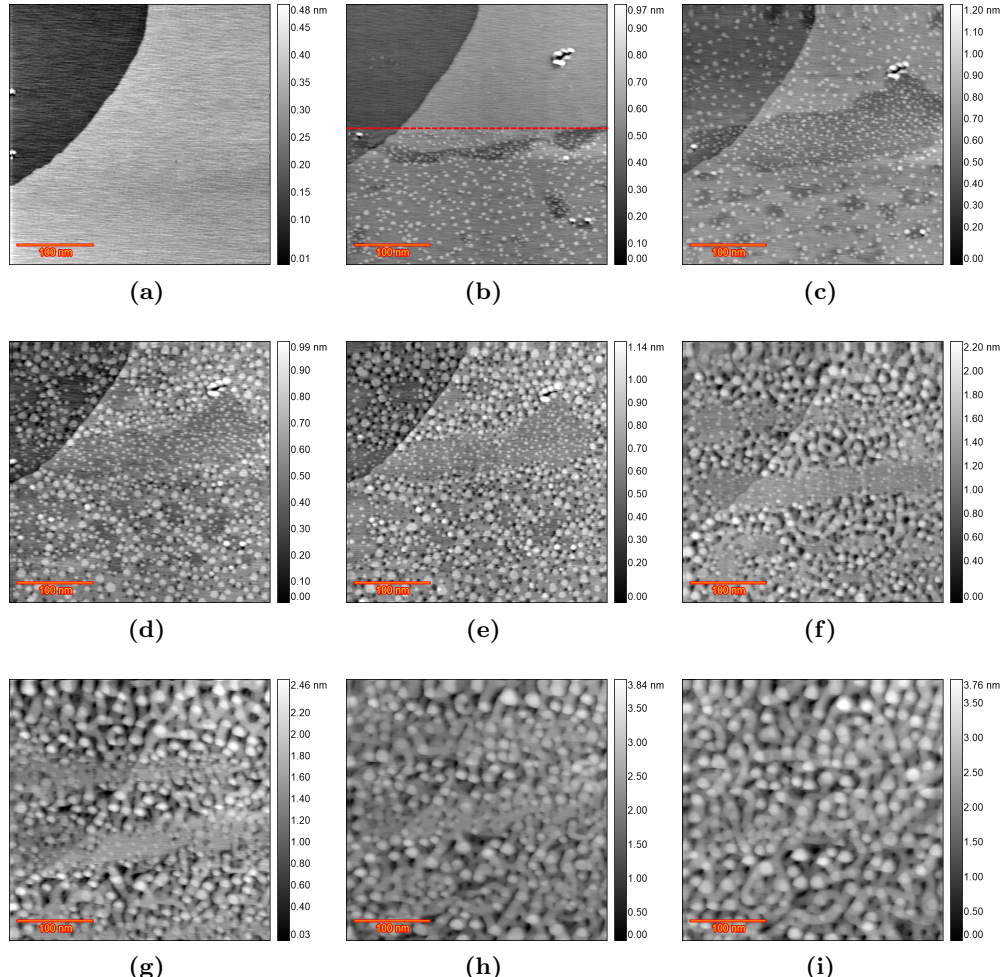


**Figure 4.6:** EC-STM images ( $350 \times 350$  nm) of Au(111) in  $0.1$  M  $\text{H}_2\text{SO}_4$  and  $1$   $\mu\text{M}$   $\text{HCl}$ .  
a) The pristine surface at  $0$  V vs RHE after annealing. b) The top half is recorded at  $0.8$  V and from the red dashed line downward, the EC voltage changed to  $0.9$  V. c) Fully lifted reconstruction at  $0.9$  V with the emergence of some darker spots. d) after  $n=5$  ORCs, e)  $n=10$ , f)  $n=50$ , g)  $n=100$ , h)  $n=150$  i)  $n=200$ .

## Chapter 4. Effect of Trace Amounts of Chloride on Roughening of Au(111) Single-Crystal Electrode Surface in Sulfuric Acid Solution during Oxidation-Reduction Cycles

in differential mode for better visualization. Figure 4.7d shows the zoomed-in image of the unroughened areas in differential mode. Small adatom islands, which are the result of the lifting of the reconstruction, are noticeable within these areas and a step line is also visible. The transition area between roughened and unroughened areas contains smaller islands which suggests that the border between the two areas is not abrupt, or that islands grow by adatoms (generated by place exchange mechanism in the roughened region) diffusing from all directions, which becomes discontinuous at the borders.

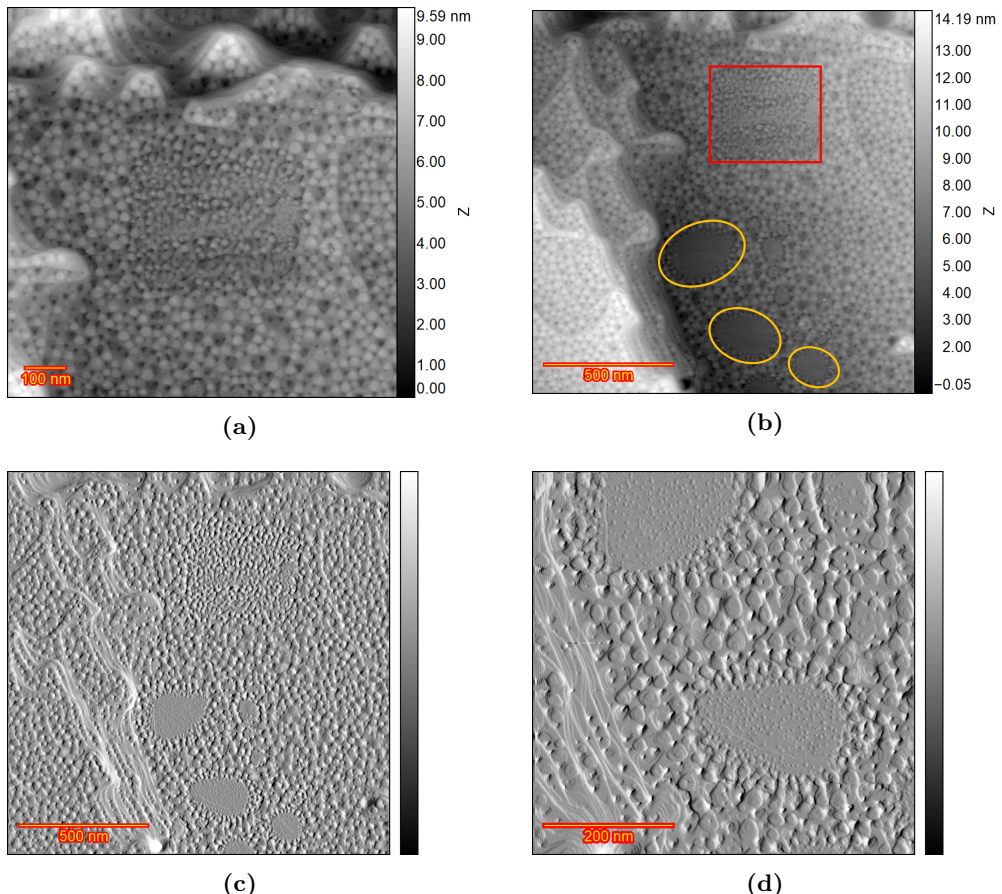


**Figure 4.7:** Au(111) in  $\text{H}_2\text{SO}_4$  and  $1 \mu\text{M}$  HCl after 200 ORCs a) Large scan area which includes the initial scan area at the center. b) Further zoomed-out frame which contains the initial scan area and some spots with no roughening. c) The differential image of the frame shown in (b). d) Zoomed-in image on the spots with no roughening.

Figure 4.8a presents the recorded CVs of Au(111) in  $0.1 \text{ M}$   $\text{H}_2\text{SO}_4$  and  $1 \mu\text{M}$  HCl

#### 4.4. Results and discussion

---

with a scan rate of  $50\text{ mVs}^{-1}$  in the potential window of 0.9 V to 1.7 V vs. RHE. The first cycle (in blue) to the last cycle (in red) shows slight changes only in the anodic peak shape, while the reduction peak shape is almost constant. The amplitude of the main anodic peak at 1.62 V reduces and shifts to a slightly lower potential for the first five cycles; for higher cycle numbers, the amplitude shifts to a higher current density and potential. Moreover, a small and broad anodic peak emerges at 1.42 V, its intensity increasing with cycle number. The main cathodic peak is located at 1.16 V, with a very slight reduction over cycles (Figure 4.8b shows the first and last cycle). Figure 4.8c shows the calculated charge density for both oxidation and reduction peaks with cycle number, showing a quick lowering and subsequent rising of the charge, followed by a slow decay.

From the above results, it is clear that chloride-induced Au dissolution plays an important role in the surface development of Au electrodes during oxidation-reduction cycles. Figure 4.9 illustrates the effect of chloride concentration by a histogram showing the difference in oxidation and reduction charge densities for all the cycles for the three chloride concentrations. The most frequent value of the difference between oxidation and reduction charge density for 50, 10, and 1  $\mu\text{M}$  chloride are 54.96, 7.21, and 3.94  $\mu\text{C cm}^{-2}$ , respectively. Increased chloride concentrations result in a greater charge difference, underscoring the critical role of chloride ions in facilitating Au dissolution. At a concentration of 50  $\mu\text{M}$ , chloride not only promotes a higher dissolution rate but also enhances surface atom mobility. That explains why more step-line recession and fewer vacancy islands were captured in STM images as the chloride coverage on the surface is at the highest level at this concentration. As the chloride concentration decreases to 10  $\mu\text{M}$ , the reduced mobility of Au atoms allows the capturing of vacancy islands. At the lowest HCl concentration (1  $\mu\text{M}$ ), some regions outside the initial scanned area in Figure 4.7b, remained pristine even after 200 cycles, indicating that tip effects were primarily responsible for the observed roughening in darker regions by disturbing the interfacial layer in repeated surface scans after ORCs. The tip effect is only important in 1  $\mu\text{M}$  HCl because under these conditions, any inhomogeneities in the surface properties appear to become amplified and hence become susceptible to disturbances from the tip. In contrast, this disturbance was not important in other experiments due to the greater homogeneity of the surface. Formation of the areas with different levels of roughening is likely due to the inherent inhomogeneity in the surface which would be amplified by the chloride-containing electrolyte for instance by having a different adsorbed adlayer. Perhaps there is a threshold (local) chloride concentration required to form an adlayer containing chloride, which could lead to this unexpected

**Chapter 4. Effect of Trace Amounts of Chloride on Roughening of Au(111) Single-Crystal Electrode Surface in Sulfuric Acid Solution during Oxidation-Reduction Cycles**

4

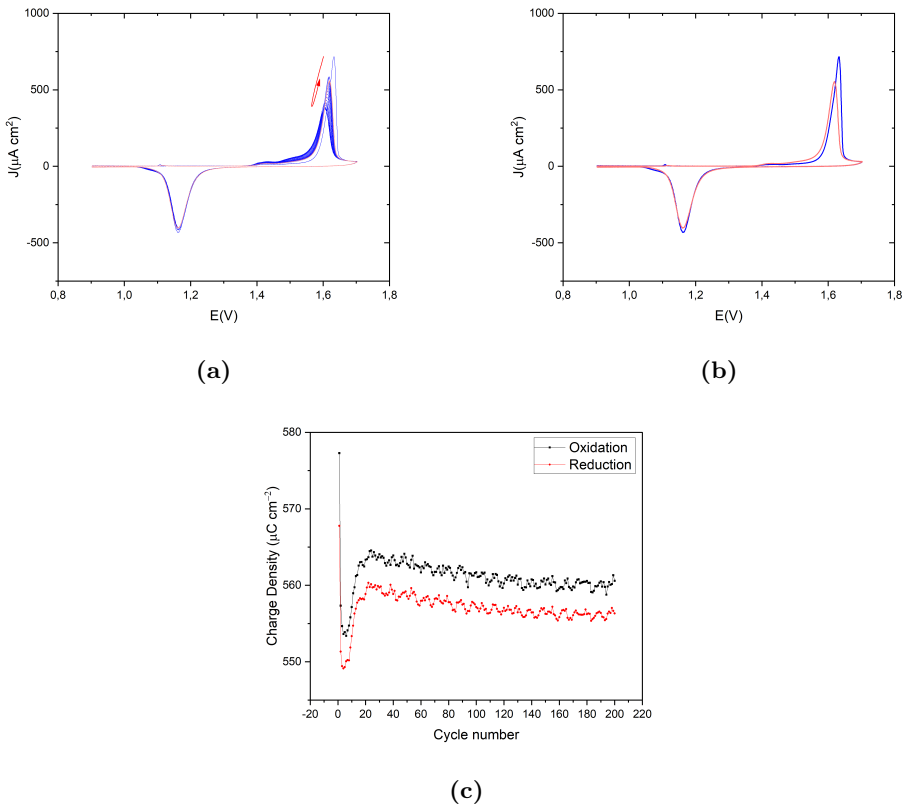


**Figure 4.8:** a) Cyclic voltammograms of the consecutively applied 200 ORCs on Au(111) in 0.1 M  $\text{H}_2\text{SO}_4$  and 1  $\mu\text{M}$  HCl with a scan rate of  $50 \text{ mV s}^{-1}$  versus RHE. The color spectrum ranges from blue for the first cycle to red for the last cycle. The arrow shows the trajectory of the oxidation peak. b) First and last cycle in blue and red respectively for a better representation. c) Calculated oxidation(black) and reduction(red) charge density ( $\mu\text{C cm}^{-2}$ ) versus the cycle number for the CVs shown in (a).

#### 4.5. Results and discussion

---

amplifying behavior. It seems that in those spots that are not roughened, Au atom surface mobility is very low since the small adatom islands did not go through ripening steps. Reduction in surface mass transport rates is expected in areas with different absorbed layers. Previous STM studies of Au(111) in UHV studied the effect of sulfur and oxygen, the lifting of the reconstruction by sub-monolayer S coverage, and the adlayer structure of S adatoms [63, 64, 65, 66]. Adsorbed sulfur on Au(111) was shown to have an effect on the enhancement of the decay rate of monoatomic Au islands[67]. It has been proposed that chemisorbed species can improve metal surface dynamics by forming metal-additive complexes which can lead to easier mass transport across the surface on Cu and Ag samples[68, 69]. Accordingly, sulfate and other adsorbates can modify electrochemical reactions, Au atom mobility, the formation energy of step lines and kinks, and other related processes in various crystallographic orientations. In addition, adsorbed sulfate presumably inhibits the adsorption of impurities. These influences collectively determine the dynamics of roughening, the shape of islands, and the final surface roughness after the ORCs. Moreover, neither oxidation (place exchange mechanism) nor Au dissolution appears to have taken place in the spots that were not roughened. This behavior was observed in many other experiments on Au(111) in 0.1 M  $\text{HClO}_4$  (which has some small chloride contamination out of the bottle)[70]. Thus, we infer a correlation between the trace amount of chloride and the roughened areas on the sample. There is another somewhat puzzling anomaly in the behavior of the system with 1  $\mu\text{M}$  chloride, and that is the cycle dependence of the oxidation and reduction charge density. For 50  $\mu\text{M}$  chloride, there is no cycle dependence (Fig.4.3c), in agreement with the lack of surface changes under those conditions. For 10  $\mu\text{M}$  chloride, the oxidation/reduction charge density decreases with cycle number (Fig.4.5c). This is in qualitative agreement with our previous work (using 0  $\mu\text{M}$  chloride) and was interpreted as the loss of (111) terraces during cycling (as Au(111) has the highest oxidation/reduction charge density). Remarkably, for 1  $\mu\text{M}$  chloride, the oxidation/reduction charge density first decreases (signifying the loss of 111 terraces), then increases again (suggesting the formation of new 111 facets?), and subsequently decreases again. We have no good explanation for this behavior at present, but it could be that we are seeing the superposition of two signals, one from the part of the surface that is roughening, and another from the part that is not roughening. Future studies could examine whether trace amounts of oxygen in the electrolyte would influence the system in any way.

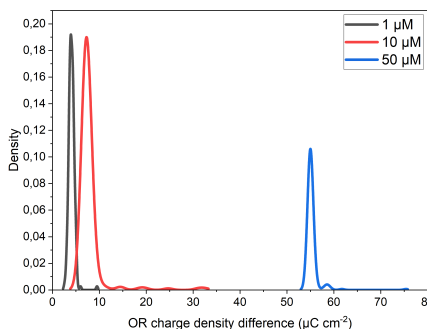


**Figure 4.9:** The histogram displays the distribution of 200 ORCs based on their charge density difference (X-axis, in  $\mu\text{C cm}^{-2}$ ) in 0.1 M  $\text{H}_2\text{SO}_4$  and different concentrations of HCl. The Y-axis, labeled density, represents the probability density of ORCs in each bin.

## 4.5 Conclusions

In this work, we performed an in-situ EC-STM study of the evolution of an Au(111) electrode surface during 200 Oxidation Reduction Cycles (ORCs) in 0.1 M sulfuric acid with varying concentrations of HCl. The findings demonstrate how even a minor chloride concentration significantly alters the surface dynamics and surface roughening. Chloride ions rapidly dissolve Au atoms at the highest concentration (50  $\mu\text{M}$ ). Moreover, the high surface atom mobility under these conditions prevents the formation of detectable vacancy islands in the captured images during the cycles, with only step-line recession being observed. Consequently, only a few new step sites are generated, leading to minimal changes in the CVs and constant oxidation and reduction charge densities, and the complete absence of surface roughening. The pronounced difference between the oxidation and reduction charges further proves the high dissolution rate of Au atoms. At the lower chloride concentration (10  $\mu\text{M}$ ), the dissolution occurs at a significantly slower rate (given the comparison of the step line recession and disappearing of adatom islands), allowing the recognition of the initial step lines in the recorded image after multiple ORCs. The reduced atom mobility facilitates the imaging of vacancy islands formed due to Au dissolution at terrace sites. These newly emerging step sites result in the appearance of two additional cathodic and anodic peaks in the recorded CVs. The oxidation and reduction charge densities exhibit a roughly logarithmic decay, resembling the behavior in pure sulfuric acid, indicating the inactivity of the new step sites in contributing to oxidation and reduction charges.

#### 4.5. Conclusions

---

Finally, at the lowest chloride concentration (1  $\mu\text{M}$ ), an apparent inhomogeneity in chloride adsorption was observed, leading to the formation of dark areas after the absorbed layer developed at positive potentials (0.9 V). These areas displayed distinct behavior: Au atom mobility was reduced, as indicated by the smaller island sizes, and the cycling caused no noticeable changes or roughening even after 200 ORCs (in regions undisturbed by repeated scanning with the tip). The overall oxidation and reduction charge density exhibited a multimodal behavior as a function of cycle number, the nature of which remains to be understood in detail.

# Chapter 5

# Anisotropic Roughening of Au(111) Single-Crystal Electrode Surface in HClO<sub>4</sub> Solution during Oxidation-Reduction Cycles

5

## 5.1 Abstract

This study investigates the inhomogeneous roughening of an Au(111) single-crystal electrode surface during oxidation-reduction cycles (ORCs) in a 0.1 M perchloric acid (HClO<sub>4</sub>) solution using electrochemical scanning tunneling microscopy (EC-STM). The results reveal that, even in ultrapure HClO<sub>4</sub>, the presence of minor impurities can lead to three distinguishable surface evolutions, on one and the same crystal: surface roughening by the formation of adatom and vacancy islands, gold dissolution resulting in vacancy island formation (in conjunction with step line recession), and the surface remaining intact even during oxidation-reduction cycling. The impact of trace impurities, specifically sulfate (SO<sub>4</sub><sup>2-</sup>) and chloride (Cl<sup>-</sup>), on the surface structure development is investigated by adding 10  $\mu$ M of H<sub>2</sub>SO<sub>4</sub> and HCl to the HClO<sub>4</sub> solution. Our results reveal that sulfate significantly promotes uniform roughening,

## 5.2. Introduction

---

while chloride accelerates gold dissolution and step-line recession. These findings highlight the critical role of minor impurities in altering the electrochemical behavior of gold surfaces, and how sensitive the local evolution of the surface structure is to these effects.

## 5.2 Introduction

Gold and its alloys are among the most important materials for various electrochemical applications. Known for its high chemical inertness compared to metals like platinum and its stability in aqueous electrolytes, gold frequently acts as an inert electrode in diverse electrochemical reactions[71, 72]. For example, gold is utilized in electroplating[73, 74], electrochemical sensors[75], and as electrocatalyst for various reactions, specifically for CO<sub>2</sub> reduction, selective oxidation reactions, and oxygen reduction reaction (ORR) to hydrogen peroxide[76, 77, 78]. Additionally, it plays a role in energy storage technologies such as supercapacitors and batteries[79, 80]. Moreover, gold is employed in electroanalytical methods for the precise quantitative analysis of analytes in solution[81]. In particular, gold constitutes an important model system in the context of fundamental principles in electrochemistry, as well as the mechanisms and kinetics of the initial stages of metal oxidation and reduction [82, 83, 84, 85, 56, 86, 87, 88, 6]. Despite its high chemical inertness being advantageous for these applications, the extensive use of gold-based devices is limited by reactivity loss and reduced durability due to structural degradation and dissolution of gold during prolonged use. In fact, oxidation reduction cycles (ORCs) etch gold when sufficient positive potentials are applied[89, 90, 91]. Since elucidating the dissolution mechanism of noble metals like gold is important for both industrial applications and fundamental science, the structure and characteristics of polycrystalline and single crystal surfaces of gold in acidic media, especially in the presence of anions like perchlorate [91, 27, 92, 93, 94, 95], sulfate [89, 27, 8], and chloride [91, 95, 96, 55, 97], have been extensively studied by electrochemical and surface characterization techniques.

At sufficiently positive potentials, sulfate or chloride anions specifically adsorb on the gold surface, forming an ordered sulfate [98, 89, 99] or chloride adlayer[100, 101]. In contrast, perchlorate is considered as a weakly adsorbed anion[102, 91, 55]. As a result, even trace amounts of chloride or sulfate impurities in HClO<sub>4</sub>, which strongly adsorb and may alter the nature of the double layer in a perchlorate solution, can significantly affect the electrochemical behavior of gold, both in terms of voltammetry and surface structure. *In situ* electrochemical scanning tunneling microscopy (EC-

## Chapter 5. Anisotropic Roughening of Au(111) Single-Crystal Electrode Surface in $\text{HClO}_4$ Solution during Oxidation-Reduction Cycles

STM) is an effective technique for capturing the atomic-scale surface evolution of Au(111) from its pristine state through various stages of electrochemical treatment. [27]

Studies of Au(111) electrode in perchloric acid electrolyte after oxidation-reduction cycles (ORCs) with EC-STM have yielded widely varying results. For instance, one study reported the formation of adatom and vacancy islands after ORCs[96], while another observed worm-like islands [93]. Contradictorily, other studies noted the development of pits post-ORCs[97, 55, 95, 94], with the shape and roughness of these pits varying significantly across different reports[27]. Additionally, some studies identified areas with diverse structures, including variations in pit size [27, 94], regions with differing heights and roughness [94, 93], and unexpectedly, areas with less pits and adatom islands adjacent to the initial scan area [94]. These diverse findings underscore the complexity of the double-layer structure in  $\text{HClO}_4$  and highlight the necessity for further investigations in this area of electrochemistry.

In this paper, we conduct a comprehensive study and analysis of the oxidation-reduction process of Au(111) in perchloric acid to gain a deeper understanding of the roughening approach in perchlorate solution. Our aim is to identify the primary behavior of the gold surface amidst the various possible behaviors influenced by impurities. Specifically, we investigate how chloride and sulfate impurities in the perchlorate solution affect the double-layer structure and gold surface dynamics. Our findings reveal that the inconsistencies observed in pure perchlorate solution are very likely attributable to the presence of these minor impurities.

5

### 5.3 Experimental

#### 5.3.1 EC-STM measurements

Electrochemical Scanning Tunneling Microscope (EC-STM) images were obtained using a custom-built instrument developed at the Leiden Institute of Chemistry (LIC) at Leiden University. The EC-STM cell is constructed from PEEK. Detailed descriptions of the instrument's design and construction are provided in the Supporting Information of our recent paper[50]. Tips were crafted from a platinum/iridium wire (90/10) using the pulling-cutting method. To minimize extra faradaic current, a layer of hot melt adhesive (EVA-copolymer, synthetic resin, wax, and stabilizer, brand: C.K.) was applied, leaving the apex exposed. The working electrode (WE) was a disk-shaped single-crystal Au(111) electrode (10 mm diameter) with a gold wire welded at the

## 5.4. Experimental

---

back. This crystal, cut with 0.1° accuracy and polished to a 30 nm roughness by the Surface Preparation Laboratory (SPL) in the Netherlands, was annealed with a butane flame torch to an orange color for five minutes and then cooled in air above ultrapure water to prevent contamination. A high-purity gold wire served as the counter electrode (CE), and a reversible hydrogen electrode (RHE, Hydroflex, Gaskatel) was used as the reference electrode (RE). The distance between the WE and RE was approximately 7 mm to minimize the ohmic drop during the voltage sweep. Images were recorded in constant tunneling current mode with a current setpoint ranging from 50 pA to 150 pA. The tip bias ranges from 10 to 50 mV. To maximize the distance between the tip and the sample during CV application, the current setpoint was set to zero. The electrochemical voltage was then adjusted to the "rest potential," allowing the tip to approach as the current setpoint increased, resulting in the appearance of tunneling current. Throughout the experiment, the EC-STM chamber was purged with ultra-high-purity argon gas to reduce the risk of oxygen or other gas dissolution into the cell. All the experiments start with applying electrochemical potential of 0 V vs RHE, increasing the potential to the point of the lifting of the reconstruction, followed by applying the ORCs. In the course of the experiments, the lower potential windows varied from 0.9 V to 0.8 V to rule out the possibility of not reducing the oxidized surface and its effect on the observed results. Above 0.8 V, Au(111) should not reconstruct.[102]

### 5.3.2 Electrochemical Cell and Electrolyte

For standard electrochemical experiments, a custom-made Pyrex glass cell was employed. All glassware and plastic components were cleaned by soaking in a permanganate solution (0.5 M sulfuric acid and 1 g/L potassium permanganate) for at least 12 hours before each experiment. After thorough rinsing with Milli-Q water, the components were treated with a diluted piranha solution (3:1 mixture of sulfuric acid ( $\text{H}_2\text{SO}_4$ ) and hydrogen peroxide ( $\text{H}_2\text{O}_2$ ), diluted with water) to remove any manganese oxide and permanganate residues. To ensure all traces of the diluted piranha solution were eliminated, the parts were boiled at least five times. The electrolyte was prepared using ultra-high purity (UHP) Milli-Q water (resistivity  $> 18.2 \text{ M}\Omega\cdot\text{cm}$ ) and included  $\text{HClO}_4$  (70% Suprapur Sigma Aldrich),  $\text{H}_2\text{SO}_4$  (96% Suprapur Sigma Aldrich),  $\text{HCl}$  (30% Suprapur Sigma Aldrich), and ROTIPURAN® Ultra/Supra  $\text{HClO}_4$ . The solution was degassed with ultra-high-purity argon gas for at least 30 minutes before use. All measurements were conducted at room temperature (293 K).

## 5.4 Results and discussion

Many EC-STM experiments were conducted to investigate the morphological changes of a well-annealed Au (111) surface during oxidation-reduction cycles (ORCs) in a 0.1 M  $\text{HClO}_4$  solution. Three main surface responses were observed: roughening and nano-island formation (adatom and vacancy islands), etching (formation of vacancy islands), and a surface remaining intact. To assess the impact of chloride and sulfate contaminants, similar experiments were performed in 0.1 M  $\text{HClO}_4$  solutions containing 10  $\mu\text{M}$   $\text{H}_2\text{SO}_4$  and HCl.

### 5.4.1 Oxidation-reduction cycles of Au(111) in 0.1 M $\text{HClO}_4$

Figure 5.1a shows the changes in the cyclic voltammogram of Au(111) as a consequence of the ORCs in a conventional electrochemical cell containing 0.1 M  $\text{HClO}_4$  solution, scanning from 0.9 to 1.7 V at  $50 \text{ mVs}^{-1}$ . The first cycle can be used as a benchmark for the cleanliness and crystallographic orientation of the single crystal surfaces [103, 104]. The first CV just after annealing is shown separately, and agrees well with the existing literature, together with the final CV after 200 ORCs (Figure 5.1b). Au(111) shows a double-layer region up to 1.1 V, with negligible or very weak specific adsorption of perchlorate anions.[102] At higher potentials, the CV features two anodic peaks O3 and O4, respectively, at approximately 1.35 and 1.55 V. Angerstein-Kozlowska et al. have attributed these peaks to the replacement of adsorbed anions with hydroxide (O3) and further gold oxidation accompanied with some remaining anion desorption (O4) [105, 106]. Upon cycling two smaller shoulder-type peaks appear at potentials below the O3 peak called O1 and O2, likely related to OH and O adsorption on low-coordinated sites generated during the oxidation-reduction cycling. Simultaneously, the charge corresponding to the O3 and O4 peaks decreases with increasing number of cycles, indicating that the (111) terrace is lost during the process. In the negative-going scan, a prominent cathodic peak exists at 1.18 V, labeled as R3, associated with the reduction of the surface oxide [105, 106]. There is a shoulder to R3 at more negative potentials, which has been assigned to the reduction of two sublattices of MOH on an anion-free surface [105, 107]. With cycling, this shoulder develops two separate peaks, R1 and R2. Calculated oxidation and reduction charge densities for the 200 ORCs are available in Figure C.1a.

Figure 5.2 displays EC-STM images of the Au(111) surface in a 0.1 M  $\text{HClO}_4$  solution from the initial reconstructed surface to the roughened surface after 200 ORCs. In the double-layer region at 0.7 V (Figure 5.2a), the images reveal wide, atomically

## 5.4. Results and discussion

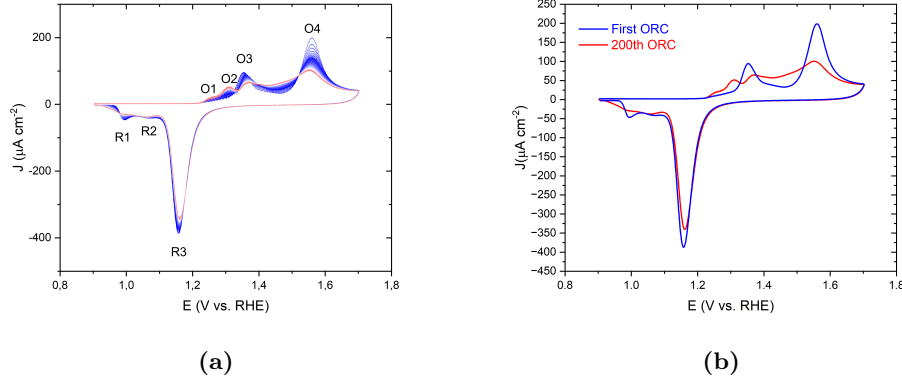


**Figure 5.1:** a) Cyclic voltammograms of the consecutively applied 200 ORCs on Au(111) in 0.1 M  $\text{HClO}_4$  with a scan rate of  $50 \text{ mVs}^{-1}$  in the potential window of 0.9 to 1.7 V versus RHE from the first (blue) to 200th (red) b) only the first (blue) and the 200th (red) ORC.

flat terraces, separated by steps with a monoatomic height of 0.23 nm (Figure C.2), consistent with the reported 0.236 nm monoatomic step height of the Au(111) surface [108, 97]. At 0.9 V (Figure 5.2b), small monoatomic islands begin to form on the terraces due to the lifting of surface reconstruction from  $(\sqrt{3} \times 22)$  to  $(1 \times 1)$ . Thus, lifting of the reconstruction can take place between 0.7 V and 0.9 V. Figure 5.2c, captured after fifteen ORCs from 0.9 to 1.65 V at a scan rate of  $50 \text{ mVs}^{-1}$ , with the potential held at 0.9 V during imaging, shows the Au(111) surface covered with atomic islands on the terraces caused by place exchange during the ORCs. An increase in surface roughness with increasing number of ORCs was previously observed by Ye et al. using in-situ EC-STM (Figure 2 in reference [96]). Although the majority of the surface was roughened, some areas stayed remarkably pristine, as illustrated by the darker areas in Fig.5.2c pointed with the blue arrow. Further imaging after applying ORCs for 15, 25, 40, 50, 110, 170, and 200 cycles (25 -170 in Figure C.3) reveals that the size of the islands increases with the number of cycles, as illustrated in the image Figure 5.2d obtained after 200 ORCs. As the roughness increases, the darker areas, which initially show no roughening, diminish in size and eventually disappear after approximately 50 cycles. The tendency of forming large islands was consistently observed across three different experiments, as illustrated in Figures C.4a after 200 cycles, C.4b and C.4c after 70 cycles. There are some inhomogeneities in the size of formed islands after the 200 ORCs, in contrast to the results in sulfuric acid [50]. This inhomogeneity interferes with the calculation of the height-height correlation function,

so that no meaningful correlation length and roughness calculation can be obtained.

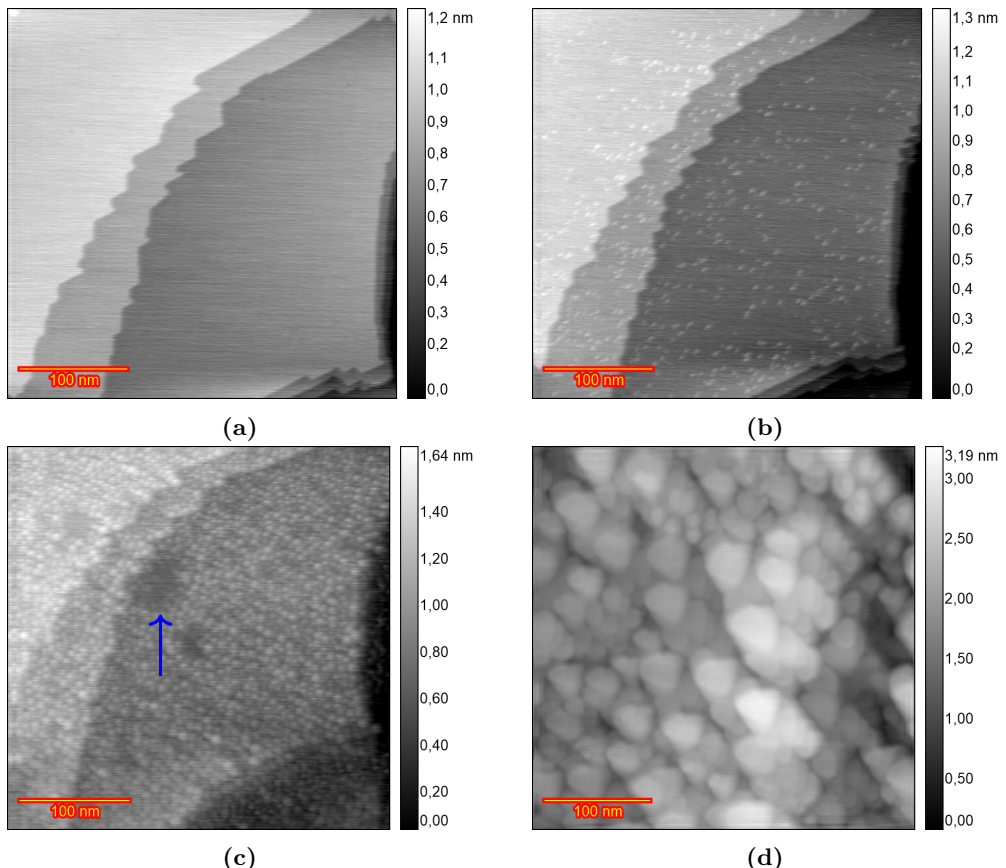


**Figure 5.2:** EC-STM image ( $350 \times 350 \text{ nm}$ ) of Au(111) in 0.1 M  $\text{HClO}_4$ . a) Sample surface at 0.7 V vs RHE just after annealing. b) partially lifted reconstruction at 0.9 V. c) after n ORCs from 0.9 to 1.65 V and imaging at 0.9 V n=15 d) n=200.

In multiple experiments, we observed that the surface structure of Au(111) in  $\text{HClO}_4$  solution varied across different experiments, especially after ORCs, as illustrated by the images of an experiment shown in Figure 5.3. The experiment of that figure was in principle the same as the experiment in Figure 5.2. In the double-layer region at 0.8 V (Figure 5.3a), the image shows broad, atomically flat terraces with a well-defined herringbone structure and a step lines of monoatomic step height. At 0.9 V (Figure 5.3b), small monatomic islands start to form on the terraces due to the lifting of the reconstruction. The surface of Au (111) was scanned from 0.9 to 1.65 V at a rate of  $50 \text{ mVs}^{-1}$ , with the potential held at 1.1 V during imaging. No-

## 5.4. Results and discussion

table, after 1, 5 (Figure C.6c and C.6d), and 13 (Figure 5.3c) cycles, the monatomic islands and step edges remained stable, with the surface largely unchanged except for a few larger islands ( $\sim 10$  nm in diameter). As a consequence of going through the oxidation-reduction process and place-exchange mechanism, formation of many adatom and vacancy islands was expected. However, the surface remained unaffected. This behavior was also observed in other experiments (Figure C.5a). Other experiments were also performed with the rest potential of 0.9 V prior to this experiment, leading to comparable results, indicating that the rest (or imaging) potential plays no role in this behavior.

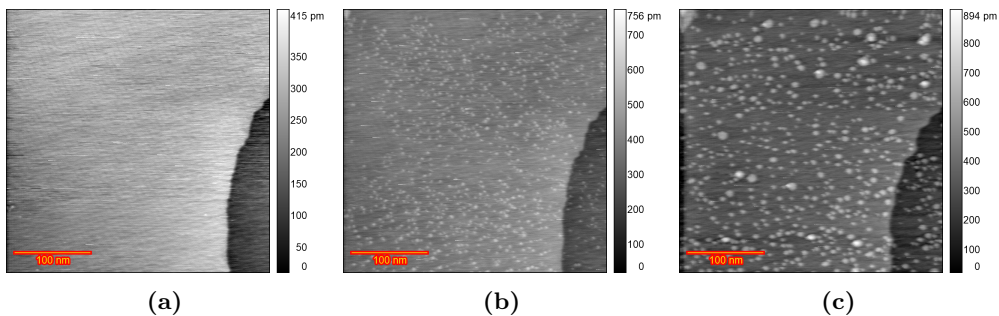


**Figure 5.3:** EC-STM image ( $350 \times 350$  nm) of Au(111) in 0.1 M HClO<sub>4</sub>. a) Sample surface at 0.8 V vs RHE just after annealing. b) partially lifted reconstruction at 0.9 V. c) after 13 ORCs from 0.9 to 1.65 V and imaging at 1.1 V.

Figure 5.4 illustrates another distinct behavior of the Au(111) surface structure in HClO<sub>4</sub> solution. Figure 5.4a shows the surface in the double-layer region at 0.8 V with reconstruction. The reconstruction is almost completely lifted at 0.95 V (Figure 5.4b) and leads to large adatom islands formation. These adatom islands are bigger than those observed in the experiments in Figures 5.2b and 5.3b. This indicates differences in the early stage of the experiment. After the initial scan from 0.9 to 1.65 V at  $50$  mV s<sup>-1</sup>, and imaging at 1.1 V, small adatom islands appeared on the terraces (Figure 5.4c). By the eighth cycle (Figure 5.4d), small vacancy islands began to grow, and the number of the adatom islands reduced. The large adatom islands disappeared by the 15th ORC (Figure 5.4e) and after 50 cycles, triangular pits formed (Figure 5.4f). Continued cycling leads to coalescence of the pits and etched terraces sequentially, as shown in Figures C.7j, and C.7k after 125 and 200 cycles.

To check for a possible role of impurities in the electrolytes used in previous experiments and verify the consistency of the results, we utilized *ROTIPURAN*® Ultra/Supra HClO<sub>4</sub> electrolyte, renowned for its exceptional purity, to ensure consistent

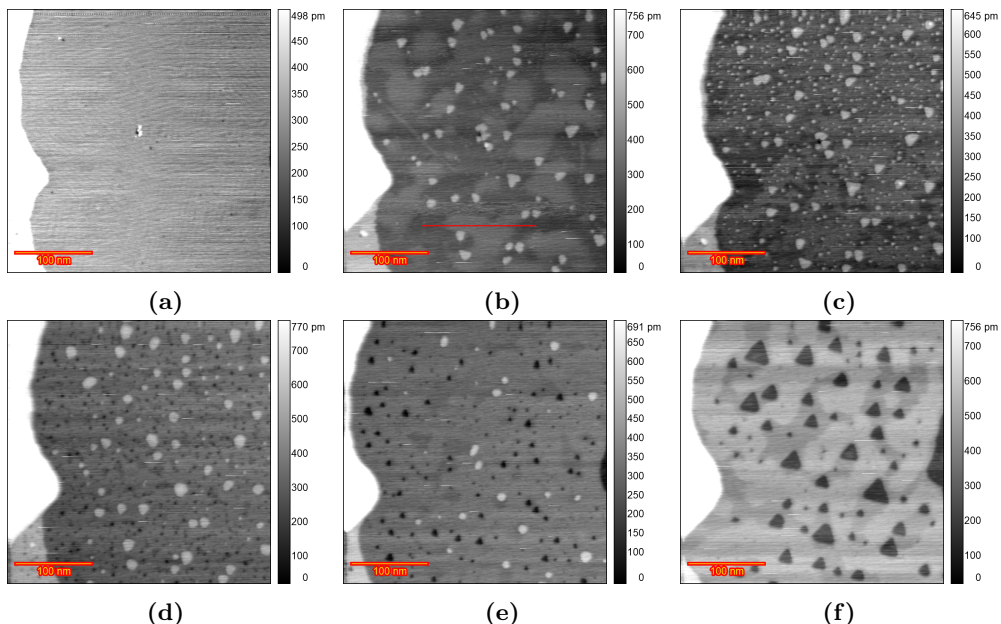


**Figure 5.4:** EC-STM image( $350 \times 350$  nm) of Au(111) in 0.1 M  $\text{HClO}_4$ . a) Sample surface at 0.8 V vs RHE just after annealing. b) lifted reconstruction at 0.95 V. c) after n ORCs from 0.9 to 1.65 V and imaging at 1.1 V n=1 d) n=8 e) n=15 f) n=50

outcomes. Figure 5.5 presents the results obtained using this electrolyte. At 0.6 V in the double-layer region (Figure 5.5a), the surface displayed broad, atomically flat terraces. After lifting the reconstruction, the terraces were partially covered by islands (Figure C.8b). These atomic islands grew in size and number by 2nd and 5th ORC (Figures C.8c, and C.8d). Although in the previous experiment, the vacancies began to grow after the eighth ORC, in this case, there is no significant growth of the vacancies after 20 ORCs (Figure C.8e). After 30 cycles, vacancies start to grow partially and the adatom islands disappeared (Figure C.8f). Ultimately, as shown in Figure 5.5b after 100 cycles, the terraces were strongly etched one by one as observed in Figure 5.4f. Higher cycle numbers up to 200 ORCs, caused more etching as shown in Figure C.8l. We suggest two possible explanations for the disappearance of the adislands and the formation of vacancies. The first possibility is that locally adsorbed contaminants, likely chloride, are moved by the scanning tip, altering the surface behavior by modifying the double-layer structure. The second possibility is that initially, the surface was free of impurities, allowing the growth of islands. However, after 20 ORCs impurities from the solution, again likely chloride, were absorbed onto the gold surface, reducing

## 5.4. Results and discussion

the built-up roughness and islands, and finally etching the surface. It is well known that perchloric acid may contain anionic impurities [70]. Therefore, we decided to perform experiments with small amounts of sulfate and chloride added deliberately to the perchloric acid electrolyte. In future research, spectroscopy techniques such as X-ray photoelectron spectroscopy (XPS) could be used to identify specific surface contaminants, although having the necessary spatial resolution will be a challenge. Moreover, higher-resolution scanning tunneling microscopy may lead to unraveling the double layer structure in the unchanged areas.

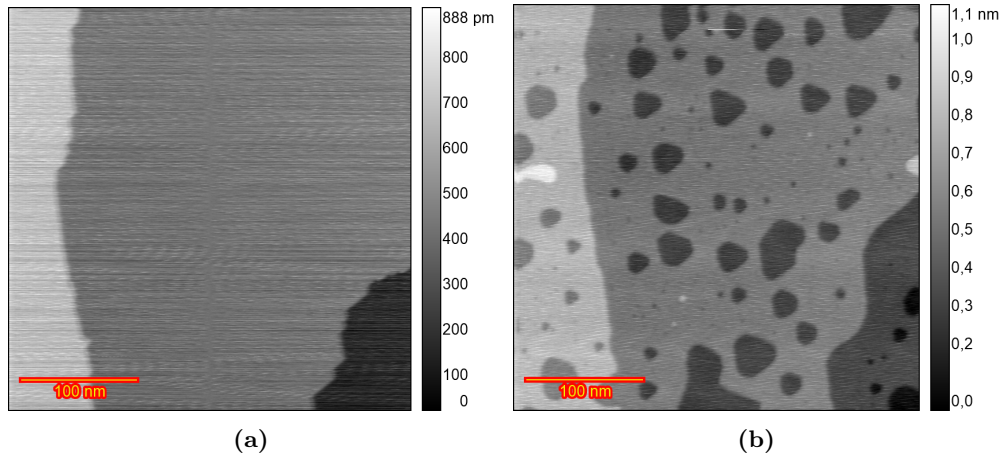


**Figure 5.5:** EC-STM image ( $350 \times 350$  nm) of Au(111) in 0.1 M  $\text{HClO}_4$  (ROTIPURAN). a) Sample surface at 0.6 V vs RHE just after annealing. b) after 100 ORCs from 0.9 to 1.65 V and imaging at 0.9 V.

### 5.4.2 Role of $\text{H}_2\text{SO}_4$ Contamination in $\text{HClO}_4$ solution on Au (111) Surface Structure

Since sulfate adsorbs more strongly than perchlorate, we added 10  $\mu\text{M}$   $\text{H}_2\text{SO}_4$  to 0.1 M  $\text{HClO}_4$  in the EC-STM experiment (Figure 5.6a) to examine its effect. In the double-layer region (0.0 V), wide atomically flat terraces, approximately straight and curved step lines were visible. Figure 5.6b displays an image acquired after 10 cycles of potential scanning from 0.8 to 1.65 V at a scan rate of  $50 \text{ mV s}^{-1}$ , with the potential of Au held at 0.8 V during imaging. This observation reveals that the Au(111) surface is completely covered with islands after oxidation and reduction, and the step edges remain pristine. Imaging after applying ORCs for 20, 35, 50, 75, 100, 125, 150, 175, (figures C.9d to C.9k) and 200 cycles (Figure 5.6c) shows an increase in surface

roughness. Scanning more than 23 different/random (Figure C.10) locations after 200 ORCs confirmed that the surface structure observed in Figure 5.6c is consistent across the scanned locations. The final texture and level of roughening of the Au electrode in the solution containing 10  $\mu\text{M}$   $\text{H}_2\text{SO}_4$  (Figure 5.6c) is similar to that observed in the experiment with pure sulfuric acid (Figures 3, and 5 in Ref[50]). A comparison with the pure  $\text{HClO}_4$  solution (Figure 5.2d) reveals that the size distribution of the islands is more uniform in the experiment with  $\text{H}_2\text{SO}_4$  in solution than in the pure  $\text{HClO}_4$  experiment. Figure C.11 shows the corresponding CVs of the 200 ORCs of the annealed Au (111) in a conventional electrochemical cell containing  $\text{HClO}_4$  solution + 10  $\mu\text{M}$   $\text{H}_2\text{SO}_4$ .

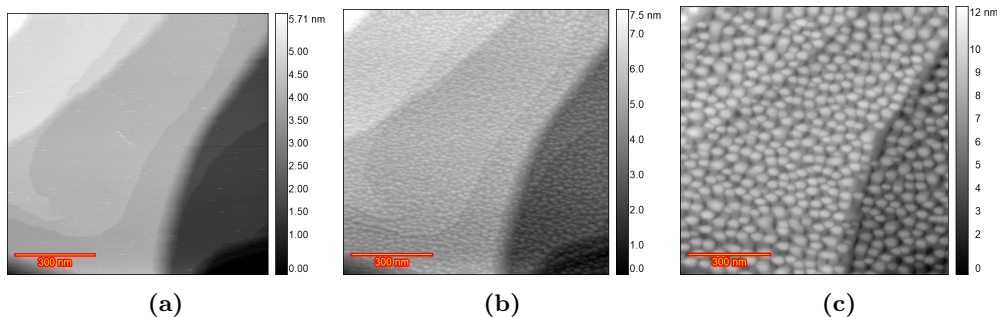


**Figure 5.6:** EC-STM image( $350 \times 350$  nm) of Au(111) in 0.1 M  $\text{HClO}_4$  containing 10  $\mu\text{M}$   $\text{H}_2\text{SO}_4$ . a) Sample surface at 0.0 V vs RHE just after annealing. b) after  $n=10$  ORCs from 0.8 to 1.65 V and imaging at 0.8 V C)  $n=200$

In another experiment, under in principle identical experimental conditions, regions with no roughening were observed. Similar to the experiment described in the previous paragraph, atomically flat terraces were seen at 0.0 V (Figure 5.7a). After 10 ORCs from 0.8 to 1.65 V at  $50 \text{ mVs}^{-1}$ , with holding the potential at 0.8 V during imaging (Figure 5.7b), the surface became completely covered with atomic islands. Imaging after 200 ORCs (Figure 5.7c) showed an increase in the size and height of the islands. However, the top part of the image showed larger islands in comparison to the rest of the image. Surprisingly, zooming out and imaging different locations after 200 ORCs (Figure 5.7d) revealed areas where no roughening had occurred. Since the step lines are clearly visible at the center of the image, the flat areas cannot be caused by improper surface imaging. This observation indicates that even in the presence of  $\text{H}_2\text{SO}_4$ , inhomogeneity in the surface roughening can still be observed after many ORCs. This is likely due to the presence of chloride impurities, which are absorbed more strongly onto the surface than  $\text{H}_2\text{SO}_4$ . As a result, the double layer is not homo-

## 5.4. Results and discussion

geneous across the entire sample surface, leading to variations in surface roughening. This phenomenon was also observed in our previous work[109], which examined the effect of small amounts of chloride in  $H_2SO_4$ . Figure C.12 shows the full sequence of experimental images corresponding to Figure 5.7.

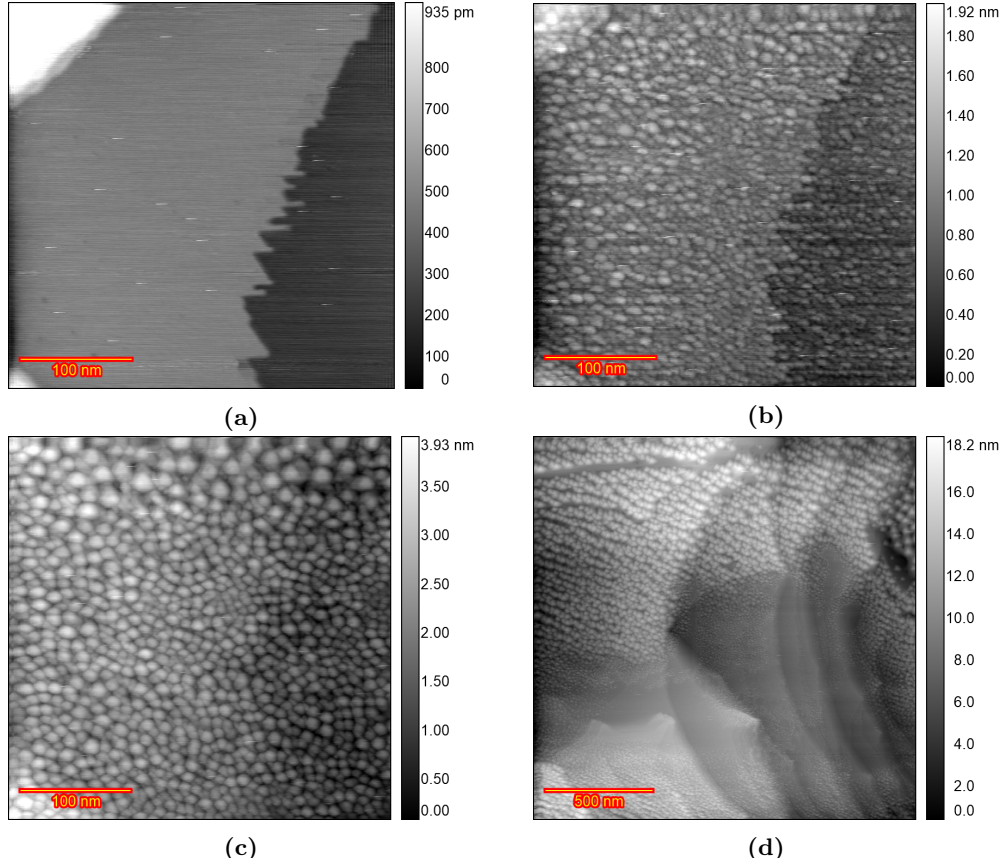


**Figure 5.7:** EC-STM image ( $350 \times 350$  nm) of Au(111) in  $0.1$  M  $HClO_4$  containing  $10$   $\mu$ M  $H_2SO_4$ . a) Sample surface at  $0.0$  V vs RHE just after annealing. b) after  $n=10$  ORCs from  $0.8$  to  $1.65$  V and imaging at  $0.8$  V c)  $n=200$  d) zoomed out.

### 5.4.3 Role of HCl Contamination in $HClO_4$ solution on Au (111) Surface Structure

Figure 5.8 shows EC-STM images of an Au(111) surface in a  $0.1$  M  $HClO_4$  solution with  $10$   $\mu$ M HCl at various stages during the ORC experiment. At  $0.0$  V (Figure

## Chapter 5. Anisotropic Roughening of Au(111) Single-Crystal Electrode Surface in $\text{HClO}_4$ Solution during Oxidation-Reduction Cycles

### 5

5.8a), wide and atomically flat terraces and monatomic step lines are visible. Figure 5.8b depicts an image taken at 0.9 V, after the lifting of the surface reconstruction. Significant changes in the shape of the step lines were observed compared to the chloride-free solution, although no adatom islands can be seen because of the high mobility of gold atoms in the presence of chloride. Figure 5.8c presents an image after 10 cycles of potential scanning from 0.8 to 1.65 V at a  $50 \text{ mVs}^{-1}$  scan rate, with the potential held at 0.8 V during imaging. Significant recession of the step lines is observed, with no vacancy islands, and the terraces remain pristine after 10 ORCs. Imaging after 200 ORCs (Figure 5.8d) shows significant etching and recession of the step lines. The complete sequence of images for this experiment (Figure 5.8) is presented in Figure C.13. We previously observed that in the presence of chloride in sulfuric acid[109], there is significant Au dissolution and the high mobility of gold surface atoms in chloride-containing electrolyte does not allow the capturing of the vacancies in the STM images. Scanning at various/random locations after 200 ORCs confirms that no adatom/vacancy islands can be seen on the scanned areas because of high mobility of gold atoms in the presence of chloride. This high dissolution rate in chloride-containing electrolytes was repeated in another experiment (Figure C.14).

Repetition of the same experiment (as showed in Figure 5.8) started with a well-defined herringbone reconstruction at 0 V (Figure 5.9a). Unlike the observations in the experiment described in the previous paragraph, some vacancy islands were captured during sample imaging. For instance, after 125 ORCs (Figure 5.9b) vacancies are located in the top part of the image. These observations can pinpoint the fact that the extent of chloride adsorption on the sample surface differs even with the additional 10  $\mu\text{M}$  HCl. More images for this experiment are provided in Figure C.15.

Figure 5.10a shows how the cyclic voltammetric fingerprint of Au(111) changes during cycling from 0.9 to 1.7 V at  $50 \text{ mVs}^{-1}$ . In the initial cycle of the chloride-containing solution (blue curves in Figure 5.10a), the peaks of OH adsorption and gold oxide formation merge into a single peak around 1.42 V (blue curve in Figure 5.10b). A previous EQCM study[91] attributed this anodic peak to the three-electron oxidative dissolution of gold  $\text{Au} + 4 \text{Cl}^- \longrightarrow \text{AuCl}_4^- + 3 \text{e}^-$ . Furthermore, as reported in the literature [97, 55], the reduction peak of the oxide layer shifts to a slightly more positive potential. In subsequent oxidation-reduction cycles, the charge of the peak due to the formation of  $\text{AuCl}_4^-$  decreases, and completely disappears after approximately 15 cycles (Figure 5.10a ), likely due to the decreasing presence of chloride on the surface promoting  $\text{AuCl}_4^-$  formation. Moreover, after 200 cycles, the peak for gold oxide formation (O4) broadens, as shown in Figure 5.10c. Calculated oxidation reduction

## 5.4. Results and discussion

---

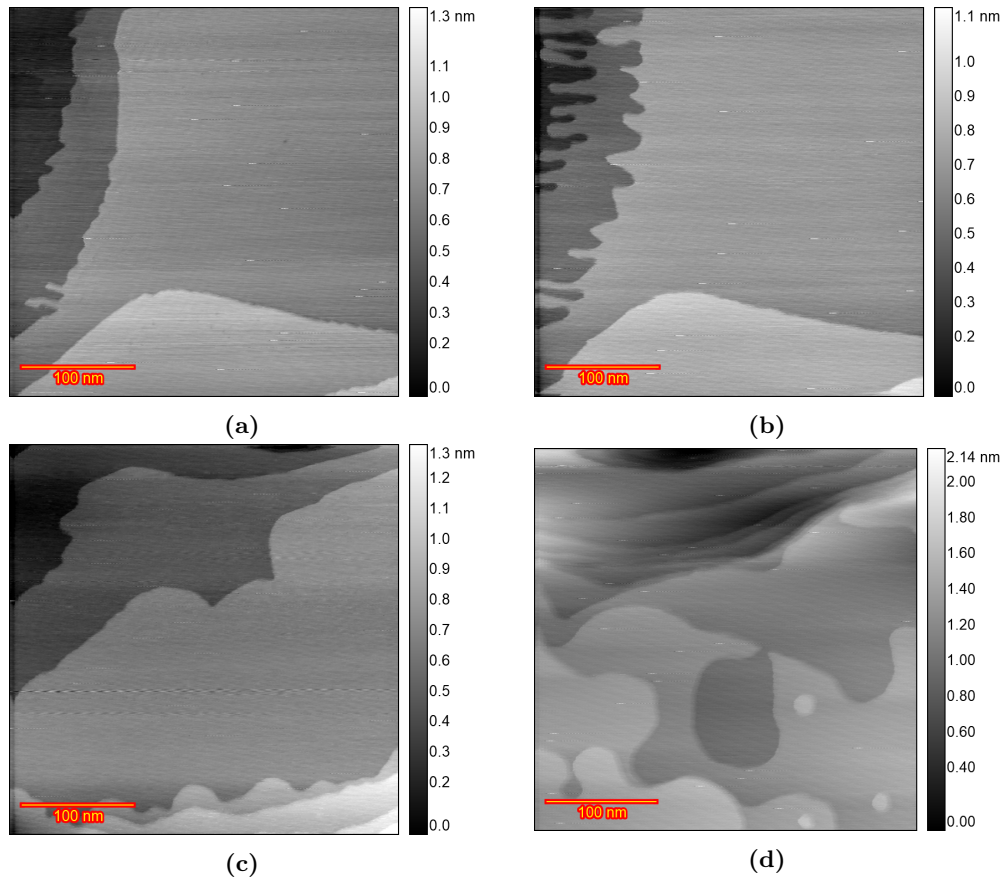


**Figure 5.8:** EC-STM image ( $350 \times 350$  nm) of Au(111) in 0.1 M  $\text{HClO}_4$  containing  $10 \mu\text{M}$  HCl. a) Sample surface at 0.0 V vs RHE just after annealing. b) lifted reconstruction at 0.9 V. c) after  $n=10$  ORCs from 0.8 to 1.65 V and imaging at 0.8 V d)  $n=200$

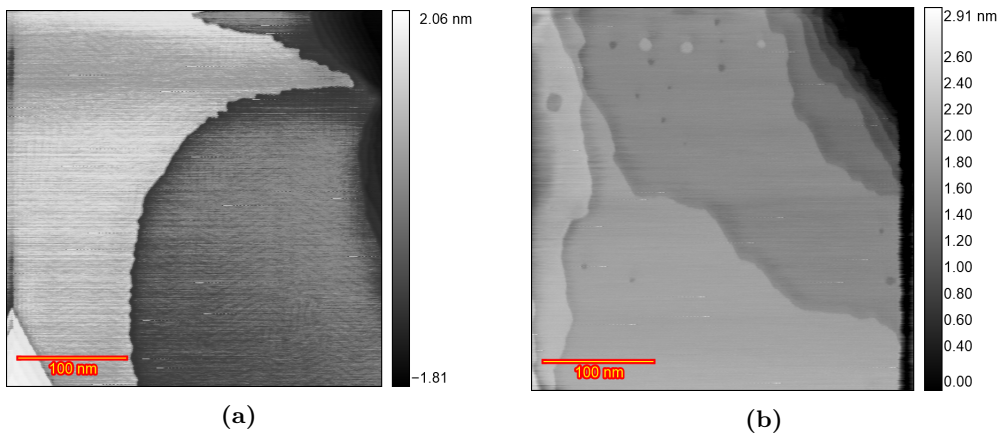


**Figure 5.9:** EC-STM image ( $350 \times 350 \text{ nm}$ ) of Au(111) in  $0.1 \text{ M HClO}_4$  containing  $10 \text{ }\mu\text{M HCl}$ . a) Sample surface at  $0.0 \text{ V}$  vs RHE just after annealing. b) after  $n=125$  ORCs from  $0.8$  to  $1.65 \text{ V}$  and imaging at  $0.8 \text{ V}$ .

charge densities for these CVs are available in Figure C.16a.

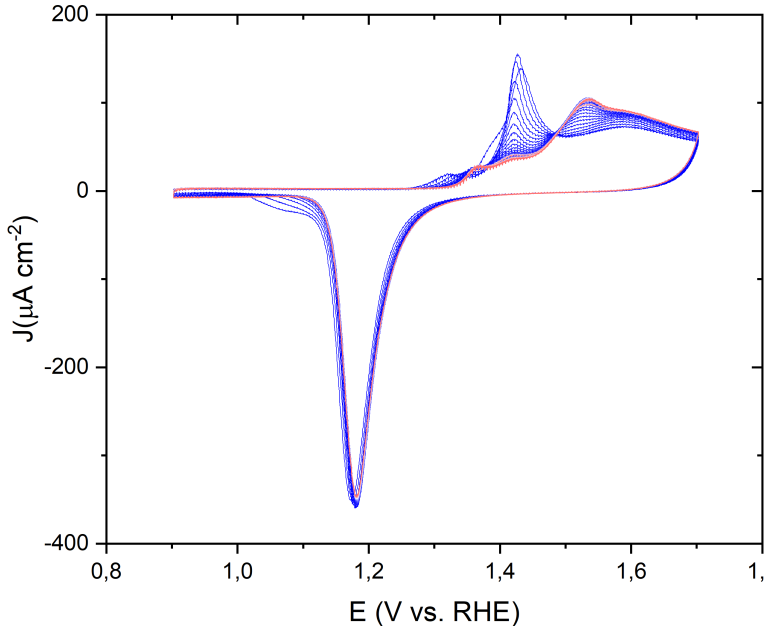
#### 5.4.4 General Discussion

The EC-STM studies described above demonstrate three primary surface responses of the Au(111) electrode in  $0.1 \text{ M HClO}_4$  solution during ORCs: roughening (formation of adatom and vacancy islands), etching (formation of pits), and surface stability (i.e. the surface remaining largely intact). Our findings demonstrate that the variation in these behaviors must be attributed to trace impurities, most likely chloride.

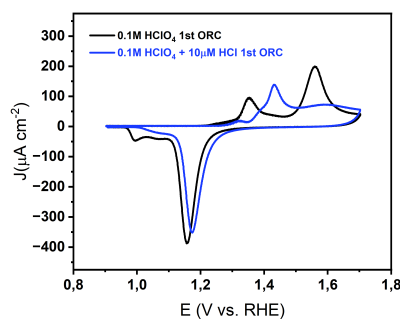
*Roughening by Island Formation.* The formation of adatom islands and vacancy islands is indicative of surface roughening, which can be observed in both  $\text{HClO}_4$  and  $\text{H}_2\text{SO}_4$  solution by applying ORCs. This structure is attributed to the place-exchange process that occurs during ORCs, which causes surface atoms to be displaced and rearranged, leading to an increase in surface roughness[42]. The addition of sulfate impurities to the  $\text{HClO}_4$  solution, being more adsorptive than perchlorate, tends to occupy sites on the surface, as evidenced by changes in cyclic voltammetry peaks in Figure C.11. This apparently leads to a more homogeneous surface roughening, as is evident in Figure 5.6 where the presence of  $10 \text{ }\mu\text{M H}_2\text{SO}_4$  results in more uniform island sizes and a consistent increase in surface roughness.

*Etching and Pit Formation.* Contrasting with the roughening behavior, etching is characterized by the formation of pits on the Au(111) surface. The pits begin to

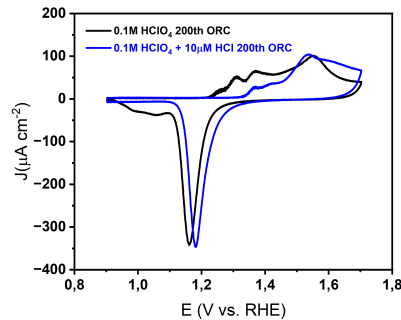
## 5.4. Results and discussion



(a)



(b)



(c)

**Figure 5.10:** CV of Au(111) in 0.1 M HClO<sub>4</sub> containing 10 μM HCl in the potential window of 0.9 to 1.7 V versus RHE a) All the CVs from the first (red) to 200th (blue) b) comparison of the first CV of pure 0.1 M HClO<sub>4</sub> (black) and the electrolyte containing 10 μM HCl (blue). c) comparison of the 200th CV of pure 0.1 M HClO<sub>4</sub> (black) and the electrolyte containing 10 μM HCl (blue).

## Chapter 5. Anisotropic Roughening of Au(111) Single-Crystal Electrode Surface in $\text{HClO}_4$ Solution during Oxidation-Reduction Cycles

form and coalesce into larger ones, as shown in Figures 5.4 and 5.5. It is known that 10  $\mu\text{M}$  HCl in 0.1 M sulfuric acid can cause a slow ( 2 atomic layer over 200 ORCs) gold dissolution, and increasing the chloride concentration leads to increase in dissolution rate and gold atom surface mobility[109]. Chloride ions are known to strongly adsorb on Au(111), forming a chloride adlayer that can cause gold dissolution through the formation of gold chloride complexes (e.g.,  $\text{AuCl}_4^-$ ). This trace level of chloride impurities in perchloric acid appears to lead to strong differences in local chloride absorption, and causes gold roughening the extent of which can vary widely over the surface.

*Intact surface.* In some cases, the Au(111) surface remains relatively stable, with minimal roughening or etching observed. A similar behavior as depicted in Figure 5.3 was observed in our previous study, in which a very low chloride concentration (1  $\mu\text{M}$  HCl) in 0.1 M sulfuric acid could apparently form an adlayer which blocks surface oxidation-reduction reactions in that area and consequently, no change in surface structure or surface roughening was observed even after 200 ORCs[109]. Thus, the very low concentration of chloride can be related to the intactness of the surface over many ORCs. Moreover, the areas that stayed unchanged over ORCs in 0.1 M  $\text{HClO}_4$  are easier to find compared to the experiment with the additional 10  $\mu\text{M}$  sulfuric acid. This indicates that there is a competition between the anions to cover the surface and this may reduce the intact areas in the presence of sulfate.

The observed height changes on the terraces in Figures 5.4b and 5.4f can be explained by the localized adsorption of impurities (most likely chloride) on the surface. At sufficiently high potentials (around 0.9 V vs RHE in this case), anion adsorption occurs, leading to the lifting of reconstruction. This adsorption can modify the tunneling medium, which in turn can affect the work function. Such changes can alter the magnitude of the tunneling current. Since all images are captured in constant current mode, the feedback system compensates for this change by adjusting the tip height. Consequently, variations in the work function may appear as depressions/protrusion on the surface. Similarly, shadow-like regions on the terraces, as seen in Figures 5.4b and 5.4f, were noted to have heights lower than an atomic step ( 0.87  $\text{\AA}$  according to height profile plot in Figure 5.11.) with indistinct boundaries. Thus, these height variations do not represent actual topographical features of the sample.

Similar behavior was observed for 1  $\mu\text{M}$  HCl in 0.1 M sulfuric acid[109]. The impact of the change in the adlayer on the topographical image of Cu(111) in 0.1 M NaOH was observed as a reduced height on the terrace as well (approximately 0.05 nm)[110]. This observation provides some more evidence that the double-layer composition at

## 5.5. Conclusions

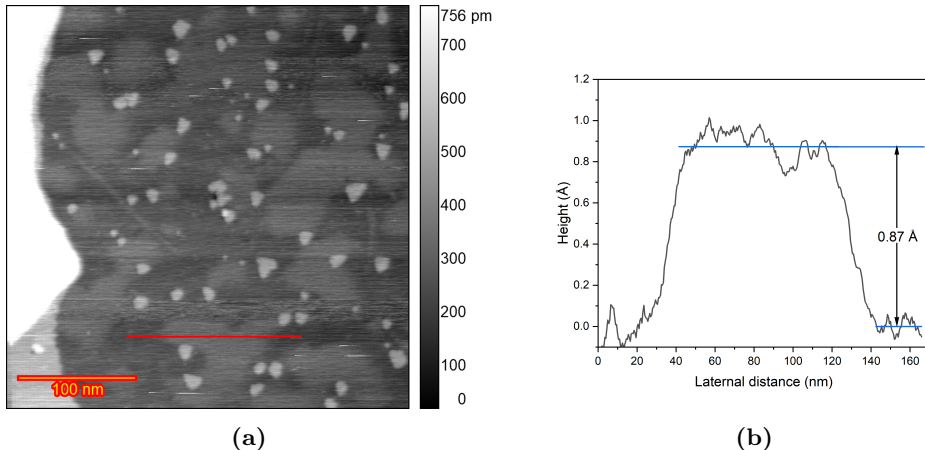


**Figure 5.11:** a) The STM image showed in Figure 5.4b with the red line indicating the location of the extracted height profile b) the corresponding height profile showing the height difference of higher and lower area on the same terrace.

high enough potentials can be/become inhomogeneous. The observations in figure 5.5 suggest that the absorbed layer is not static and can change during the experiment, likely due to interactions with the scanning tip and/or the diffusion of contaminants in the electrolyte solution. Comparison of Figure 5.8 and 5.9b would show some variations in chloride concentration since previous in-situ STM studies of Au(111) have shown that the presence of  $\text{Cl}^-$  ions significantly enhances surface diffusion and accelerates annealing on Au (111)[95, 55, 97]. A similar inhomogeneity in the double layer composition was also observed in 0.1 M sulfuric acid plus 1  $\mu\text{M}$  HCl in our previous study[109].

## 5.5 Conclusions

This study underscores the significant impact of trace impurities on the electrochemical behavior and surface morphology of Au(111) in  $\text{HClO}_4$  solutions, highlighting their role in dictating anisotropic surface evolution. The adsorption of impurities, such as chloride, alters the local electrochemical environment, influencing the surface oxidation and reduction reactions. These findings emphasize the complexity of the electrochemical double-layer structure and the need to consider impurity effects in both fundamental and applied research involving gold electrodes. Understanding these mechanisms is crucial for addressing degradation in noble metals like gold, particu-

## **Chapter 5. Anisotropic Roughening of Au(111) Single-Crystal Electrode Surface in HClO<sub>4</sub> Solution during Oxidation-Reduction Cycles**

---

larly in environments where maintaining ultrapure conditions is challenging. Further research is essential to elucidate the mechanistic pathways of surface changes and to develop strategies for mitigating impurity-induced degradation, thereby improving the performance and longevity of gold-based electrochemical systems.

## **5.6. Acknowledgement**

---

### **5.6 Acknowledgement**

This work was funded by the TOP grant project number 716.017.001, financed by the Dutch Research Council (NWO)

# Appendix A

## Supporting information for chapter 2

### A.1 Introduction

As explained in the introduction of this thesis, EC-STM is one of the instruments that can help chemists to have a closer look at the surface of electrodes. Many improvements have been made[111, 112] since the first successful experiments of atomic resolution in aqueous electrolytes[113]. However, there are always some limitations in these instruments that prevent us from recording valid data in certain measurements. For instance, the electrolyte inside the cell is not renewed with fresh electrolyte. This can be problematic for long measurements of e.g. the hydrogen evolution reaction (HER) or the oxygen evolution reaction (OER). The concentrations of species can alter in the electrolyte, and impurities can accumulate on the electrode surface, which is not desirable. One way to tackle this is to have a flow of electrolytes inside the cell. Thus, a pumping system is required to pump the fresh electrolyte into the cell and pump out the used electrolyte. Because of the small volume of the EC-STM cell, it is essential to have precise control over the flow rates at the inlet and outlet. The errors in pumping rates can result in overflow or underflow conditions. Moreover, the surface tension plays a significant role because of the small size of the cell. At this dimension, the dominant force is not gravity anymore, and we must take surface tension into consideration. Finally, the flow can make some minor pressure differences across the tip and exert some lateral forces toward the tip during the image recording,

## A.2. Numerical Model (FLOW-3D)

---

which can turn into a reason for extra drifts. The electrolyte flow near the sample surface is crucial because it can affect the electrochemical reactions on the surface. A proper flow near the sample surface is required, and the best way to study this characteristic is computational fluid dynamics (CFD). CFD is a numerical method for the simulation of fluid flow in a system. The Residence Time Distribution (RTD) in a reactor can also be calculated by this method. The RTD is an efficient tool to study the flow pattern like flow mixing behavior in chemical reactors[114]. In a nutshell, the time that different fluid elements spend in a continuous process unit (or steady-state continuous flow reactor) is called residence time distribution (RTD) of the fluid elements in that process unit (reactor). The RTD in a reactor is determined experimentally by injection of an inert tracer into the stream flowing through the reactor at time  $t = 0$  in the reactor inlet and then measuring the concentration of the tracer over time in the reactor outlet. The response concentration curve, known as the RTD function, provides useful information about the process stream dynamics[115]. A critical consideration in the system's design is the prevention of vortex formation within the cell, as this phenomenon can drastically alter the average residence time distribution, thereby impairing overall performance. To address this issue, an extensive study was undertaken to evaluate the effects of cell geometry and dimensions. In addition, the influence of operational parameters, such as the pumping rate and the electrolyte height, was investigated. The results of these analyses will be presented and discussed in the following sections.

## A.2 Numerical Model (FLOW-3D)

Simulation of flow in the cell was performed by FLOW-3D Software[116] within a two-phase system (water-air) in a three-dimensional numerical model. In FLOW-3D, all equations are formulated with area and volume porosity functions. This method is called FAVOR or Fractional Area/Volume Obstacle Representation Method[116]. In the FAVOR method, the meshes are rectangular, and boundaries are located in the mesh domain by using a porosity technique in which the volume fraction ( $V_F$ ) is zero within obstacles and unity where the cell is fully filled with fluid. For  $0 < V_F < 1$ , the cell is partially occupied by the obstacle (e.g., near the surface). By this technique, many numerical problems in a simulation, such as instability and algorithm complication can be eliminated. FLOW-3D solves the Reynolds averaged Navier-Stokes equations (continuity and momentum in the three directions) as shown in equations A.1-A.4, respectively[116].  $V_F$  is the cell fractional volume;  $\rho$  is the fluid density;  $u$ ,  $v$ ,

## Appendix A. Supporting information for chapter 2

---

and  $w$  are velocity components in the  $x$ ,  $y$ , and  $z$  directions;  $A_x$ ,  $A_y$ , and  $A_z$  are the cross-sectional area of the flow in  $x$ ,  $y$ , and  $z$  directions;  $p$  is pressure;  $G_x$ ,  $G_y$ , and  $G_z$  are gravitational components in three directions; and  $F_x$ ,  $F_y$ , and  $F_z$  are viscous accelerations in three directions.

$$V_F \frac{\partial \rho}{\partial t} + \frac{\partial(uA_x)}{\partial x} + \frac{\partial(vA_y)}{\partial y} + \frac{\partial(wA_z)}{\partial z} = 0 \quad (\text{A.1})$$

$$\frac{\partial u}{\partial t} + \frac{1}{V_F} \left[ uA_x \frac{\partial u}{\partial x} + vA_y \frac{\partial u}{\partial y} + wA_z \frac{\partial u}{\partial z} \right] = -\frac{1}{\rho} \frac{\partial p}{\partial x} + G_x + F_x \quad (\text{A.2})$$

$$\frac{\partial v}{\partial t} + \frac{1}{V_F} \left[ uA_x \frac{\partial v}{\partial x} + vA_y \frac{\partial v}{\partial y} + wA_z \frac{\partial v}{\partial z} \right] = -\frac{1}{\rho} \frac{\partial p}{\partial y} + G_y + F_y \quad (\text{A.3})$$

$$\frac{\partial w}{\partial t} + \frac{1}{V_F} \left[ uA_x \frac{\partial w}{\partial x} + vA_y \frac{\partial w}{\partial y} + wA_z \frac{\partial w}{\partial z} \right] = -\frac{1}{\rho} \frac{\partial p}{\partial z} + G_z + F_z \quad (\text{A.4})$$

In FLOW-3D Software, the VOF method is used for free surface tracking. That is a simple and efficient method for modeling free surface profiles in two-dimensional and three-dimensional meshes and is based on the work of Nichols and Hirt[117]. This method is an extended formulation of a previous method named Marker and Cell (MAC) method. In the MAC method, a number of marker particles are defined that moves in the computational domain, so the grids that contain markers are occupied by fluid, and those without markers are empty and free surface is located in grids that contain marker particles and at the same time have at least one neighboring grid cell that is empty[118]. MAC is a computationally expensive method compared to VOF because the new method does not need to define particles, and occupancy of the cells in the grid is parameterized using a function named  $F$ .  $F$  is a function that has a value of unity in regions occupied by fluid and zero in regions containing no fluid. So for  $F$  between 0 and 1, cells contain a free surface. The VOF formulation in the form of FAVOR is given as equation A.5.

$$\frac{\partial F}{\partial t} + \frac{1}{V_F} \left[ \frac{\partial}{\partial x} (FA_x u) + \frac{\partial}{\partial y} (FA_y v) + \frac{\partial}{\partial z} (FA_z w) \right] = 0 \quad (\text{A.5})$$

To investigate the residence time distribution (RTD) of the cell, two distinct approaches can be employed: particle tracking and the Local Mean Age (LMA) of the fluid. In the particle tracking approach, the RTD is determined by simulating the injection of particles at the reactor's inlet and measuring their concentration at the outlet. This method is called “pulse experiment” and the experimental process for

## A.2. Numerical Model (FLOW-3D)

---

this is described by Levenspiel (1999)[119]. In CFD, a convection-diffusion equation is employed to track the motion of a finite number of marker particles injected at the inlet boundary of the computational domain]. These marker particles are massless and significantly smaller than the mesh size within the domain. They do not influence the fluid dynamics but instead move with the mean flow while also undergoing diffusion, governed by a specified diffusion coefficient. From the resulting concentration curve ( $C(t)$ ), which is the particle concentration at a certain location as a function of time, the normalized concentration ( $E(t)$ ) can be calculated by equation A.6. The mean residence time ( $\tau$ ) is then defined as equation A.7. The dimensionless variance ( $\sigma$ ) in equation A.8 is a metric used to quantify the spread or dispersion of residence times in a system relative to the mean residence time. A low value of the dimensionless variance typically indicates a plug flow behavior with minimal dispersion whereas a high value suggests significant dispersion, often associated with mixing or deviations from ideal plug flow.

$$E(t) = \frac{C(t)}{\int_0^\infty C(t) dt} \quad (\text{A.6})$$

$$\tau = \int_0^\infty t E(t) dt \quad (\text{A.7})$$

$$\sigma^2 = \frac{\int_0^\infty (t - \tau)^2 C(t) dt}{\int_0^\infty C(t) dt} \quad (\text{A.8})$$

In the second approach which named local mean age (LMA), the average age of the fluid throughout the entire cell can be calculated. This represents the average time taken by fluid particles to travel from an inlet (or a reference point) to a specific location in the domain. The resulting distribution of the local average fluid age is visualized as iso-contours within the spatial domain.

### A.2.1 Geometry and Mesh

The geometry under CFD study consists of three key components in the region of interest: counter electrode, cell, and scanning tip. These components influence the flow patterns within the domain and subsequently affect the conditions for electrochemical reactions. The components, as shown in Figure A.1, are described below:

*The Cell* serves as the main container into which fresh solution is pumped through a 0.6 mm diameter inlet located on the left-hand side wall. The stale solution exits

through a 0.6 mm diameter outlet on the right-hand side wall at the same height as the inlet. At the bottom of the cell, a 3 mm diameter hole accommodates the sample, mounted underneath the cell. To prevent leakage, an O-ring, 1 mm thick, is placed between the sample and the cell. The most critical area of the cell is the bottom of this hole, where the electrochemical reactions occur.

*The Counter electrode* consists of a long, inert wire, typically made of platinum or gold. Since the wire is immersed in the solution, it can influence the flow within the cell. Therefore, the shape and placement of the electrode are critical. As shown in Figure A.1, the counter electrode is positioned near the edge of the wall at the bottom of the cell.

*The Scanning tip* is responsible for scanning the surface of the sample at the bottom of the cell and recording geometrical data with atomic resolution. The tip is a conductive wire oriented perpendicularly to the sample surface. Its effect on the flow pattern is significant and cannot be ignored. The tip is surrounded by an insulating layer to prevent unwanted electrochemical reactions along its length. Only the metal apex of the tip is exposed to the solution to record the tunneling current. However, the exposed area is negligible compared to the mesh size, and its impact on the overall flow pattern is minimal.

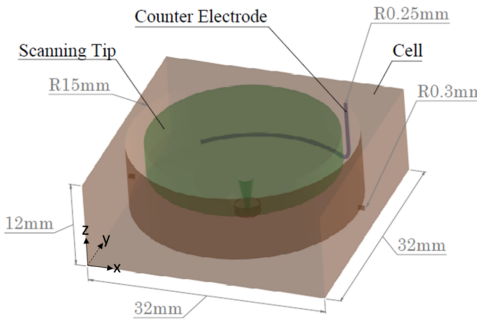


**Figure A.1:** Circular cell geometry showing the dimensions and the different components.

The system for CFD simulations consists of two primary regions: the flow domain and the solid domain. As previously mentioned, the flow domain is divided using rectangular meshes. This type of mesh is straightforward to generate and contributes to the stability of the numerical solution. The mesh size was selected to be less than 0.2 mm, which provides an appropriate balance between achieving a reasonable number of nodes and maintaining a manageable simulation runtime.

#### A.2.2 Boundary conditions

In this study, a two-phase flow was considered, with water as the first phase and air as the second. The flow was modeled under the assumptions of an isothermal, incompressible, Newtonian fluid with constant density and viscosity. The density and viscosity of water at room temperature were assumed to be  $998 \text{ kg.m}^{-3}$  and  $1 \text{ g.m}^{-1.s}^{-1}$ , respectively. The ambient air pressure was set to  $1.013 \times 10^5 \text{ Pa}$ . Constant velocity boundary conditions were applied at the inlet and outlet of the cell, while no-slip conditions were enforced at all solid walls. The Reynolds number was calculated to be 54 in the inlet/outlet pipe and lower throughout the cell, indicating laminar flow. The effects of surface tension and gravity were also considered. Gravity can be neglected in the simulation if the dimension of the cell is smaller than the capillary length of water ( $l_{\text{cap}} \approx 2.7 \text{ mm}$ )[120]. The surface tension of water at room temperature was considered constant at  $0.072 \text{ N.m}^{-1}$ . The effects of wall adhesion were included, with contact angles of  $80^\circ$  for the cell,  $115^\circ$  for the scanning tip, and  $40^\circ$  for the counter electrode.

The simulation was conducted with a time-step ranging from 1 to  $10 \mu\text{s}$ . The governing equations were solved until the velocity field reached a steady-state condition. The dye tracer was introduced at the cell inlet from  $t = 0 \text{ s}$  to  $t = 2 \text{ s}$ . For  $t > 2 \text{ s}$ , the tracer concentration at the inlet was set to zero. Simultaneously, the tracer concentration was detected at the outlet. Two flux planes were defined perpendicular to the inlet and outlet. The tracer concentration values were extracted from the simulation outputs corresponding to these planes.

Boundary conditions were applied as follows:

- $X_{\text{min}}$  and  $X_{\text{max}}$  : Constant velocity at the inlet and outlet.
- $Z_{\text{max}}$ : Constant pressure.
- $Y_{\text{min}}$ ,  $Y_{\text{max}}$ , and  $Z_{\text{min}}$ : Wall boundary conditions, as these planes correspond to solid materials.

A non-zero initial fluid height was considered to reduce the total runtime. To avoid any confusion, the initial height is defined the distance between the sample surface and fluid height.

### A.3 Results and discussion

In addition to the main circular cell (Figure A.1), the Rhombic Cell (Figure A.2a) was designed to minimize undesirable hydraulic flow patterns, such as back mixing and dead volume, thereby improving the overall mean residence time distribution (RTD) within the cell and near the sample surface. The Rhombic Cell with Groove (Figure A.2b) retains the general shape of the simple Rhombic Cell but includes a groove at its base to improve the performance further.

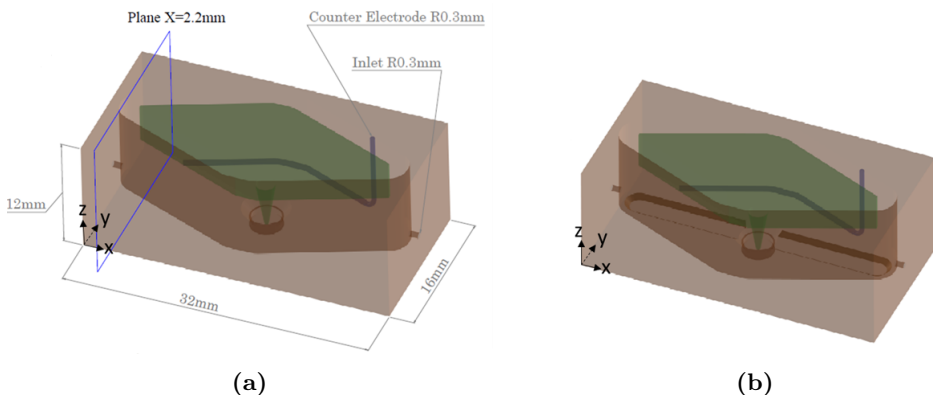


**Figure A.2:** a) rhombic cell, b) rhombic cell with groove

The results of the normalized concentration for the initial water height of 1mm with three different inlet velocities (3, 6, and 9 cm/s) for the circular cell are presented in Figure A.3. It is evident that the higher velocity helps the tracers to reach the detector at the output sooner and it shifts the highest concentration peak to lower time.

Figure A.4 presents the LMA contours in the midplane ( $y = 0$ ) for three different velocities. Similarly, Figure A.5 illustrates the LMA contours for a plane parallel to and close to the sample surface in the circular cell, with an initial water height of 1 mm and varying inlet velocities. These contours demonstrate the impact of higher velocities on RTD.

Similar simulations were done for the rhombic cell and Figure A.6 presents the normalized concentration function for different initial water heights and inlet velocities. As previously discussed, higher velocities result in improved performance, which is also evident for the Rhombic Cell. A comparison at a fixed velocity ( $3 \text{ cm.s}^{-1}$ ) across all initial electrolyte heights in Figure A.6 indicates that lower electrolyte heights lead to better RTD performance.

Figure A.7 presents the LMA results for a plane parallel to and near the sample

### A.3. Results and discussion

---

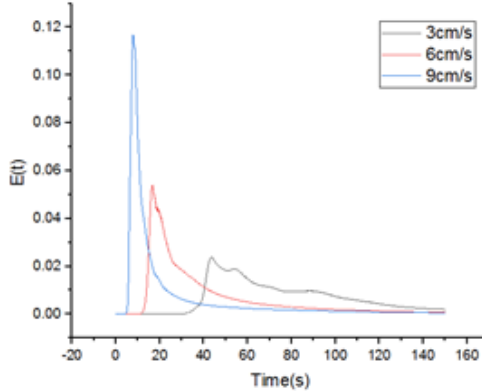


**Figure A.3:**  $E(t)$  function for 1 mm initial fluid height in the Circular Cell for three different inlet velocities

surface in the Rhombic Cell, with an initial water height of 1 mm and varying inlet velocities. A significant improvement is observed compared to the Circular Cell (Figure A.5).

The final version of the cell design is the Rhombic Cell with a groove at its bottom. Figure A.8 presents the  $E(t)$  function results for various initial electrolyte levels and inlet velocities for this model, while Figure A.9 displays the LMA contours.

When fluid flows through an ideal reactor, one of two primary assumptions is typically used to facilitate performance analysis. The first assumption is that the fluid in the reactor is thoroughly mixed, resulting in uniform properties throughout the reactor volume. This scenario applies to stirred reactors or blending systems. The second assumption, referred to as “plug flow,” suggests that all fluid elements enter the reactor simultaneously, travel through it at the same velocity along parallel paths, and exit at the same time. This assumption is particularly valid in cases such as laminar flow within pipes[121]. Thus, ideal reactors exhibit two primary flow patterns: plug flow and mixed flow. These patterns result in distinctly different behaviors, and reactor design often aims to approach one of these idealized flow regimes. However, real reactors deviate from these ideal patterns due to phenomena such as fluid channeling, recycling, or the presence of stagnant or dead zones within the reactor. Such flow irregularities should be minimized, as they reduce reactor performance[119]. Various models have been developed to predict reactor behavior under real conditions, capturing flows that may align more closely with plug flow, mixed flow, or intermediate patterns. By comparing experimental residence time distribution (RTD) curves to theoretical models, the most suitable model for a given reactor can often be identified. Although the fit

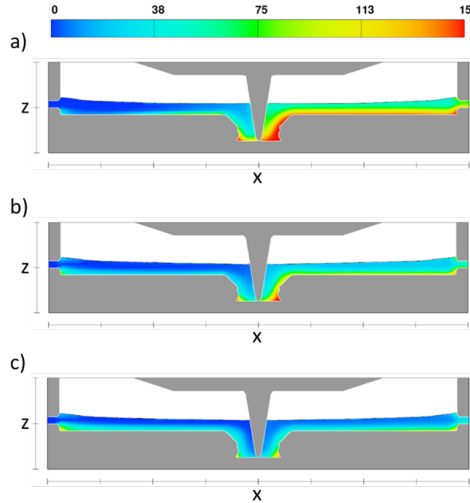


**Figure A.4:** LMA contour of circular cell in the midplane ( $y=0$ ) at velocities of a) 3, b) 6, and c)  $9 \text{ cm.s}^{-1}$ .

may not be perfect, these models provide a reasonable approximation of the actual  $E(t)$  curve[119]. In summary, these models are valuable tools for understanding flow behavior and diagnosing inadequacies in real reactors[119].

In compartment models, the reactor volume is divided into three distinct regions: the plug flow region, the mixed flow region (together referred to as the active volume), and the dead or stagnant region[119]. The  $E(t)$  function for a complete plug flow in a reactor resembles a pulse function, where all injected elements have the same residence time within the reactor. Under real conditions, when the  $E(t)$  function shows a sharp peak with a short tail, the flow can be approximated as a plug flow. In contrast, for a complete mixing flow, the  $E(t)$  function follows a decaying exponential curve over time. However, in real reactors, flow behavior is typically a combination of plug flow and mixing flow, resulting in an  $E(t)$  function that includes a sharp peak followed by a tail[119].

A comparison of the circular cell (Figure A.3) with the rhombic cell (Figure A.6b) demonstrates that the rhombic cell exhibits behavior closer to plug flow, representing an ideal reactor, and performs better than the circular cell. In all three models, increasing the inlet velocity while maintaining a constant initial electrolyte height (1 mm) results in higher  $E(t)$  peaks with shorter tails. This indicates that as inlet velocity increases, injected particles exit the cell more rapidly, with more uniform

### A.3. Results and discussion

---

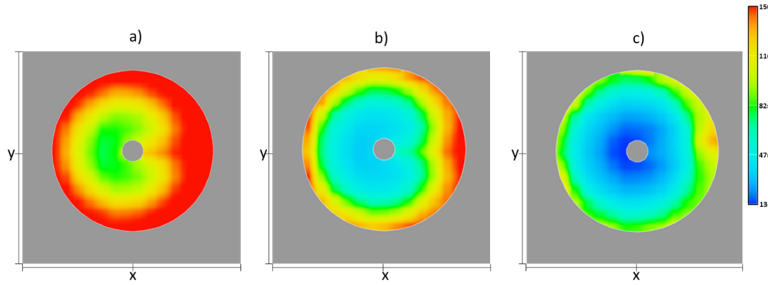


**Figure A.5:** LMA contour of the circular cell parallel and near the sample surface at velocities of a) 3, b) 6, and c) 9  $cm.s^{-1}$ .

flow and reduced dispersion. Consequently, at higher velocities, the cell behaves more similarly to an ideal plug flow reactor. The dependency of outlet tracer concentration on the initial electrolyte height, for a constant velocity of  $6\text{ cm.s}^{-1}$ , is illustrated in Figures A.10a and A.10b for the rhombic cell and the rhombic cell with a groove, respectively. A similar trend to that observed with increasing inlet velocity at a constant height is seen when reducing the initial electrolyte height at a constant inlet velocity. Specifically, as the initial height decreases, the  $E(t)$  curves become narrower and exhibit shorter tails, confirming that the reactor flow approaches ideal plug flow conditions under these circumstances.

While RTD calculations can predict the presence of dead zones within the cell, LMA (Local Mean Age) provides additional insight by identifying their precise location and dimensions. In essence, LMA calculates the average time required for a fluid element to travel from the inlet to a specific point within the cell domain.

Figures A.5, A.7, and A.9 illustrate the distribution of local fluid age on a plane parallel to and close to the sample surface (0.2 mm) for the circular, rhombic, and rhombic with groove designs, respectively. In all three models, the highest fluid ages occur in the stagnant zones near the O-ring. Furthermore, in all designs, increasing the inlet velocity reduces the size and extent of dead zones. For a more quantitative comparison, the average LMA values for each design at different inlet velocities are plotted in Figure A.11. The rhombic cell performs better at lower velocities, while the rhombic cell with a groove outperforms at higher velocities. This improvement at higher speeds is likely due to the formation of a direct flow path from the inlet to the sample surface in the grooved design. The ultimate objective is to achieve optimal LMA near the sample surface with minimal pumping speed. Higher pumping speeds introduce additional forces on the scanning tip, which can cause operational

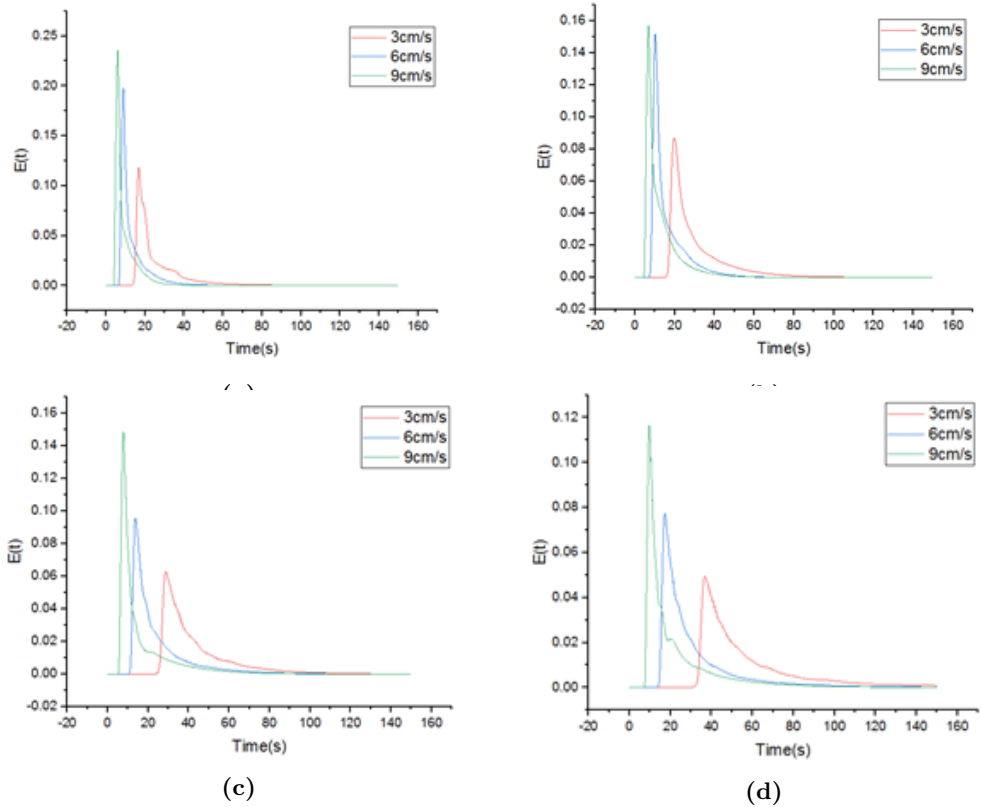


**Figure A.6:**  $E(t)$  function result for rhombic cell design at three velocities for different initial electrolyte levels, a) 0.7, b) 1, c) 1.5, and d) 2 mm.

A

### A.3. Results and discussion

---

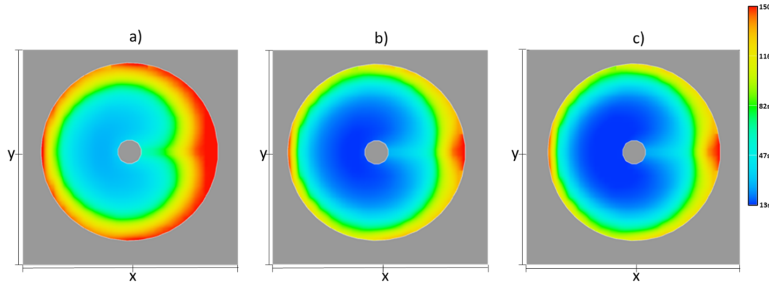


**Figure A.7:** LMA contour of rhombic cell parallel and near the sample surface at velocities of a) 3, b) 6, and c) 9  $cm.s^{-1}$ .

challenges.

The effects of initial conditions and cell type on flow behavior were analyzed based on the residence time distribution (RTD) and LMA near the sample surface. Results indicate that the rhombic cell is highly suitable as a flow medium, particularly at low inlet velocities, as evidenced by its sharper  $E(t)$  curve peaks and shorter tails compared to the circular cell. This reflects reduced axial dispersion and a flow closer to a plug flow. At high velocities, the rhombic cell with grooves performed better than the plain rhombic cell. However, at low velocities, the LMA near the sample surface was lower in the rhombic cell. Consequently, the rhombic cell was identified as the optimal design for the EC-STM system.

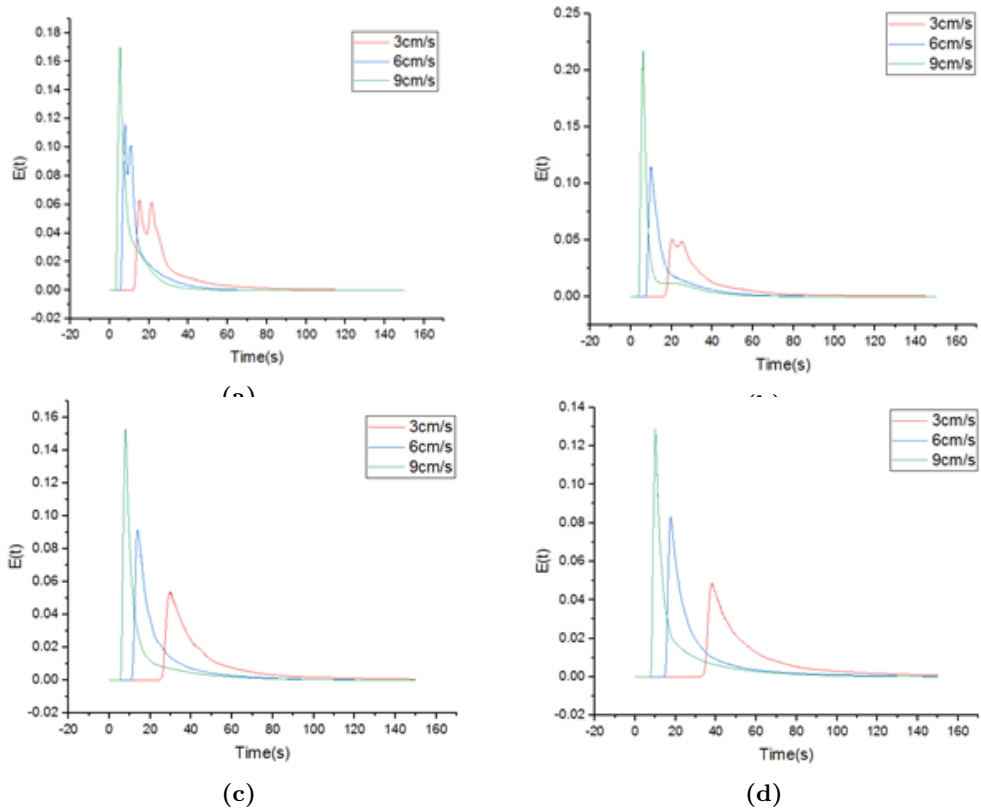


**Figure A.8:**  $E(t)$  function result for rhombic cell with a groove at three velocities for different initial electrolyte levels, a) 0.7, b) 1, c) 1.5, and d) 2 mm.

A

### A.3. Results and discussion

---

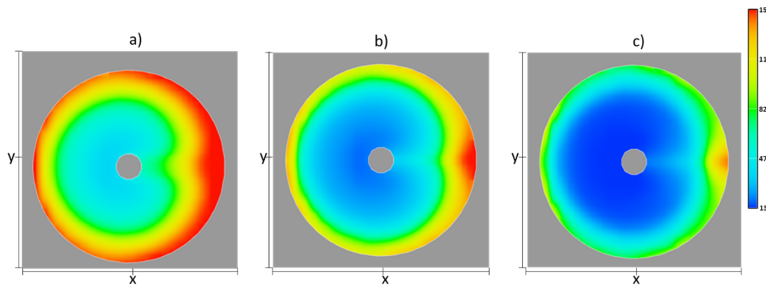


**Figure A.9:** LMA contour of rhombic cell with a groove, parallel and near the sample surface at velocities of a) 3, b) 6, and c) 9  $cm.s^{-1}$ .

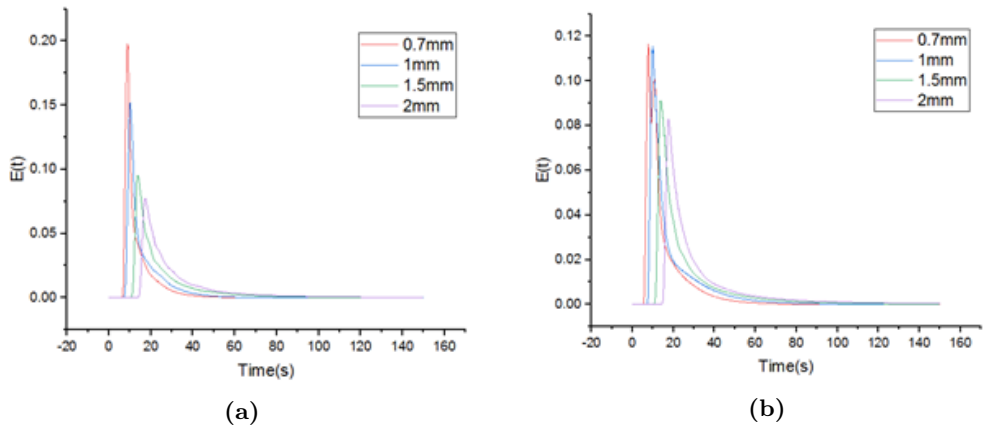
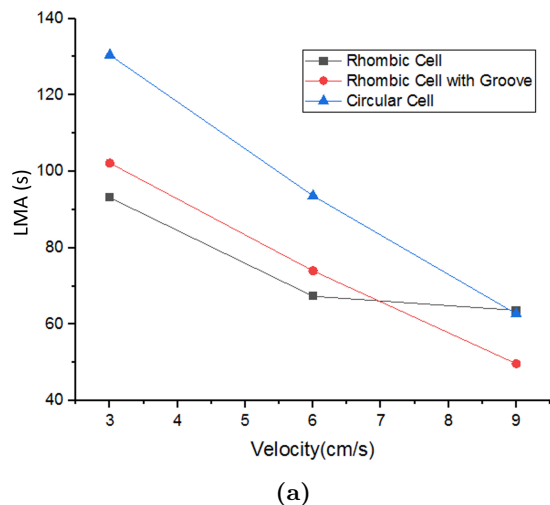


**Figure A.10:**  $E(t)$  function for different initial heights with the inlet velocity of 6  $cm.s^{-1}$  for a) rhombic cell, b) rhombic cell with groove.



(a)

**Figure A.11:** Average LMA value at the plane near the sample surface for all designs with initial electrolyte height of 1 mm at different speeds.

A



## Appendix B

# Supporting information for chapter 3

### B.1 Lifting the reconstruction for the experiment with holding the potential

The EC-STM image in Figure B.1a was initially recorded at 0 V just after the thermal annealing. The stripe reconstruction is visible, indicating that the sample is in good condition to start the experiment. There is a screw dislocation at the bottom-left part of the image which is a result of a defect in the crystal[122]. Subsequently, a voltage sweep from 0 to 0.2 V was applied, and Figure B.1b was recorded at 0.2 V. The image shows some defects/islands forming almost at the center of the imaged region. At this potential, we do not expect the lifting of the reconstruction since the electrode potential is lower than the potential of zero charge. It is possible to see the stripe reconstruction near the formed island which proves that the island formation cannot be due to the lifting of the reconstruction. After the potential was swept from 0.2 to 0.4 V, Figure B.1c was recorded at 0.4 V, depicting the two islands as a defect at the center. After sweeping the potential to 0.6 V, Figure B.1d was recorded, showing the generation of the small islands in the defect area. With a further sweep to 0.7 V, Figure B.1e was recorded, indicating some major changes in the step lines. It can be seen that the reconstruction lines are not as impacted as the pristine surface and they are not entirely parallel anymore. At 0.8 V, Figure B.1f was recorded, and lifting the reconstruction led to the formation of small islands all over the terraces. At 0.88 V

#### B.4. HHCF result for the instant frames

---

and 0.98 V, Figure B.1g and B.1h were recorded, respectively. By comparing Figure B.1f and B.1h, one can conclude that the island size increased at the expense of the smaller islands on the large terraces.

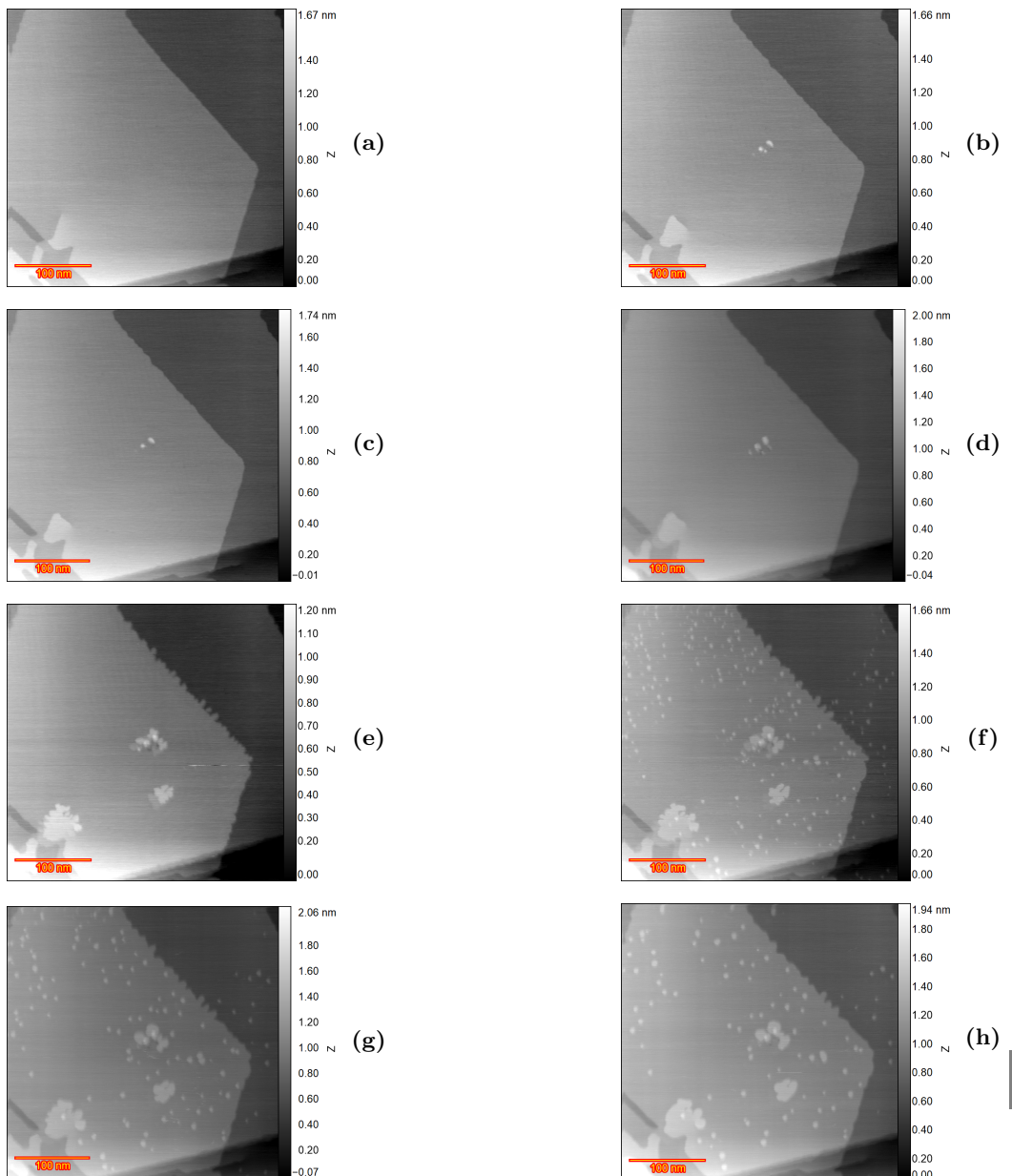
### B.2 HHCF result for the instant frames

Figure B.2a shows the HHCF for the instant frames in the experiment with holding potential in the double layer. As expected, increasing the cycle number increases the roughness magnitude and the correlation length shifts toward a higher radius. The roughness amplitude and correlation length versus cycle number for instant frames are shown in Figure B.2b revealing the linear behavior for roughness amplitude and a non-linear behavior for correlation length. At the initial stage of roughening, the islands grow in the 2D regime (corresponding to the correlation length), and as soon as they reach the size of ca. 20 nm, their lateral size changes more slowly and they tend to grow in the 3D regime.

### B.3 Curve fitting for OR charges

Equation B.1 is used to achieve the best curve fitting and the acquired coefficients are listed in Table B.1. The offset value (a) for reduction charge density is  $7.8 (\mu\text{C cm}^{-2})$  less than oxidation charge density and it can be related to the dissolution of gold in either anodic sweep[123] or reduction of gold oxide during cathodic sweep[124, 125], or in both directions[126]. The reported charge density difference per cycle in 0.5 M sulfuric acid is  $4.2 (\mu\text{C cm}^{-2})$  of which  $3.7 (\mu\text{C cm}^{-2})$  is caused by anodic sweep and  $0.5 (\mu\text{C cm}^{-2})$  by cathodic sweep[126]. The difference in offset value (a) for oxidation and reduction in our study is almost double the reported amount[126]. To have a better understanding of this happening, this difference versus cycle number is plotted in Figure B.3. This value is the highest for the first cycle and it decreases rapidly to  $7 (\mu\text{C cm}^{-2})$  and it continues to decrease over cycles. At the last cycle, it reaches  $4.83 (\mu\text{C cm}^{-2})$ . This also can explain the minor difference in the logarithm coefficient (b) for oxidation and reduction in Table B.1. With the reported coefficients and the fact that there is a linear correlation between the cycle number and the surface roughness, one can relate the oxidation or reduction charge density to the roughness value.

$$y = a - b \times \ln(x + c) \quad (\text{B.1})$$



**Figure B.1:** Au(111) in 0.1 M sulfuric acid with the image size of 350×350 nm at different potentials a) 0, b) 0.2, c) 0.4, d) 0.6, e) 0.7, f) 0.8, g) 0.88, and h) 0.98 V versus RHE.

B

#### B.4. Curve fitting for OR charges

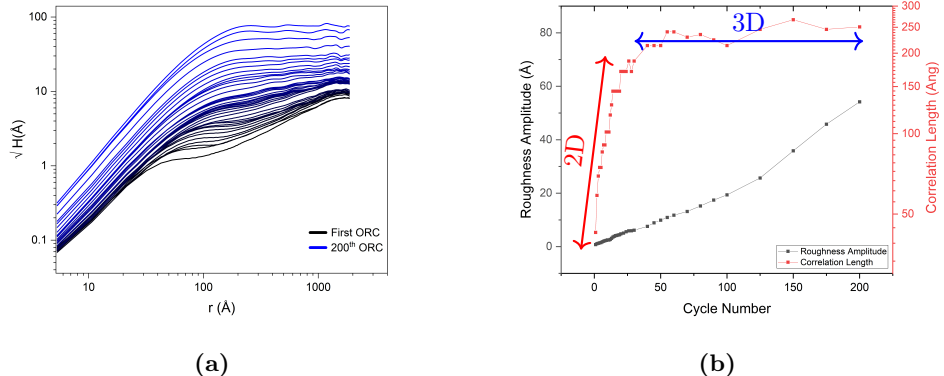


**Figure B.2:** a) Height-height correlation function versus distance  $r$  for Au(111) in 0.1 M sulfuric acid as a function of the number of oxidation-reduction cycles (ORCs) for the experiment with holding potential in the double layer for the instant frames. b) Extracted roughness amplitude and correlation length versus cycle number from the HHCF results. The arrows indicate the 2D and 3D island growth regimes.

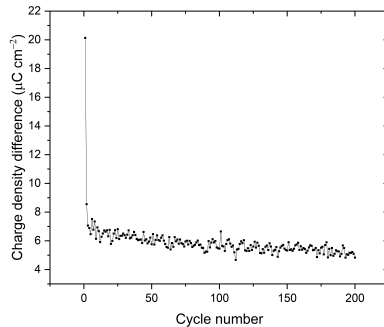


**Figure B.3:** Calculated the difference in oxidation-reduction charge density ( $\mu\text{C cm}^{-2}$ ) in cyclic voltammogram of the consecutively applied 200 ORCs on Au(111) in 0.1 M  $\text{H}_2\text{SO}_4$  with a scan rate of  $50 \text{ mV s}^{-1}$  versus RHE.

**Table B.1:** The calculated coefficients for curve-fitting on the oxidation-reduction charge density shown in Figure 9b by using EquationB.1.

Reduction Coefficients	Oxidation Coefficients
$a = 561.47713 \pm 0.39641$	$a = 569.28624 \pm 0.41304$
$b = 5.29827 \pm 0.08969$	$b = 5.76885 \pm 0.09353$
$c = -0.9771 \pm 0.00608$	$c = -0.99642 \pm 9.70464\text{E-}4$

## B.4 Oxidation-Reduction charge density with holding the potential

Oxidation-Reduction charge density for the experiment with holding potential in the double layer is shown in Figure B.4a. In this experiment, more delays were applied, and as a result, different CVs and oxidation-reduction charge densities are expected. The amplitude of the main oxidation peak for the first and second cycles is not as noticeable as for the aforementioned results due to the applied delay. This behavior can also be seen in Figure B.4b as the charge density does not drop as fast as in other experiments. For the first twenty cycles no spike can be seen in the charge density since after each cycle the delay has been applied. However, after the twentieth cycle, the spikes appeared on the cycles subsequent to the delays. Regardless of the spikes, the general trend is an approximately logarithmic decay of the charge density over cycles.

#### B.4. Oxidation-Reduction charge density with holding the potential

---

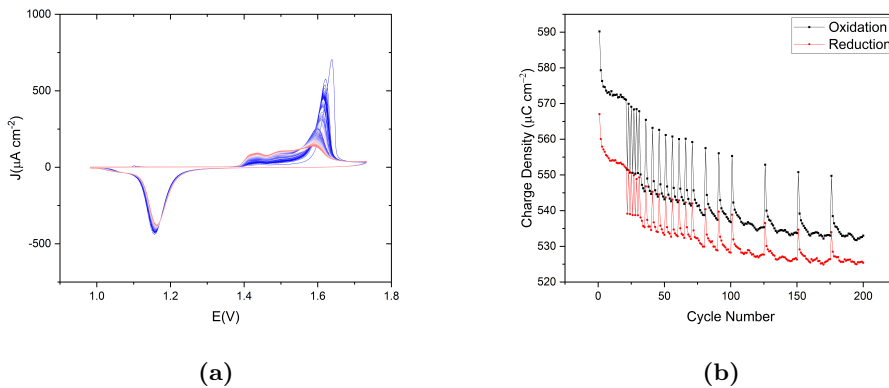


**Figure B.4:** a) Cyclic voltammogram of the applied 200 ORCs on Au(111) in 0.1 M sulfuric acid with a scan rate of  $50 \text{ mV s}^{-1}$  versus RHE for the experiment with holding potential in double layer. The color gradient from blue to red corresponds to the progression from the first to the last cycle. b) Calculated oxidation-reduction charge density ( $\mu\text{C cm}^{-2}$ ) versus the cycle number for the CVs shown in (a).

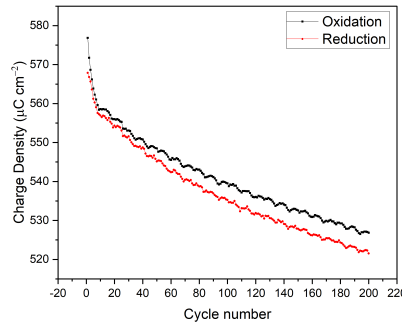
## Appendix C

# Supporting information for chapter 5

C

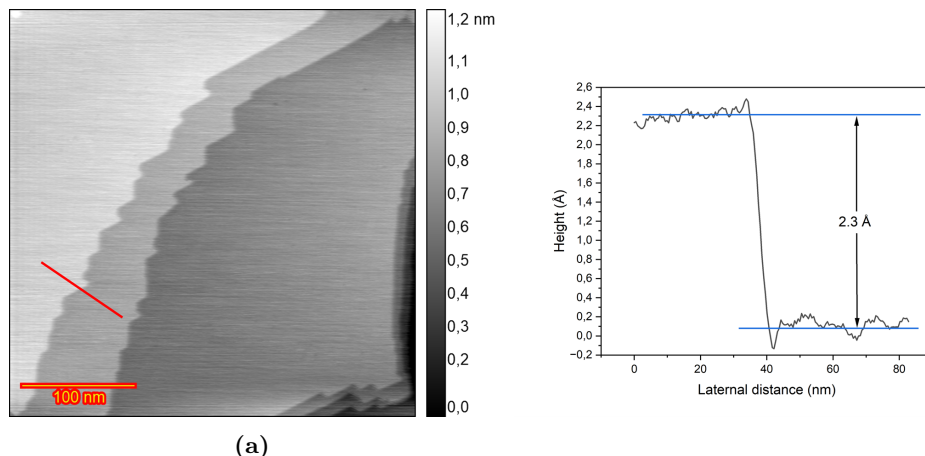
## C.1. Au(111) in 0.1 M HClO<sub>4</sub>

### C.1 Au(111) in 0.1 M HClO<sub>4</sub>



(a)

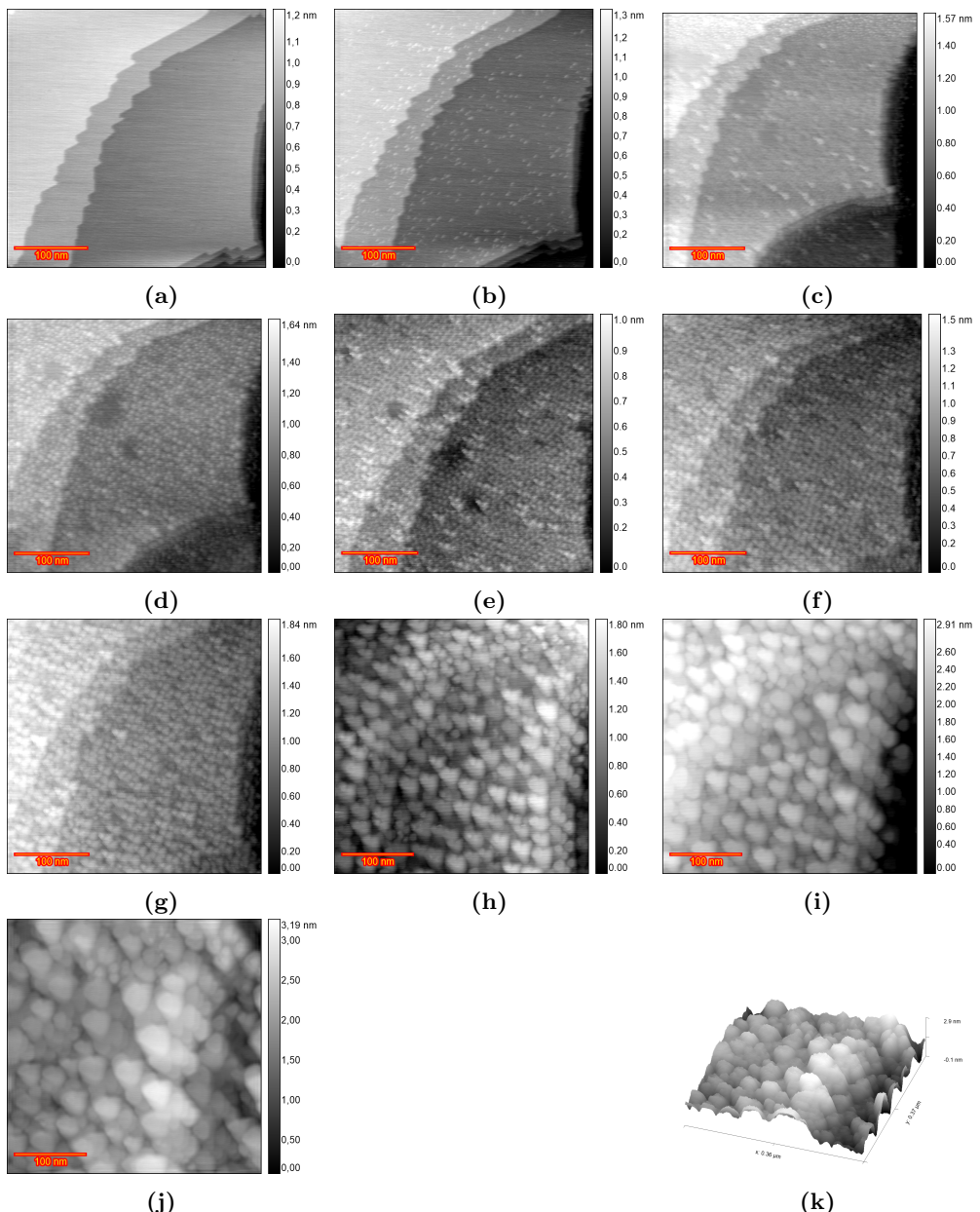
**Figure C.1:** Calculated oxidation and reduction charge densities for Au(111) in 0.1 M HClO<sub>4</sub> for 200 ORCs.



(a)

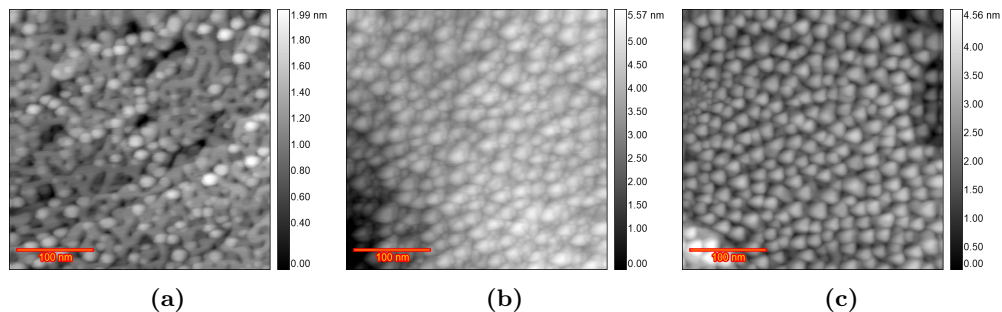
**Figure C.2:** EC-STM image (350×350 nm) of Au(111) in 0.1 M HClO<sub>4</sub>. a) Sample surface at 0.7 V vs RHE just after annealing b) the corresponding height profile of the indicated red line in (a) that shows the step height for Au(111)

In the experiment shown in Figure C.3e-g, there is some evidence of a tip-shape effect. Thus, this effect should be considered in the discussions and conclusions for the mentioned images. However, it does not influence the final broader conclusions.



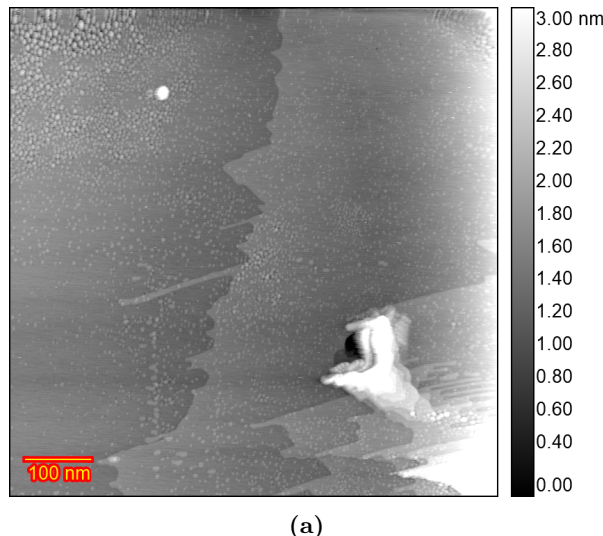
**Figure C.3:** EC-STM image (350×350 nm) of Au(111) in 0.1 M HClO<sub>4</sub>. a) Sample surface at 0.7 V vs RHE just after annealing. b) partially lifted reconstruction at 0.9 V. c) after n ORCs from 0.9 to 1.65 V and imaging at 0.9 V n=5 d) n=15 e) n=25 f) n=40 g) n=50 h) n=110 i) n=170 j) n=200 k) 3D image after 200 ORCs.

### C.1. Au(111) in 0.1 M HClO<sub>4</sub>

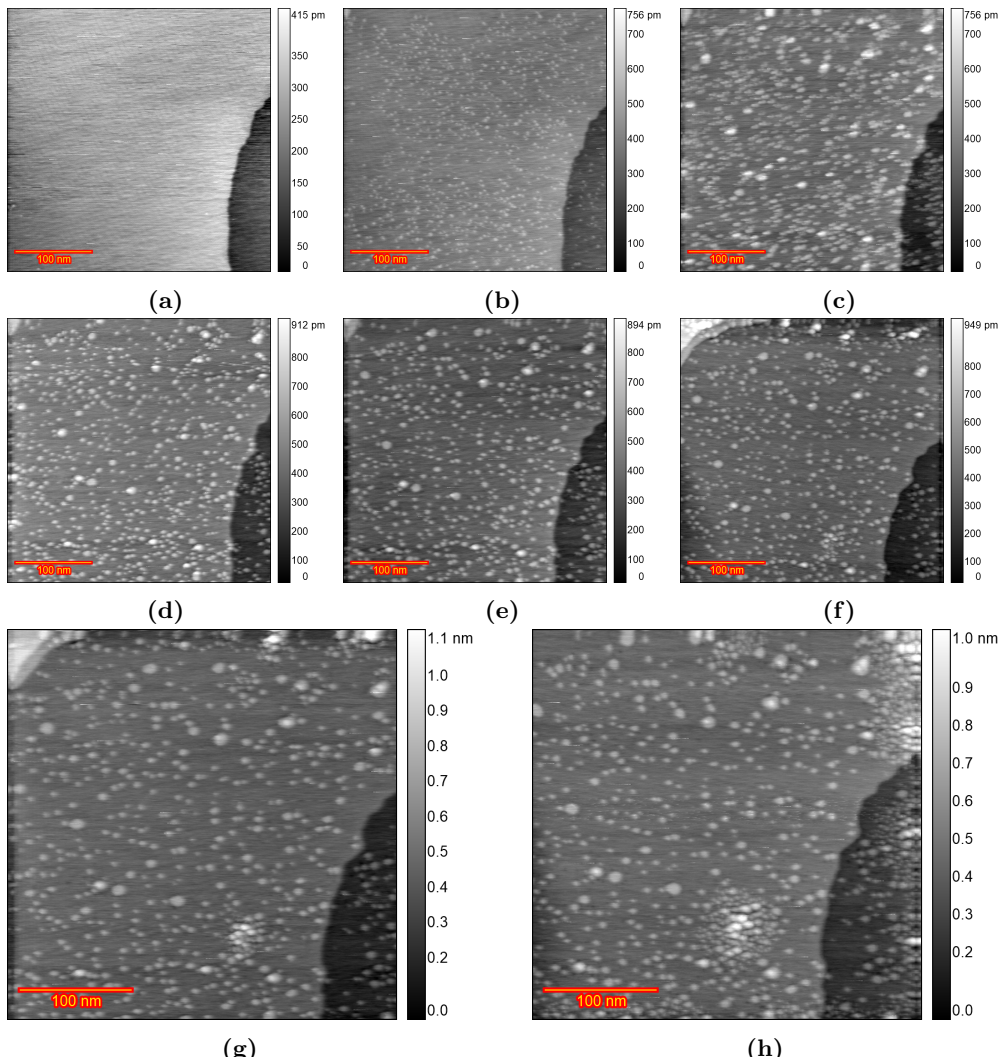


**Figure C.4:** EC-STM image (350×350 nm) of Au(111) in 0.1 M HClO<sub>4</sub> for three different experiment. a) after 200 b,c) after 70 oxidation-reduction cycle.

In the experiment shown in Figure C.6, increasing the upper potential limit to 1.8 V after the 13th ORC was tested and led to the formation of some new islands in the bottom right of the image in Figures C.6g and C.6h. This observation needs more investigation since this indicates the possibility of an unexpected inhibition of the surface oxidation reaction in these areas.

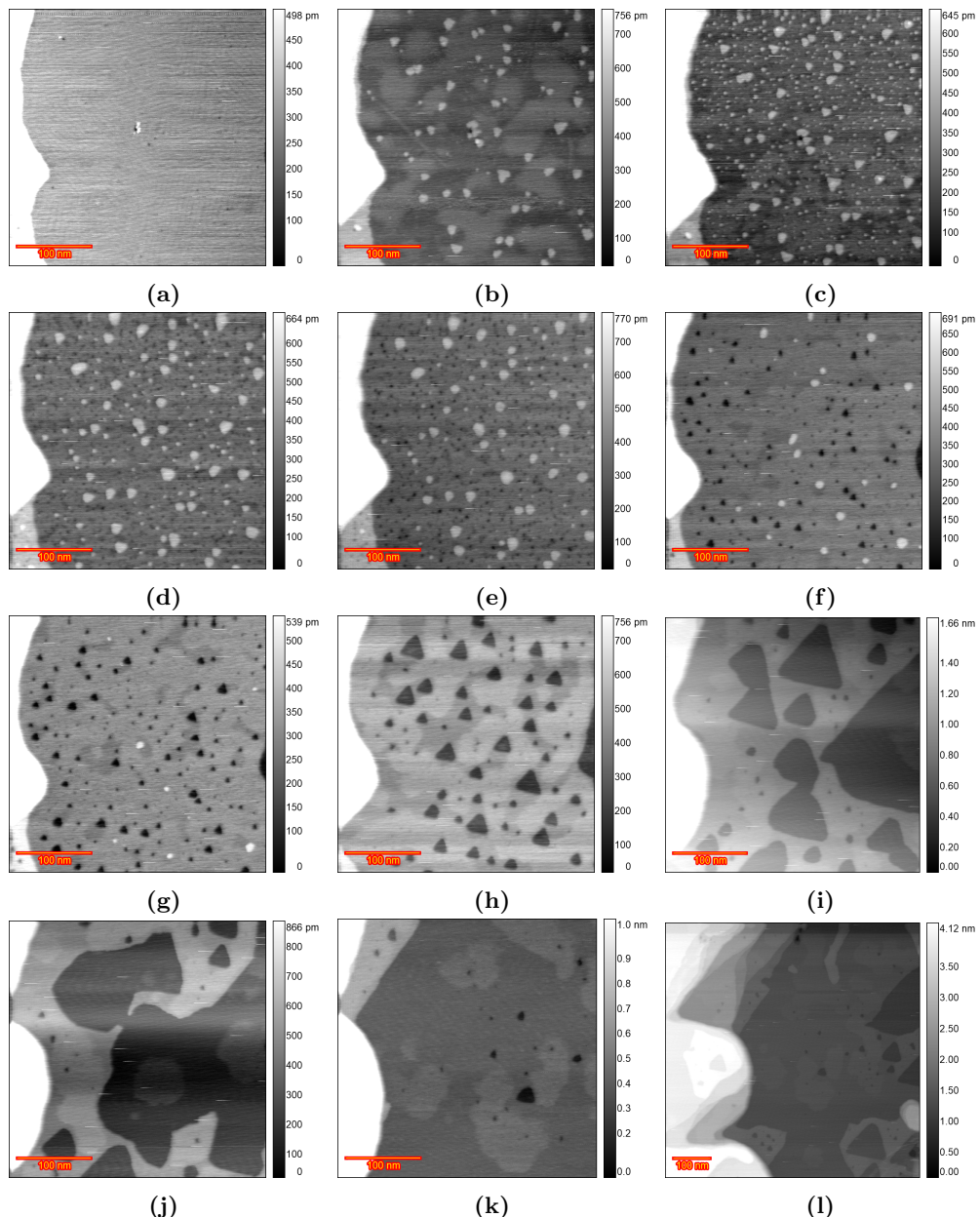


**Figure C.5:** EC-STM image (700×700 nm) of Au(111) in 0.1 M HClO<sub>4</sub>. after 40 cycles. the surface remained largely unchanged except for a few areas.

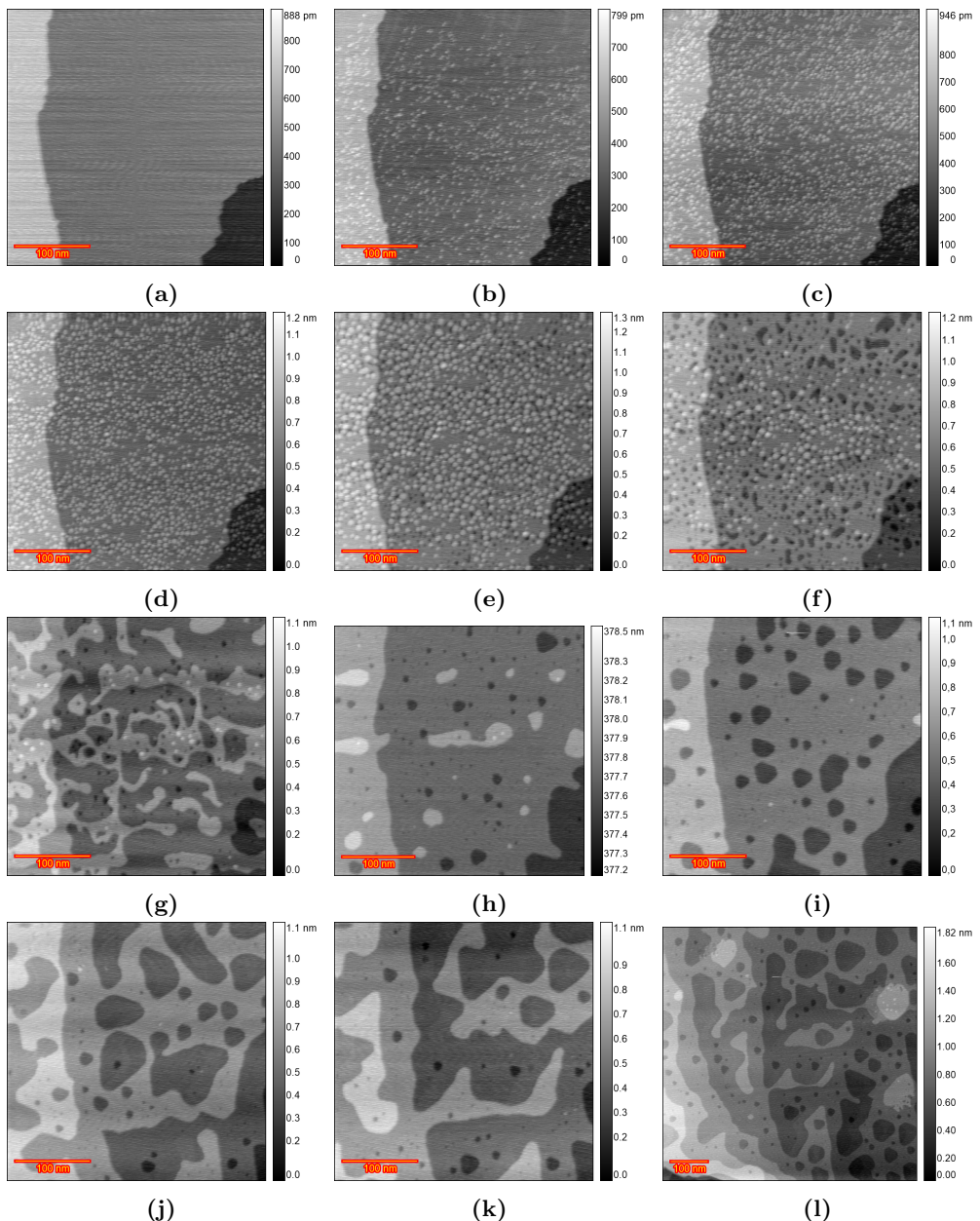


**Figure C.6:** EC-STM image ( $350 \times 350$  nm) of Au(111) in 0.1 M  $\text{HClO}_4$ . a) Sample surface just after annealing. b) lifted reconstruction at 0.9 V. c) after  $n$  ORCs from 0.9 to 1.65 V and imaging at 0.9 V  $n=1$  d)  $n=5$  e)  $n=13$  f)  $n=15$  g)  $n=20$  h)  $n=30$ .

### C.1. Au(111) in 0.1 M HClO<sub>4</sub>



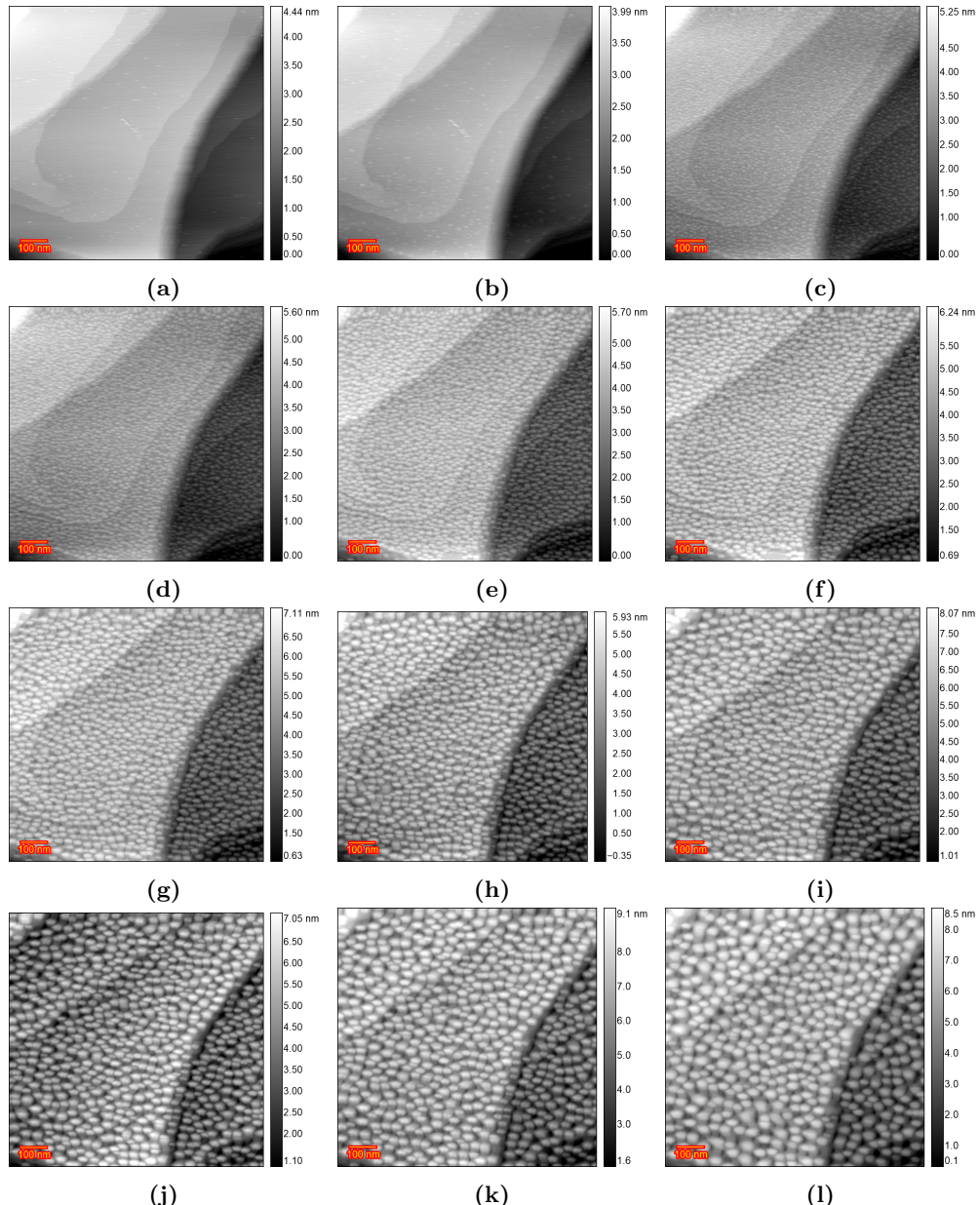
**Figure C.7:** EC-STM image of Au(111) in 0.1 M HClO<sub>4</sub>. a) Sample surface just after annealing. b) lifted reconstruction at 0.95 V. c) after n ORCs from 0.9 to 1.65 V, n=1,d) n=5, e) n=8, f) n=15, g) n=20, h) n=50, i) n=125, j) n=150, k) n=200, l) zoomed out after 200 ORCs.



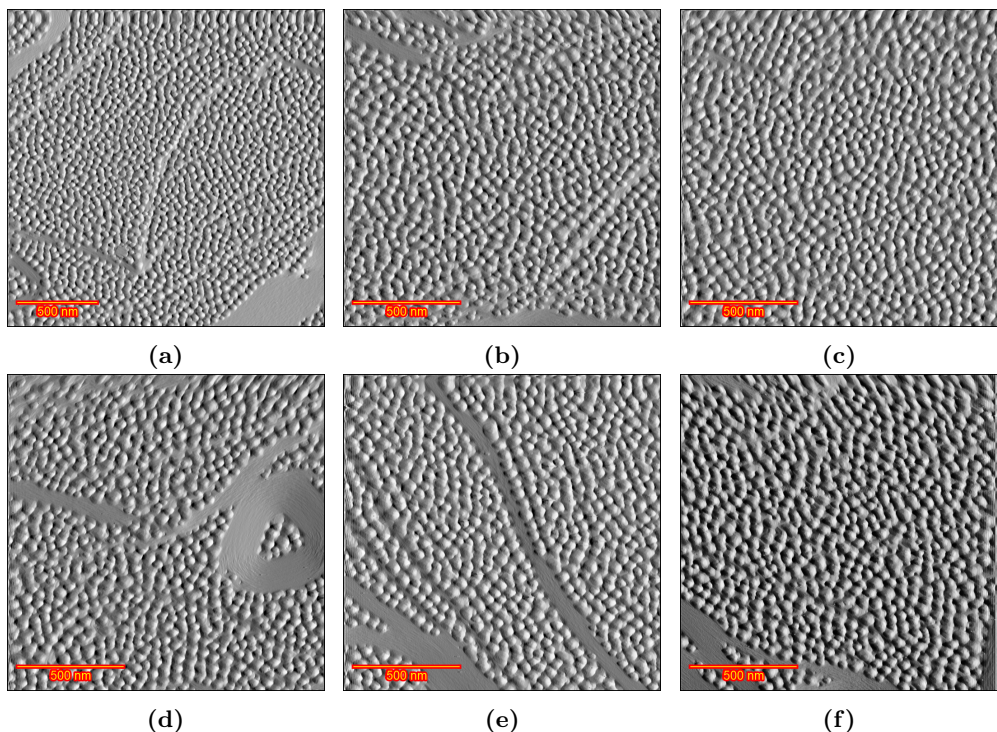
**Figure C.8:** EC-STM image of Au(111) in 0.1 M HClO<sub>4</sub> (ROTIPURAN), a) Sample surface just after annealing, b) lifted reconstruction at 0.9 V, c) after n ORCs from 0.9 to 1.65 V, n=2, d) n=5, e) n=20, f) n=30, g) n=50, h) n=70, i) n=100, j) n=150, k) n=175, l) n=200 zoomed out.

## C.2. Au(111) in 0.1 M HClO<sub>4</sub> and 10 $\mu$ M H<sub>2</sub>SO<sub>4</sub>

### C.2 Au(111) in 0.1 M HClO<sub>4</sub> and 10 $\mu$ M H<sub>2</sub>SO<sub>4</sub>



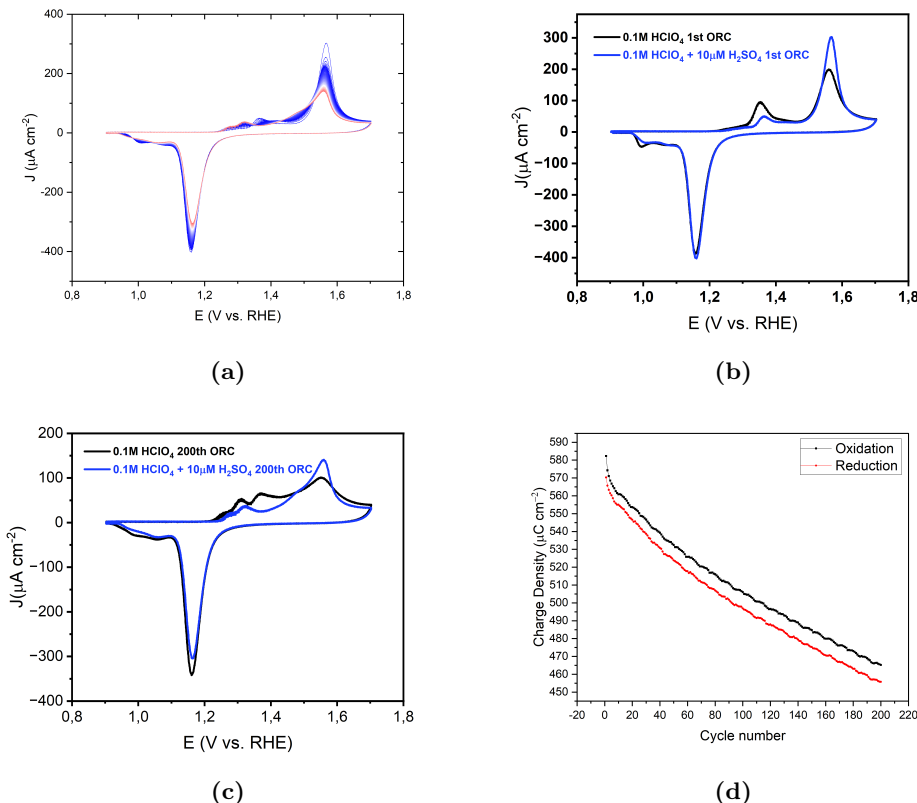
**Figure C.9:** EC-STM image of Au(111) in 0.1 M HClO<sub>4</sub> and 10  $\mu$ M H<sub>2</sub>SO<sub>4</sub>, a) Sample surface just after annealing, b) lifted reconstruction at 0.9 V, c) after n ORCs from 0.8 to 1.65 V, n=10, d) n=20, e) n=35, f) n=50, g) n=75, h) n=100, i) n=125, j) n=150, k) n=175, l) n=200.



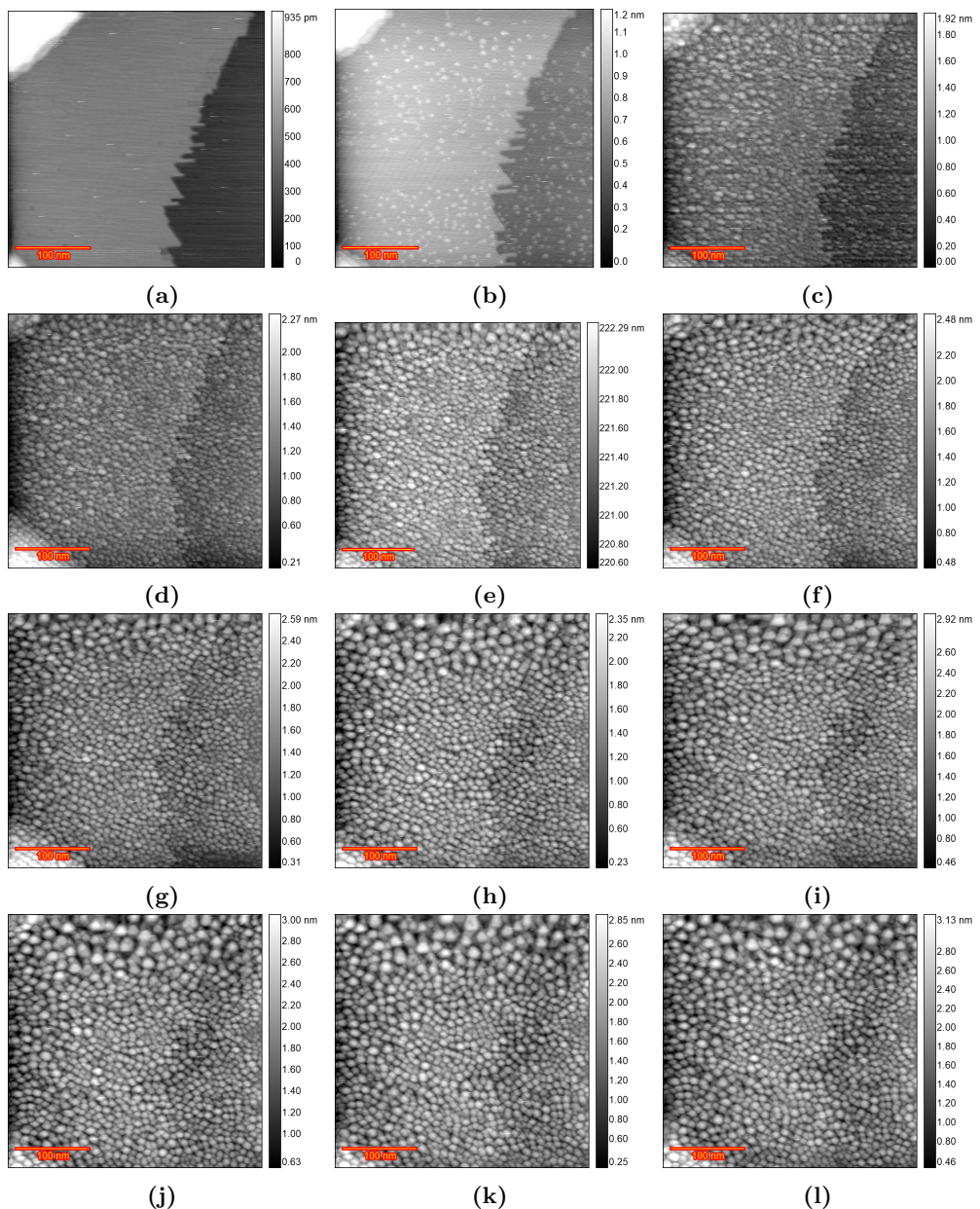
**Figure C.10:** Sequence of EC-STM images of Au (111) at different/random locations after 200 ORCs in 0.1 M  $\text{HClO}_4$  and 10  $\mu\text{M}$   $\text{H}_2\text{SO}_4$  in differential mode.

Figure C.11a shows the corresponding CVs of the 200 ORCs of the annealed Au (111) in a conventional electrochemical cell containing  $\text{HClO}_4$  solution + 10  $\mu\text{M}$   $\text{H}_2\text{SO}_4$ , scanning from 0.9 to 1.7 V at  $50 \text{ mV s}^{-1}$  from the first cycle (in blue) to the 200th cycle (in red). Comparing the CVs after the first oxidation-reduction cycle in the  $\text{H}_2\text{SO}_4$ -containing electrolyte and pure  $\text{HClO}_4$  (Figure C.11b), shows an increase in oxide formation (O4) and decrease in OH adsorption (O3) peak in the sulfate-containing solution. This can be explained by the blocking effect of absorbed sulfate on the surface at positive potentials, which blocks the chemisorption of  $\text{OH}^-$  [105, 106]. Further oxidation-reduction cycles lead to a decrease in both O4 and O3 peaks, while the O3 peak completely disappears after 200 ORCs for the sulfate containing electrolyte (Figure C.11c). The O2 and O1 peaks become more visible with the roughness increase (Figure C.11a). Figure C.11d shows oxidation reduction charge density for the 200 ORCs.

## C.2. Au(111) in 0.1 M HClO<sub>4</sub> and 10 $\mu$ M H<sub>2</sub>SO<sub>4</sub>



**Figure C.11:** CV of Au(111) in 0.1 M HClO<sub>4</sub> containing 10  $\mu$ M H<sub>2</sub>SO<sub>4</sub> in the potential window of 0.9 to 1.7 V versus RHE. a) All the CVs from the first (Blue) to 200<sup>th</sup> (red). b) comparison of the first CV of pure 0.1 M HClO<sub>4</sub> (black) and the electrolyte containing 10  $\mu$ M H<sub>2</sub>SO<sub>4</sub> (blue). c) comparison of the 200th CV of pure 0.1 M HClO<sub>4</sub> (black) and the electrolyte containing 10  $\mu$ M H<sub>2</sub>SO<sub>4</sub> (blue). d) Calculated oxidation and reduction charge densities for 200 ORCs.



**Figure C.12:** Full sequence EC-STM images ( $350 \times 350$  nm) of experiment in 0.1 M  $\text{HClO}_4$  containing  $10 \mu\text{M H}_2\text{SO}_4$ . a) Sample surface just after annealing, b) lifted reconstruction at 0.9 V, c) after  $n$  ORCs from 0.8 to 1.65 V,  $n=10$ , d)  $n=20$ , e)  $n=35$ , f)  $n=50$ , g)  $n=75$ , h)  $n=100$ , i)  $n=125$ , j)  $n=150$ , k)  $n=175$ , l)  $n=200$ .

### C.3 Au(111) in 0.1 M HClO<sub>4</sub> and 10 $\mu$ M HCl

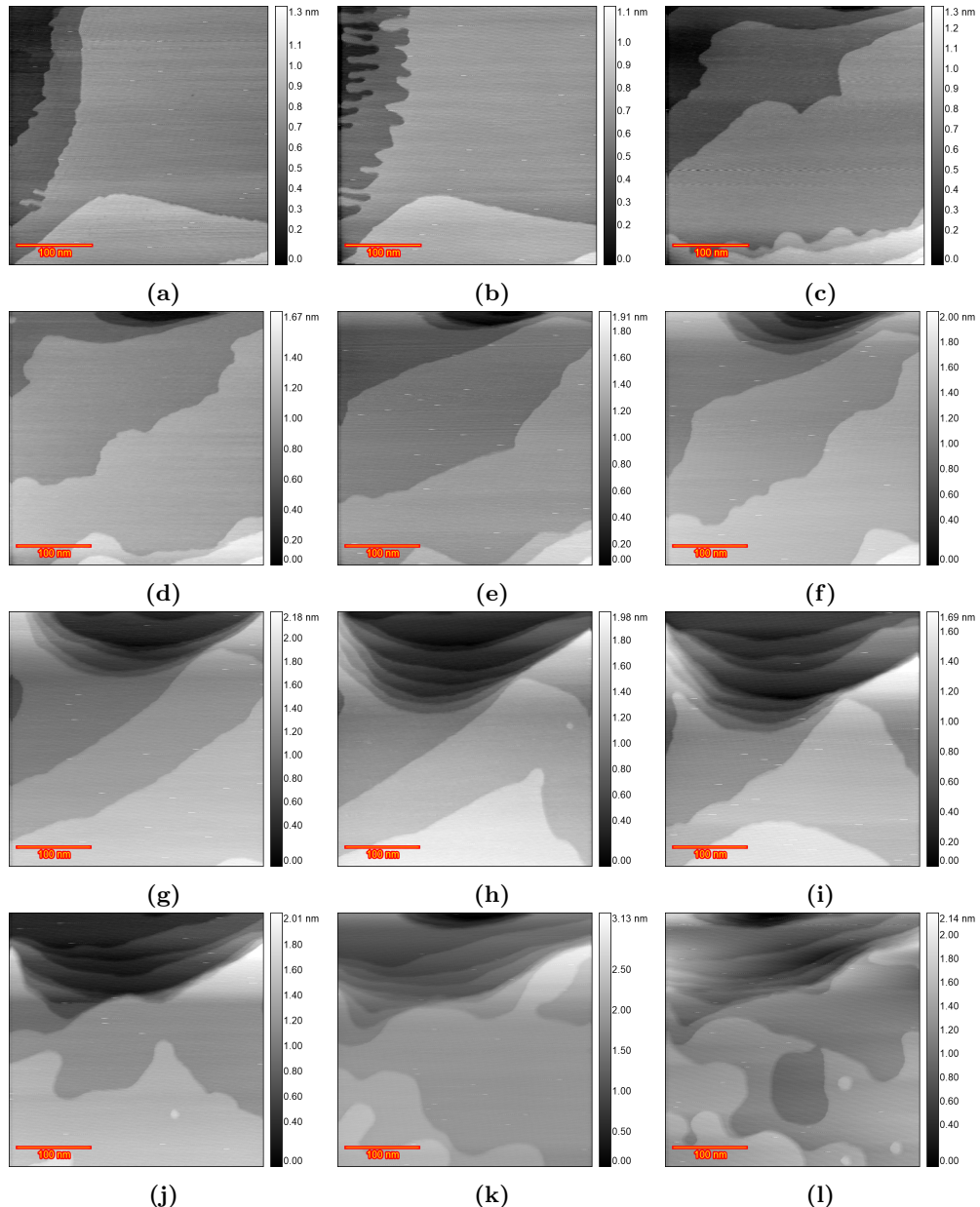


**Figure C.13:** Full sequence EC-STM images (350×350 nm) of experiment in 0.1 M HClO<sub>4</sub> containing 10  $\mu$ M HCl. a) Sample surface just after annealing, b) lifted reconstruction at 0.9 V, c) after n ORCs from 0.8 to 1.65 V, n=10, d) n=20, e) n=35, f) n=50, g) n=75, h) n=100, i) n=125, j) n=150, k) n=175, l) n=200.

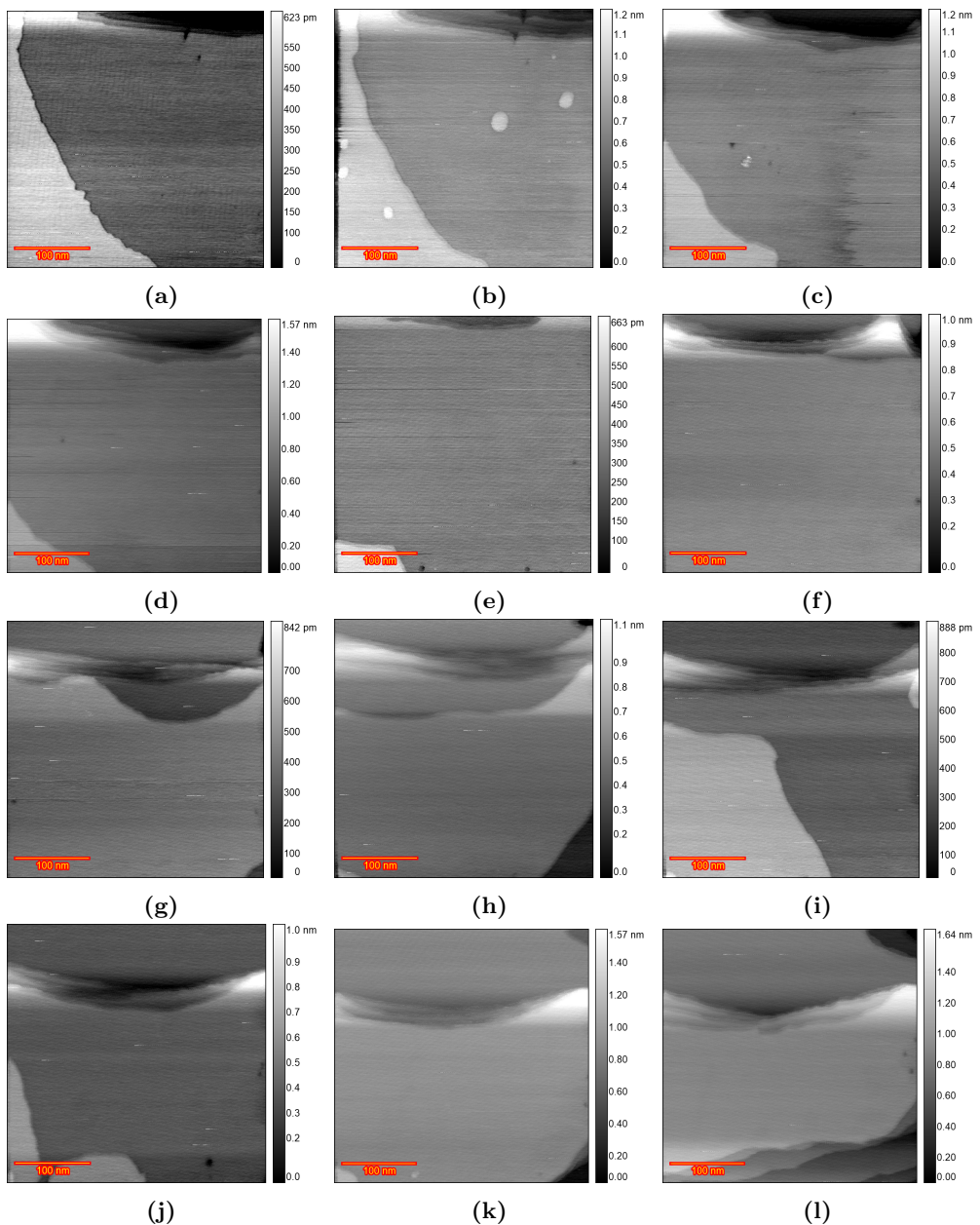


**Figure C.14:** Full sequence EC-STM images ( $350 \times 350$  nm) of experiment in 0.1 M  $\text{HClO}_4$  containing 10  $\mu\text{M}$  HCl. a) Sample surface just after annealing, b) lifted reconstruction at 0.9 V, c) after n ORCs from 0.8 to 1.65 V, n=10, d) n=20, e) n=35, f) n=50, g) n=75, h) n=100, i) n=125, j) n=150, k) n=175, l) n=200.

### C.3. Au(111) in 0.1 M HClO<sub>4</sub> and 10 $\mu$ M HCl

---

In a surprising discovery, repeating the experiment shown in Figure 5.8 revealed a behavior of growing vacancy islands similar to that observed in pure HClO<sub>4</sub> (experiments in Figures 5.4 and 5.5). At 0 V, terraces with a well-defined herringbone reconstruction divided by monatomic height step lines were evident (Figure C.15a). At 0.9 V, some areas showed island formation due to the lifting of the reconstruction (Figure C.15b). After performing 10 ORCs from 0.8 to 1.65 V at 50  $mVs^{-1}$  and maintaining the potential at 0.8 V during imaging (Figure C.15c), islands disappeared and the surface was partially covered with pits and some recession was observed in the step lines, similar to our previous observations in pure HClO<sub>4</sub> (Figures 5.4 and 5.5) which were affected by impurities. Imaging after 20 ORCs (Figure C.15d) revealed the disappearance of pits and an increased recession rate of the step lines, consistent with what is expected from an HClO<sub>4</sub> solution containing Cl, as observed in Figure 5.8. This phenomenon is likely due to the increased mobility of gold surface atoms, influenced by the greater presence of locally adsorbed Cl<sup>-</sup> on the terraces by the experiment time. After 75 ORCs Figure C.15e shows that the step lines have receded and the terraces appear pristine. However, after 125 ORCs (Figure C.15f), some areas show pits, probably due to a lack of Cl<sup>-</sup> ions on the newly exposed terraces following the etching of the front terrace through the receding step lines.

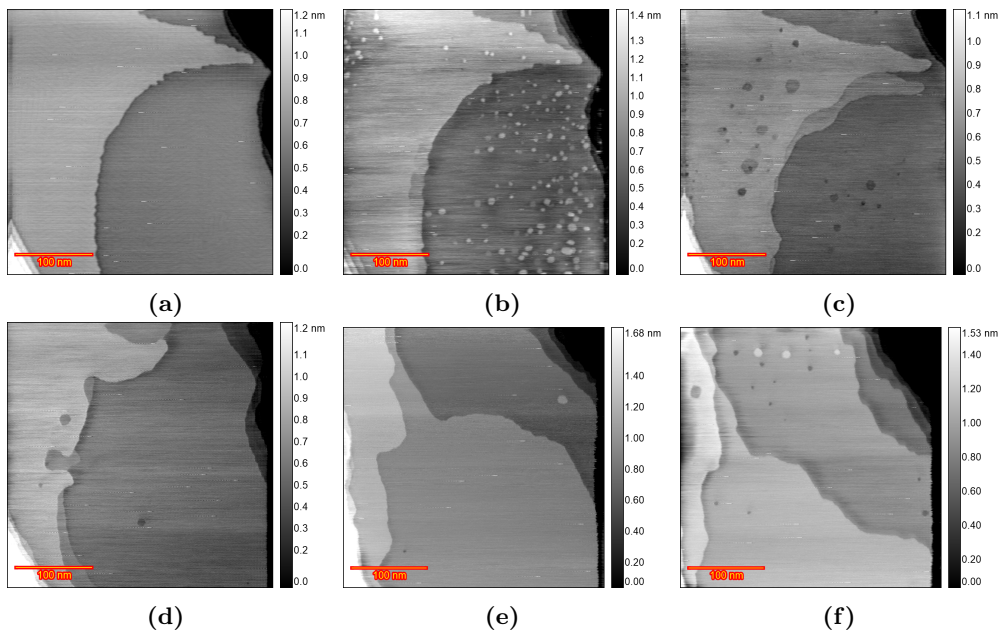
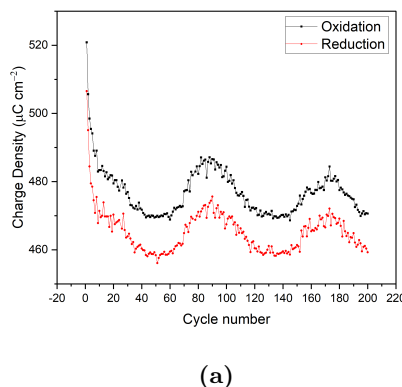


**Figure C.15:** EC-STM image( $350 \times 350$  nm) of Au(111) in 0.1 M  $\text{HClO}_4$  containing 10  $\mu\text{M}$  HCl. a) Sample surface at 0.0 V vs RHE just after annealing. b) partially lifted reconstruction at 0.9 V. c) after n ORCs from 0.8 to 1.65 V and imaging at 0.8 V n=10 d) n=20 e) n=75 f) n=125.

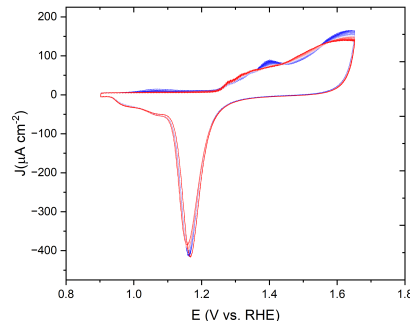


(a)

**Figure C.16:** Calculated oxidation and reduction charge densities of Au(111) in 0.1 M  $\text{HClO}_4$  containing 10  $\mu\text{M}$  HCl in the potential window of 0.9 to 1.7 V versus RHE for 200 ORCs.

C

## C.4 Recorded CV on EC-STM



(a)

**Figure C.17:** Recorded CV of Au(111) in 0.1 M  $\text{HClO}_4$  in the potential window of 0.9 to 1.65 V versus RHE during the EC-STM experiments in the EC-STM cell. The first CV is presented in blue and the last one is in red.

# Bibliography

- [1] L. Galvani. *De Viribus Electricitatis in Motu Muscolari Commentarius*. Ex Typographia Instituti Scientiarium, Bononiae,, 1791.
- [2] Wolfgang Schmickler and Elizabeth Santos. *Interfacial Electrochemistry*. Springer Berlin Heidelberg, Berlin, Heidelberg, 2010.
- [3] Larry R. Faulkner Allen J. Bard. *Electrochemical Methods: Fundamentals and Applications, 2nd Edition*, volume 677. Wiley; 2nd edition, 2004.
- [4] Dieter M. Kolb. Electrochemical Surface Science. *Angewandte Chemie International Edition*, 40(7):1162–1181, apr 2001.
- [5] Xiaoting Chen and Marc T. M. Koper. In situ ec-afm study of the initial stages of cathodic corrosion of pt(111) and polycrystalline pt in acid solution. *The Journal of Physical Chemistry Letters*, 14(21):4997–5003, 2023. PMID: 37222413.
- [6] Carsten Köntje, Dieter M. Kolb, and Gregory Jerkiewicz. Roughening and long-range nanopatterning of au(111) through potential cycling in aqueous acidic media. *Langmuir*, 29:10272–10278, 8 2013.
- [7] Georg H. Simon, Christopher S. Kley, and Beatriz Roldan Cuenya. Potential-dependent morphology of copper catalysts during co<sub>2</sub> electroreduction revealed by in-situ atomic force microscopy. *Angewandte Chemie International Edition*, 60(5):2561–2568, 2021.
- [8] Toshihiro Kondo, Jun Morita, Kazuya Hanaoka, Satoru Takakusagi, Kazuhisa Tamura, Masamitu Takahasi, Jun'ichiro Mizuki, and Kohei Uosaki. Structure of Au(111) and Au(100) Single-Crystal Electrode Surfaces at Various Potentials in Sulfuric Acid Solution Determined by In Situ Surface X-ray Scattering. *The Journal of Physical Chemistry C*, 111(35):13197–13204, sep 2007.
- [9] Hassan Javed, Kees Kolmeijer, Nick Klein, Jamie A. Trindell, Gregory Schneider, and Rik V. Mom. A laboratory-based electrochemical nap-xps system for operando electrocatalysis studies. *Vacuum*, 231:113755, 2025.
- [10] G Binning, H Rohrer, Ch Gerber, and E Weibel. Surface Studies by Scanning Tunneling Microscopy. *Phys. Rev*, 49(1):57, 1982.

## Bibliography

---

- [11] G. Binnig, H. Rohrer, Ch Gerber, and E. Weibel. Tunneling through a controllable vacuum gap. *Applied Physics Letters*, 40(2):178–180, jan 1982.
- [12] W. Ho. Single-molecule chemistry. *The Journal of Chemical Physics*, 117(24):11033–11061, dec 2002.
- [13] Harold J.W. Zandvliet and Arie van Houselt. Scanning Tunneling Spectroscopy. *Annual Review of Analytical Chemistry*, 2(1):37–55, jul 2009.
- [14] D. M. Eigler and E. K. Schweizer. Positioning single atoms with a scanning tunnelling microscope. *Nature*, 344(6266):524–526, apr 1990.
- [15] C. Julian Chen. *Introduction to Scanning Tunneling Microscopy*. Oxford University PressOxford, third edition, mar 2021.
- [16] Milutin Stanacevic, Kartikeya Murari, Abhishek Rege, Gert Cauwenberghs, and Nitish V. Thakor. VLSI Potentiostat Array With Oversampling Gain Modulation for Wide-Range Neurotransmitter Sensing. *IEEE Transactions on Biomedical Circuits and Systems*, 1(1):63–72, mar 2007.
- [17] B Drake, R. Sonnenfeld, J. Schneir, and P.K. Hansma. Scanning tunneling microscopy of processes at liquid-solid interfaces. *Surface Science*, 181(1-2):92–97, mar 1987.
- [18] J. V. Barth, H. Brune, G. Ertl, and R. J. Behm. Scanning tunneling microscopy observations on the reconstructed Au(111) surface: Atomic structure, long-range superstructure, rotational domains, and surface defects. *Physical Review B*, 42(15):9307–9318, nov 1990.
- [19] U. Harten, A. M. Lahee, J. Peter Toennies, and Ch. Wöll. Observation of a Soliton Reconstruction of Au(111) by High-Resolution Helium-Atom Diffraction. *Physical Review Letters*, 54(24):2619–2622, jun 1985.
- [20] M Schneeweiss. Oxide formation on Au(111) an in situ STM study. *Solid State Ionics*, 94(1-4):171–179, feb 1997.
- [21] B.E. Conway. Electrochemical oxide film formation at noble metals as a surface-chemical process. *Progress in Surface Science*, 49(4):331–452, aug 1995.
- [22] Marie Anne Schneeweiss, Dieter M. Kolb, Dezhong Liu, and Daniel Mandler. Anodic oxidation of Au(111). *Canadian Journal of Chemistry*, 75(11):1703–1709, nov 1997.
- [23] Fernando Silva, Cosme Moura, and A. Hamelin. Formation of a monolayer of oxide on gold single crystal face electrodes in sulphamic acid solutions. *Electrochimica Acta*, 34(12):1665–1671, dec 1989.
- [24] Oscar Diaz-Morales, Federico Calle-Vallejo, Casper de Munck, and Marc T M Koper. Electrochemical water splitting by gold: evidence for an oxide decomposition mechanism. *Chemical Science*, 4(6):2334, 2013.

- [25] S. Bourkane, C. Gabrielle, F. Huet, and M. Keddam. Investigation of gold oxidation in sulfuric medium—I. Electrochemical impedance techniques. *Electrochimica Acta*, 38(7):1023–1028, may 1993.
- [26] Ping Gao, David Gosztola, Lam-Wing H Leung, and Michael J Weaver. Surface-enhanced Raman scattering at gold electrodes: dependence on electrochemical pretreatment conditions and comparisons with silver. *Journal of Electroanalytical Chemistry and Interfacial Electrochemistry*, 233(1-2):211–222, sep 1987.
- [27] Karrie J. Hanson and Michael P. Green. Electrochemical Roughening and Annealing of Au(111) Surfaces in Perchloric and Sulfuric Acid Electrolytes Studied by STM. *MRS Proceedings*, 237(111):323, feb 1991.
- [28] Andrzej Wieckowski. *Interfacial Electrochemistry*. Routledge, nov 2017.
- [29] Johannes M. Hermann, Areeg Abdelrahman, Timo Jacob, and Ludwig A. Kibler. Potential-dependent reconstruction kinetics probed by HER on Au(111) electrodes. *Electrochimica Acta*, 347:136287, jul 2020.
- [30] Shengxiang Yang and Dennis G. H. Hetterscheid. Redefinition of the Active Species and the Mechanism of the Oxygen Evolution Reaction on Gold Oxide. *ACS Catalysis*, 10(21):12582–12589, nov 2020.
- [31] G. Palasantzas and J. Krim. Effect of the form of the height-height correlation function on diffuse x-ray scattering from a self-affine surface. *Physical Review B*, 48(5):2873–2877, aug 1993.
- [32] J. Krim and J. O. Indekeu. Roughness exponents: A paradox resolved. *Physical Review E*, 48(2):1576–1578, aug 1993.
- [33] A. Le Gal and M. Klüppel. Investigation and modelling of rubber stationary friction on rough surfaces. *Journal of Physics: Condensed Matter*, 20(1):015007, jan 2008.
- [34] Pai Li and Feng Ding. Origin of the herringbone reconstruction of Au(111) surface at the atomic scale. *Science Advances*, 8(40):1–8, oct 2022.
- [35] M. Giesen, G. Schulze Icking-Konert, and H. Ibach. Fast Decay of Adatom Islands and Mounds on Cu(111): A New Effective Channel for Interlayer Mass Transport. *Physical Review Letters*, 80(3):552–555, jan 1998.
- [36] M. Giesen, G. Schulze Icking-Konert, and H. Ibach. Interlayer Mass Transport and Quantum Confinement of Electronic States. *Physical Review Letters*, 82(15):3101–3104, apr 1999.
- [37] Margret Giesen and Harald Ibach. On the mechanism of rapid mound decay. *Surface Science*, 464(1):L697–L702, sep 2000.
- [38] David Nečas and Petr Klapetek. Gwyddion: an open-source software for SPM data analysis. *Open Physics*, 10(1):181–188, feb 2012.

## Bibliography

---

- [39] Wei Wang, Yi-Fan Huang, Dong-Yu Liu, Fang-Fang Wang, Zhong-Qun Tian, and Dongping Zhan. Electrochemically roughened gold microelectrode for surface-enhanced Raman spectroscopy. *Journal of Electroanalytical Chemistry*, 779:126–130, oct 2016.
- [40] Ulmas Zhumaev, Alexander V. Rudnev, Jian-Feng Li, Akiyoshi Kuzume, Thu-Hien Vu, and Thomas Wandlowski. Electro-oxidation of au(111) in contact with aqueous electrolytes: New insight from in situ vibration spectroscopy. *Electrochimica Acta*, 112:853–863, 2013.
- [41] Leon Jacobse, Yi-Fan Huang, Marc T. M. Koper, and Marcel J. Rost. Correlation of surface site formation to nanoisland growth in the electrochemical roughening of Pt(111). *Nature Materials*, 17(3):277–282, mar 2018.
- [42] Marcel J Rost, Leon Jacobse, and Marc T M Koper. The dualism between adatom- and vacancy-based single crystal growth models. *Nature Communications*, 10(1):5233, 2019.
- [43] J. V. Barth, H. Brune, G. Ertl, and R. J. Behm. Scanning tunneling microscopy observations on the reconstructed au(111) surface: Atomic structure, long-range superstructure, rotational domains, and surface defects. *Phys. Rev. B*, 42:9307–9318, Nov 1990.
- [44] U. Harten, A. M. Lahee, J. Peter Toennies, and Ch. Wöll. Observation of a soliton reconstruction of au(111) by high-resolution helium-atom diffraction. *Phys. Rev. Lett.*, 54:2619–2622, Jun 1985.
- [45] Carsten Koentje, Dieter Kolb, and Gregory Jerkiewicz. Roughening and long-range nanopatterning of au(111) through potential cycling in aqueous acidic media. *Langmuir : the ACS journal of surfaces and colloids*, 29, 07 2013.
- [46] M.A. Schneeweiss and D.M. Kolb. Oxide formation on au(111) an in situ stm study. *Solid State Ionics*, 94(1):171–179, 1997. Papers from the International Workshop.
- [47] Benchaporn Lertanantawong, Anthony P. O'Mullane, Werasak Surareungchai, Mithran Somasundrum, L. Declan Burke, and Alan M. Bond. Study of the underlying electrochemistry of polycrystalline gold electrodes in aqueous solution and electrocatalysis by large amplitude fourier transformed alternating current voltammetry. *Langmuir*, 24(6):2856–2868, 2008. PMID: 18266392.
- [48] B.E. Conway. Electrochemical oxide film formation at noble metals as a surface-chemical process. *Progress in Surface Science*, 49(4):331–452, 1995.
- [49] Oscar Diaz-Morales, Federico Calle-Vallejo, Casper de Munck, and Marc T. M. Koper. Electrochemical water splitting by gold: evidence for an oxide decomposition mechanism. *Chem. Sci.*, 4:2334–2343, 2013.

- [50] Saeid Behjati and Marc T. M. Koper. In situ stm study of roughening of au(111) single-crystal electrode in sulfuric acid solution during oxidation–reduction cycles. *The Journal of Physical Chemistry C*, 128(44):19024–19034, 2024.
- [51] M.A. Diaz, G.H. Kelsall, and N.J. Welham. Electrowinning coupled to gold leaching by electrogenerated chlorine. au(iii) au(i) au kinetics in aqueous cl<sub>2</sub>/cl-electrolytes. *Journal of Electroanalytical Chemistry*, 361(1):25–38, 1993. An International Journal Devoted to all Aspects of Electrode Kinetics, Interfacial Structure, Properties of Electrolytes, Colloid and Biological Electrochemistry.
- [52] Shen Ye, Chikara Ishibashi, Katsuaki Shimazu, and Kohei Uosaki. An in situ electrochemical quartz crystal microbalance study of the dissolution process of a gold electrode in perchloric acid solution containing chloride ion. *Journal of The Electrochemical Society*, 145(5):1614, may 1998.
- [53] Th. Heumann and H. S. Panesar. Beitrag zur frage nach dem auflösungsmechanismus von gold zu chlorkomplexen und nach seiner passivierung. *Zeitschrift für Physikalische Chemie*, 229O:84–97, 5 1965.
- [54] Shen Ye, Chikara Ishibashi, and Kohei Uosaki. Anisotropic dissolution of an au(111) electrode in perchloric acid solution containing chloride anion investigated by in situ stmthe important role of adsorbed chloride anion. *Langmuir*, 15(3):807–812, 1999.
- [55] Dennis J. Trevor, Christopher E. D. Chidsey, and Dominic N. Loiacono. In situ scanning-tunneling-microscope observation of roughening, annealing, and dissolution of gold (111) in an electrochemical cell. *Phys. Rev. Lett.*, 62:929–932, Feb 1989.
- [56] Margret Giesen and Dieter M. Kolb. Influence of anion adsorption on the step dynamics on Au (111) electrodes. *Surface Science*, 468(1-3):149–164, nov 2000.
- [57] Dennis J Trevor, Christopher ED Chidsey, and Dominic N Loiacono. In situ scanning-tunneling-microscope observation of roughening, annealing, and dissolution of gold (111) in an electrochemical cell. *Physical review letters*, 62(8):929, 1989.
- [58] Karina Morgenstern, Georg Rosenfeld, Bene Poelsema, and George Comsa. Brownian motion of vacancy islands on ag (111). *Physical review letters*, 74(11):2058, 1995.
- [59] M Eßer, K Morgenstern, G Rosenfeld, and G Comsa. Dynamics of vacancy island coalescence on ag (111). *Surface science*, 402:341–345, 1998.
- [60] Cristina Vaz-Dominguez, Asier Aranzabal, and Angel Cuesta. In situ stm observation of stable dislocation networks during the initial stages of the lifting of the reconstruction on au (111) electrodes. *The Journal of Physical Chemistry Letters*, 1(14):2059–2062, 2010.

## Bibliography

---

- [61] V Maurice, H-H Strehblow, and P Marcus. In situ stm study of the initial stages of oxidation of cu (111) in aqueous solution. *Surface Science*, 458(1-3):185–194, 2000.
- [62] Carissima M Vitus and Alison J Davenport. In situ scanning tunneling microscopy studies of the formation and reduction of a gold oxide monolayer on au (111). *Journal of The Electrochemical Society*, 141(5):1291, 1994.
- [63] Monika M Biener, Juergen Biener, and Cynthia M Friend. Revisiting the s- au (111) interaction: Static or dynamic? *Langmuir*, 21(5):1668–1671, 2005.
- [64] Monika M Biener, Juergen Biener, and Cynthia M Friend. Sulfur-induced mobilization of au surface atoms on au (1 1 1) studied by real-time stm. *Surface science*, 601(7):1659–1667, 2007.
- [65] BK Min, AR Alemozafar, MM Biener, J Biener, and CM Friend. Reaction of au (111) with sulfur and oxygen: Scanning tunneling microscopic study. *Topics in Catalysis*, 36:77–90, 2005.
- [66] Holly Walen, Da-Jiang Liu, Junepyo Oh, Hyunseob Lim, James W Evans, Yousoo Kim, and PA Thiel. Self-organization of s adatoms on au (111):  $\sqrt{3} \times 30$  rows at low coverage. *The Journal of chemical physics*, 143(1), 2015.
- [67] Peter M Spurgeon, Da-Jiang Liu, Theresa L Windus, James W Evans, and Patricia A Thiel. Enhanced nanostructure dynamics on au (111) with adsorbed sulfur due to au- s complex formation. *ChemPhysChem*, 22(4):349–358, 2021.
- [68] Patricia A Thiel, Mingmin Shen, Da-Jiang Liu, and James W Evans. Adsorbate-enhanced transport of metals on metal surfaces: Oxygen and sulfur on coinage metals. *Journal of Vacuum Science & Technology A*, 28(6):1285–1298, 2010.
- [69] W. L. Ling, N. C. Bartelt, K. Pohl, J. de la Figuera, R. Q. Hwang, and K. F. McCarty. Enhanced self-diffusion on cu(111) by trace amounts of s: Chemical-reaction-limited kinetics. *Phys. Rev. Lett.*, 93:166101, Oct 2004.
- [70] Nicci Fröhlich, Julia Fernández-Vidal, Francesc Valls Mascaró, Arthur J. Shih, Mingchuan Luo, and Marc T.M. Koper. Effect of trace impurities in perchloric acid on blank voltammetry of pt(111). *Electrochimica Acta*, 466:143035, 2023.
- [71] L. D. Burke and P. F. Nugent. The electrochemistry of gold: I. the redox behaviour of the metal in aqueous media. *Gold Bulletin*, 30:43–53, 1997.
- [72] Fritz Scholz. Electroanalytical methods: Guide to experiments and applications. *Electroanalytical Methods: Guide to Experiments and Applications*, pages 1–359, 2010.
- [73] L. M. Siperko, S. S. Hurban, J. M. Spalik, and A. D. Katnani. Complementary scanning tunneling microscopy and scanning electron microscopy studies of electroplated gold surfaces. *Journal of Vacuum Science and Technology A*, 10:2400–2403, 7 1992.

- [74] C. Bocking and I. R. Christie. Gold electroplating a brief overview. *Interdisciplinary Science Reviews*, 17:239–243, 1992.
- [75] Aimin Yu, Zhijian Liang, Jinhan Cho, and Frank Caruso. Nanostructured electrochemical sensor based on dense gold nanoparticle films. *Nano Letters*, 3:1203–1207, 9 2003.
- [76] Paramaconi Rodriguez and Marc T. M. Koper. Electrocatalysis on gold. *Phys. Chem. Chem. Phys.*, 16:13583–13594, 2014.
- [77] J. Zhang, K. Sasaki, E. Sutter, and R. R. Adzic. Stabilization of platinum oxygen-reduction electrocatalysts using gold clusters. *Science*, 315:220–222, 1 2007.
- [78] Marc T.M. Koper and Hendrik A. Heering. Comparison of electrocatalysis and bioelectrocatalysis of hydrogen and oxygen redox reactions. *Fuel Cell Science: Theory, Fundamentals, and Biocatalysis*, pages 71–110, 10 2010.
- [79] Sang Hoon Kim. Nanoporous gold for energy applications. *The Chemical Record*, 21:1199–1215, 5 2021.
- [80] Yi Chun Lu, Zhichuan Xu, Hubert A. Gasteiger, Shuo Chen, Kimberly Hamad-Schifferli, and Yang Shao-Horn. Platinum-gold nanoparticles: A highly active bifunctional electrocatalyst for rechargeable lithium-air batteries. *Journal of the American Chemical Society*, 132:12170–12171, 9 2010.
- [81] Shaojun Guo and Erkang Wang. Synthesis and electrochemical applications of gold nanoparticles. *Analytica Chimica Acta*, 598:181–192, 8 2007.
- [82] Corinna Stumm, Sebastian Grau, Florian D. Speck, Felix Hilpert, Valentín Briega-Martos, Karl Mayrhofer, Serhiy Cherevko, Olaf Brummel, and Jörg Libuda. Reduction of oxide layers on au(111): The interplay between reduction rate, dissolution, and restructuring. *Journal of Physical Chemistry C*, 125:22698–22704, 10 2021.
- [83] Akansha Goyal, Giulia Marcandalli, Vladislav A. Mints, and Marc T. M. Koper. Competition between co2 reduction and hydrogen evolution on a gold electrode under well-defined mass transport conditions. *Journal of the American Chemical Society*, 142(9):4154–4161, 2020. PMID: 32041410.
- [84] M. Baldauf and D. M. Kolb. Formic acid oxidation on ultrathin pd films on au(hkl) and pt(hkl) electrodes. *Journal of Physical Chemistry*, 100:11375–11381, 7 1996.
- [85] Tamás Pajkossy, Thomas Wandlowski, and Dieter M. Kolb. Impedance aspects of anion adsorption on gold single crystal electrodes. *Journal of Electroanalytical Chemistry*, 414:209–220, 1 1996.

## Bibliography

---

- [86] O. M. Magnussen, J. Wiechers, and R. J. Behm. In situ scanning tunneling microscopy observations of the potential-dependent (1 × 2) reconstruction on au(110) in acidic electrolytes. *Surface Science*, 289:139–151, 5 1993.
- [87] Serhiy Cherevko, Angel A. Topalov, Ioannis Katsounaros, and Karl J.J. Mayrhofer. Electrochemical dissolution of gold in acidic medium. *Electrochemistry Communications*, 28:44–46, 3 2013.
- [88] Corinna Stumm, Manon Bertram, Maximilian Kastenmeier, Florian D Speck, Zhaozong Sun, Jonathan Rodríguez-Fernández, Jeppe V Lauritsen, Karl J J Mayrhofer, Serhiy Cherevko, Olaf Brummel, Jörg Libuda, C Stumm, M Bertram, M Kastenmeier, O Brummel, J Libuda, F D Speck, K J J Mayrhofer, S Cherevko, Z Sun, J Rodríguez-Fernández, and J V Lauritsen. Structural dynamics of ultrathin cobalt oxide nanoislands under potential control. *Advanced Functional Materials*, 31:2009923, 3 2021.
- [89] Marie Anne Schneeweiss, Dieter M. Kolb, Dezhong Liu, and Daniel Mandler. Anodic oxidation of au(111). *Canadian Journal of Chemistry*, 75(11):1703–1709, 1997.
- [90] Stanley Bruckenstein and Michael Shay. An in situ weighing study of the mechanism for the formation of the adsorbed oxygen monolayer at a gold electrode. *Journal of Electroanalytical Chemistry and Interfacial Electrochemistry*, 188:131–136, 6 1985.
- [91] Shen Ye, Chikara Ishibashi, Katsuaki Shimazu, and Kohei Uosaki. An in situ electrochemical quartz crystal microbalance study of the dissolution process of a gold electrode in perchloric acid solution containing chloride ion. *Journal of The Electrochemical Society*, 145:1614–1623, 5 1998.
- [92] S. Manne, J. Massie, V. B. Elings, P. K. Hansma, and A. A. Gewirth. Electrochemistry on a gold surface observed with the atomic force microscope. *Journal of Vacuum Science and Technology B: Microelectronics and Nanometer Structures Processing, Measurement, and Phenomena*, 9:950–954, 3 1991.
- [93] Carissima M. Vitus and Alison J. Davenport. In situ scanning tunneling microscopy studies of the formation and reduction of a gold oxide monolayer on au(111). *Journal of The Electrochemical Society*, 141(5):1291, may 1994.
- [94] Xiaoping Gao and Michael J. Weaver. Nanoscale structural changes upon electro-oxidation of au(111) as probed by potentiodynamic scanning tunneling microscopy. *Journal of Electroanalytical Chemistry*, 367(1):259–264, 1994.
- [95] Dennis J. Trevor and Christopher E. D. Chidsey. Room temperature surface diffusion mechanisms observed by scanning tunneling microscopy. *Journal of Vacuum Science and Technology B: Microelectronics and Nanometer Structures Processing, Measurement, and Phenomena*, 9:964–968, 3 1991.

- [96] Shen Ye, Chikara Ishibashi, and Kohei Uosaki. Anisotropic dissolution of an au(111) electrode in perchloric acid solution containing chloride anion investigated by in situ stmthe important role of adsorbed chloride anion. *Langmuir*, 15:807–812, 2 1998.
- [97] Hidetoshi Honbo, Shizuwara Suga, and Kingo Itaya. Detailed in situ scanning tunneling microscopy of single crystal planes of gold(111) in aqueous solutions. *Analytical Chemistry*, 62:2424–2429, 11 1990.
- [98] M. Kleinert, A. Cuesta, L.A. Kibler, and D.M. Kolb. In-situ observation of an ordered sulfate adlayer on au(100) electrodes. *Surface Science*, 430(1):L521–L526, 1999.
- [99] Angel Cuesta, Markus Kleinert, and Dieter M. Kolb. The adsorption of sulfate and phosphate on au(111) and au(100) electrodes: an in situ stm study. *Phys. Chem. Chem. Phys.*, 2:5684–5690, 2000.
- [100] O. M. Magnussen, B. M. Ocko, R. R. Adzic, and J. X. Wang. X-ray diffraction studies of ordered chloride and bromide monolayers at the au(111)-solution interface. *Physical Review B*, 51:5510, 2 1995.
- [101] A. Cuesta and D.M. Kolb. The structure of bromide and chloride adlayers on au(100) electrodes: an in situ stm study. *Surface Science*, 465(3):310–316, 2000.
- [102] Ariba Adnan, Saeid Behjati, Núria Félez-Guerrero, Kasinath Ojha, and Marc T. M. Koper. Tracking the surface structure and the influence of cations and anions on the double-layer region of a au(111) electrode. *Phys. Chem. Chem. Phys.*, 26:21419–21428, 2024.
- [103] A. Hamelin and S. Röttgermann. Cyclic voltammograms of the au(100) face. *Electrochimica Acta*, 32:723–724, 4 1987.
- [104] S. Šrbac, R. R. Adžć, and A. Hamelin. Oxide formation on gold single crystal stepped surfaces. *Journal of Electroanalytical Chemistry and Interfacial Electrochemistry*, 249:291–310, 7 1988.
- [105] H. Angerstein-Kozlowska, B. E. Conway, A. Hamelin, and L. Stoicoviciu. Elementary steps of electrochemical oxidation of single-crystal planes of au—i. chemical basis of processes involving geometry of anions and the electrode surfaces. *Electrochimica Acta*, 31:1051–1061, 8 1986.
- [106] H. Angerstein-Kozlowska, B. E. Conway, A. Hamelin, and L. Stoicoviciu. Elementary steps of electrochemical oxidation of single-crystal planes of au part ii. a chemical and structural basis of oxidation of the (111) plane. *Journal of Electroanalytical Chemistry and Interfacial Electrochemistry*, 228:429–453, 8 1987.
- [107] H. Angerstein-Kozlowska, B. E. Conway, K. Tellefsen, and B. Barnett. Stochastically-gated surface processes involving anions in oxidation of au: time-resolution of processes down to 0.25% coverages and 50  $\mu$ s time-scales. *Electrochimica Acta*, 34:1045–1056, 8 1989.

## Bibliography

---

- [108] Holly Walen, Da-Jiang Liu, Junepyo Oh, Hyunseob Lim, J. W. Evans, Yousoo Kim, and P. A. Thiel. Self-organization of s adatoms on au(111):  $\sqrt{3}r30^\circ$  rows at low coverage. *The Journal of Chemical Physics*, 143(1):014704, 07 2015.
- [109] Saeid Behjati and Marc T. M. Koper. Effect of trace amounts of chloride on roughening of au(111) single-crystal electrode surface in sulfuric acid solution during oxidation-reduction cycles. *ACS Electrochemistry*, 1(7):1082–1092, 2025.
- [110] V. Maurice, H.-H. Strehblow, and P. Marcus. In situ stm study of the initial stages of oxidation of cu(111) in aqueous solution. *Surface Science*, 458(1):185–194, 2000.
- [111] M. Wilms, M. Kruft, G. Bermes, and K. Wandelt. A new and sophisticated electrochemical scanning tunneling microscope design for the investigation of potentiodynamic processes. *Review of Scientific Instruments*, 70(9):3641–3650, 09 1999.
- [112] Klaus Wandelt Knud Gentz. Electrochemical scanning tunneling microscopy. *CHIMIA*, 66(1/2):44, Feb. 2012.
- [113] Richard Sonnenfeld and Paul K. Hansma. Atomic-resolution microscopy in water. *Science*, 232(4747):211–213, 1986.
- [114] Dong-Yuan Sheng and Qiang Yue. Modeling of fluid flow and residence-time distribution in a five-strand tundish. *Metals*, 10(8), 2020.
- [115] Robert E. Treybal. *Mass-Transfer Operations*. McGraw-Hill Book Company, New York, 3rd edition, 1980.
- [116] Flow Science, Inc. *Flow-3D User Manual: v10.1*. Flow Science, Inc., Santa Fe, NM, 2012.
- [117] C.W Hirt and B.D Nichols. Volume of fluid (vof) method for the dynamics of free boundaries. *Journal of Computational Physics*, 39(1):201–225, 1981.
- [118] Francis H. Harlow and J. Eddie Welch. Numerical calculation of time-dependent viscous incompressible flow of fluid with free surface. *The Physics of Fluids*, 8(12):2182–2189, 12 1965.
- [119] Octave Levenspiel. *Chemical Reaction Engineering*. Wiley, New York, 3rd edition, 1998.
- [120] Tingyi "Leo" Liu and Chang-Jin "CJ" Kim. Contact angle measurement of small capillary length liquid in super-repelled state. *Scientific Reports*, 7(1):740, 2017.
- [121] P.V. Danckwerts. Continuous flow systems. distribution of residence times. *Chemical Engineering Science*, 2(1), 1958.

- [122] Shaofan Li and Gang Wang. Introduction of Dislocation Theory. In *Introduction to Micromechanics and Nanomechanics*, pages 341–411. WORLD SCIENTIFIC, feb 2018.
- [123] Serhiy Cherevko, Angel A. Topalov, Aleksandar R. Zeradjanin, Ioannis Katsounaros, and Karl J. J. Mayrhofer. Gold dissolution: towards understanding of noble metal corrosion. *RSC Advances*, 3(37):16516, 2013.
- [124] S. H. Cadle and Stanley Bruckenstein. Ring-disk electrode study of the anodic behavior of gold in 0.2m Sulfuric acid. *Analytical Chemistry*, 46(1):16–20, 1974.
- [125] S. Vesztergom, M. Ujvári, and G.G. Láng. RRDE experiments with potential scans at the ring and disk electrodes. *Electrochemistry Communications*, 13(4):378–381, apr 2011.
- [126] Buddha Ratna Shrestha, Atsushi Nishikata, and Tooru Tsuru. Application of channel flow double electrode to the study on gold dissolution during potential cycling in sulfuric acid solution. *Journal of Electroanalytical Chemistry*, 665:33–37, jan 2012.



# Summary

In this study, we investigated the electrochemical behavior and surface evolution of Au(111) electrode under different conditions and electrochemical techniques, using a homemade electrochemical scanning tunneling microscope (EC-STM), revealing the intricate interplay between surface roughening, atom mobility, and impurity effects. Initially, the working principle of the EC-STM is explained, and the mechanical and electrical specifications of the designed modules for this instrument are discussed. This technical information can be eye-catching for many individuals with an engineering background. However, having a good understanding of the design can make running the experiments easier for other researchers (i.e., electrochemists). Moreover, this knowledge can reveal the capability of the instruments for applying more complicated experiments. In the first investigation conducted in 0.1 M sulfuric acid, we elucidated Au(111) roughening, demonstrating that it initiates with 2D island formation followed by 3D growth. Delays in the double-layer potential region led to larger 2D islands at lower ORC numbers and reduced roughness amplitude for the entire cycle numbers, driven by high gold atom mobility. Though oxidation-reduction charges were inversely correlated with roughness, suggesting terrace sites contribute more to charge density than roughened areas. In the second study, we explored the impact of chloride ions in 0.1 M sulfuric acid containing traces of HCl concentrations (1–50  $\mu$ M) over 200 oxidation-reduction cycles (ORCs). High chloride levels (50  $\mu$ M) induced rapid Au dissolution and high atom mobility, suppressing vacancy island capturing in the STM images and surface roughening, with minimal CV changes, while lower concentrations (10  $\mu$ M) allowed slower dissolution and detectable vacancy islands, introducing new CV peaks caused by the new defect sites. At the lowest concentration (1  $\mu$ M), inhomogeneous chloride adsorption changed the atom mobility and roughening process over the ORCs. Finally, the third investigation in HClO<sub>4</sub> solutions highlighted anisotropic surface evolution by altering the electrochemical double-layer structure and reaction

## **Summary**

---

dynamics likely due to the trace amount of impurities in the solution. These impurity effects highlight the complexity of the prediction of the surface electrode response of Au(111) at different spots. The results of this work can offer some valuable insights for a better understanding of gold-based electrochemical systems and raise more fundamental questions for future research.

# Samenvatting

De oppervlakte-evolutie van de Au(111)-elektrode in verschillende elektrolyten en condities, onderzocht met een zelfgemaakte elektrochemische scanning tunneling microscoop (EC-STM)

In deze studie hebben we het elektrochemische gedrag en de oppervlakte-evolutie van de Au(111)-elektrode onderzocht onder verschillende omstandigheden en met verschillende elektrochemische technieken. Met behulp van een zelfgemaakte elektrochemische scanning tunneling microscoop (EC-STM) werd de ingewikkelde wisselwerking tussen oppervlakteruwheid, atoommobiliteit en onzuiverheidseffecten onthuld. Eerst wordt het werkingsprincipe van de EC-STM uitgelegd en worden de mechanische en elektrische specificaties van de ontworpen modules voor dit instrument besproken. Deze technische informatie kan specifiek interessant zijn voor personen met een technische achtergrond. Een goed begrip van het experimentele ontwerp kan het uitvoeren van deze experimenten echter ook vergemakkelijken voor andere onderzoekers (zoals elektrochemici). Bovendien kan deze kennis het vermogen van de instrumenten verduidelijken om ingewikkeldere experimenten toe te passen. In het eerste onderzoek dat werd uitgevoerd in 0.1 M zwavelzuur, hebben we het proces van verruwing van Au(111) opgehelderd en aangetoond dat het begint met 2D-eilandvorming, gevolgd door 3D-groei. Vertragen van het proces door de aangelegde potentiaal in het gebied van de elektrische dubbellaag te houden leidt tot grotere 2D-eilanden bij lagere hoeveelheden van oxidatie-reductie-cycli (ORC) en een lagere amplitude van de ruwheid voor alle geteste aantalen cycli, gedreven door de hoge mobiliteit van goudatomen. De lading van de oxidatie-reductie is echter invers gecorreleerd met de ruwheid, wat suggereert dat terrassen meer bijdragen aan ladingsdichtheid dan ruwe gebieden. In de tweede studie onderzochten we de impact van chloride-ionen in 0.1 M zwavelzuur met sporen

## **Samenvatting**

---

van HCl (1–50  $\mu$ M) gedurende 200 ORC's. Hoge chloridegehaltes (50  $\mu$ M) induceerde het snelle oplossen van Au en een hoge atoommobiliteit, waardoor het vastleggen van vacante eilanden in de STM-beelden en het verruwen van het oppervlak werden onderdrukt, met minimale verandering in het cyclische voltamogram (CV), terwijl lagere concentraties (10  $\mu$ M) langzamere oplossing en detecteerbare vacante eilanden mogelijk maakten, waardoor nieuwe CV-pieken werden waargenomen die werden veroorzaakt door de nieuwe defectlocaties. Bij de laagste concentratie (1  $\mu$ M) veranderde inhomogene chloride-adsorptie de atoommobiliteit en het verruwingssproces tijdens de ORC's. Tot slot benadrukt het derde onderzoek in  $\text{HClO}_4$ -oplossingen de anisotrope oppervlakte-evolutie door het beïnvloeden van de elektrochemische dubbellaagstructuur en de reactiedynamiek, waarschijnlijk vanwege de achtergrondconcentratie van onzuiverheden in de oplossing. Deze onzuiverheidseffecten benadrukken de complexiteit in het voorspellen van de respons van het oppervlak van de Au(111) elektrode op verschillende plekken. De resultaten van dit werk kunnen waardevolle inzichten bieden voor een beter begrip van op goud gebaseerde elektrochemische systemen en roepen meer fundamentele vragen voor toekomstig onderzoek.

# List of publications

1. Saeid Behjati and Marc T. M. Koper. In situ STM study of roughening of Au(111) single-crystal electrode in sulfuric acid solution during oxidation–reduction cycles. *The Journal of Physical Chemistry C*, 128(44):19024–19034, 2024.
2. Saeid Behjati and Marc T. M. Koper. Effect of trace amounts of chloride on roughening of Au(111) single-crystal electrode surface in sulfuric acid solution during oxidation–reduction cycles. *ACS Electrochemistry* 1 (7), 1082-1092, 2025.
3. Saeid Behjati, Mojtaba Hajilo, Maximilian Albers, and Marc T. M Koper. Anisotropic Roughening of a Au(111) Single-Crystal Electrode Surface in  $\text{HClO}_4$  Solution during Oxidation–Reduction Cycles. *J. Phys. Chem. C*, 129(19), 8915–8926, 2025.
4. Ariba Adnan, Saeid Behjati, Núria Félez-Guerrero, Kasinath Ojha, and Marc T. M. Koper. Tracking the surface structure and the influence of cations and anions on the double-layer region of a Au(111) electrode. *Phys. Chem. Chem. Phys.* 26(32):21419-21428, 2024.
5. Zahra Sharifi, Saeid Behjati, Jacques H.O.J. Wijenberg, Arnoud C.A. de Vooys, and Marc T.M. Koper. Mechanism of Cr(III)-based oxide-hydroxide film electrodeposition in an acidic solution. *Electrochimica Acta*, 512:145451, 2025.

# Curriculum vitae

Saeid Behjati was born in Iran (Tehran) in August 1991. He went through elementary and middle school while developing his early interests in electronics. During his high school years, he developed some interest in mechanics as well. Thus, he decided to continue his study for a bachelor program in solid state physics (2009–2014) at KNTU providing a quantitative grounding for his multidisciplinary interests. Later, as a master’s candidate in Photonics (2014–2016) at SBU, during his Master’s Project, he designed and fabricated a multichannel plasmonic absorber, combining advanced optical simulation with precision micro-fabrication. From June 2017 to September 2019, he served as an Instrument Developer, designing, manufacturing, and assembling a dynamic balance machine compliant with ISO 1940-1. He developed mechanical components (SolidWorks/CNC), electrical modules for vibration sensors, tachometers, encoders, and FPGA-based control systems programmed in VHDL. He also developed software for real-time motor control, data acquisition, signal processing, and automated report generation.

Subsequent to finalizing the previous project, he started looking for a more challenging and fun project to accomplish. An open position at Leiden University caught his eye, and the requirements of the projects fit very nicely with his background. Hitting COVID caused a long delay in the project’s start date, and he finally started the project in 2020 with all COVID-related limitations. Due to the final goal of the project and unpredictable challenges during the first year of his PhD, he decided to develop a new electrochemical scanning tunneling microscope (EC-STM) in the chemistry department of Leiden University, which satisfies all the technical needs toward the goals. After two years of hard work and perseverance, the first successful experiment was conducted and the instrument became available for serious experiments. The study of Au(111) roughening in different electrolytes led to many new findings for the rest of his time as a PhD candidate.

During his PhD, Saeid actively engaged in professional development courses and workshops such as Effective Communication, Planning and Managing Your PhD, and Scientific Conduct for PhDs. Alongside his research, he also found fulfillment in teaching, supervising two bachelor internship students and one master's thesis student in their respective projects.

He presented his research work at local and international conferences, including Reedijk Symposium 2023 at Leiden university, the International Society of Electrochemistry (ISE) Annual Meeting in 2023 and 2024, the Netherlands' Catalysis and Chemistry Conference (NCCC) in 2024 and 2025.

*Saeid*

*Leiden, May 2025*

# Acknowledgements

I am profoundly grateful to my promoter, Prof. dr. M.T.M. Koper, and my co-promoter, Dr. R.V. Mom, for their exceptional trust and guidance throughout my research. Although I already had a strong background in instrument development, being given the opportunity to design and successfully develop a new electrochemical scanning tunneling microscope for CASC in a short time frame was both exciting and deeply meaningful to me. I am pleased that their confidence in me proved to be well-placed.

I also extend my sincere thanks to my teammates in CASC and colleagues in FMD, and ELD, for their invaluable collaboration and support. Their assistance greatly enriched this journey and contributed to the success of my experiments.

Finally, I express my heartfelt gratitude to my family and friends, whose love, patience, and encouragement provided the strength to persevere through this endeavor.